Modeling and simulation of uni- and multi-flagellar bacterial locomotion in a viscous fluid

by

Vahid Nourian

A thesis
presented to the University of Waterloo
in fulfillment of the
thesis requirement for the degree of
Doctor of Philosophy
in
Applied Mathematics

Waterloo, Ontario, Canada, 2022

Examining Committee Membership

The following served on the Examining Committee for this thesis. The decision of the Examining Committee is by majority vote.

External Examiner:	Sookkyung Lim Professor, Department of Mathematical Sciences University of Cincinnati
Supervisor(s):	Henry Shum Assistant Professor, Department of Applied Mathematics Faculty of Mathematics, University of Waterloo
Internal Member:	Anita Layton Professor, Department of Applied Mathematics Faculty of Mathematics, University of Waterloo
Internal Member:	Brian Ingalls Professor, Department of Applied Mathematics Faculty of Mathematics, University of Waterloo
Internal-External Member:	Nima Maftoon Assistant Professor, Department of Systems Design Engineering Faculty of Engineering, University of Waterloo

Author's Declaration

I hereby declare that I am the sole author of this thesis. This is a true copy of the thesis, including any required final revisions, as accepted by my examiners.

I understand that my thesis may be made electronically available to the public.

Abstract

Flagellated bacteria categorized as microorganisms, play vital roles in human life such that their beneficial and detrimental effects on different aspects of the ecosystem are indisputable. Flagellated bacteria propel themselves in fluids by rotating one or more flexible filaments, known as flagella, driven by independent flagellar motors. Depending on the rotation direction of the motors and handedness of the helical filaments, the flagella either pull or push the cell body. Entrapment of swimming bacteria near surfaces, observed in some species, may lead to biological processes such as biofilm formation and wound infection. Previous experimental and numerical studies of bacterial locomotion have illustrated that several behaviors exhibited by the bacteria have roots in hydrodynamic interactions between the bacteria components and the surrounding fluid.

In this thesis, we numerically study flagellated bacterial locomotion in bounded and unbounded spaces. The physical properties of the model bacteria in this study are described based on experimental data available for various species of uni-, bi-, and multiflagellated bacteria. Specifically, we choose *Vibrio alginolyticus*, *Magnetococcus marinus* and *Escherichia coli* to focus on their motility to shed light on some of the unique behavior observed in each one. Depending on the species, the model bacteria have either a spherical or a spherocylindrical cell body and the flexible flagellar filaments are connected to the cell body membrane directly or via very flexible straight hooks. The flagella are independently driven by either constant or variable torque motors. Despite a similar flagellar structure, uni- and multiflagellated bacteria employ different mechanisms to swim on straight trajectories or reorient.

Here, we use the boundary element method (BEM) and the Kirchhoff rod model to develop a comprehensive elastohydrodynamic framework in order to model the motility of uni- and multiflagellated bacteria in a Newtonian viscous fluid. For this purpose, the boundary integral equations (BIE) are numerically evaluated over the cell body surface and along the flagella which are described by distributions of regularized Stokeslets and Rotlets. By assuming that the flagella are inextensible and unshearable, the linear theory of elasticity is used to estimate the internal moments along the flagella. Adding the hydrodynamics and elasticity equations to the total force/torque balance and kinematic equations leads to a system of linear equations which are solved to find the velocities and update the swimmer configuration accordingly.

Motivated by experimental observations of *Vibrio alginolyticus* locomotion in which it is shown that there is an interesting correlation between the near-surface entrapment of bacteria and the concentration of certain ions in the swimming medium, we numerically investigate its motility in different concentrations of NaCl. Our simulations demonstrate that

changing the concentration of NaCl in the swimming fluid affects the tendency of pusher-mode bacteria to remain near the surfaces by altering the averaged swimming speed and inducing the different degrees of deformations along the flagellum. In addition to the ion concentration, our results indicate the flagellum/hook stiffness, the flagellar motor torque, and the cell body aspect ratio may affect whether the uniflagellated model bacterium escapes from the surface or becomes trapped in circular orbits.

By simulating the locomotion of a bi-flagellated model bacterium with a spherical cell body, one puller, and one pusher flagellum, we show that the bacteria with such configuration mainly swim along double helical trajectories. Comparing the properties of the obtained trajectories with the *Magnetococcus marinus*'s trajectories measured experimentally, indicate that this species has likely puller-pusher configuration. Varying the stiffness, orientations, or positions of the flagella significantly changes the swimming characteristics. Notably, when either the applied torque to the pusher flagellum is higher than a critical value and/or its stiffness is lower than a critical stiffness, the pusher flagellum exhibits overwhirling motion, resulting in a more complicated swimming style and a lower swimming speed. For a moderate flagellum stiffness, the swimming speed is insensitive to the rest orientation of the flagella over a wide range of orientation angles because the flagella deform to maintain alignment with the swimming direction.

Numerical investigation of multiflagellated bacteria locomotion in unbounded fluid indicates that the arrangement of the flagella on the cell body provides no advantages in the average swimming speeds of bacteria. However, the trajectory of the bacteria could be either relatively straight or double helical trajectory depending on the degree of asymmetry that exists in the distribution of the flagella. Our results indicate that the multiflagellated bacteria in the "run" state may have several stable swimming modes in which the swimming properties such as speeds and trajectories could be different. The tumbling event, stopping of the flagellar motor, and interaction with other bacteria are likely some reasons which cause the bacteria to switch between the different modes. High viscous torque due to the presence of a no-slip boundary slightly changes the swimming properties of the multiflagellated bacteria such as bundling time, the translational and angular speeds. Remarkably, the flagella arrangement is one of the key factors determining how the swimming properties vary in response to the presence of a surface.

Acknowledgements

Foremostly, I would like to express my sincere gratitude to my supervisor Prof. Shum. This work could not happen without his invaluable help, support, and encouragement.

I would like to thank all my examining committee members: Prof. Lim, Prof. Layton, Prof. Ingalls, and Prof. Maftoon for their valuable time, continuous assistance, and insightful comments on this dissertation.

The Natural Sciences and Engineering Research Council of Canada (NSERC), the University of Waterloo, and the Department of Applied Mathematics are all acknowledged for the financial support of this project and my program. The Faculty of Mathematics and Compute Canada are also acknowledged for providing computational facilities.

At the end, I express my special thanks to my lovely parents and sister for their endless support and patience throughout my journey.

Dedication

To my parents, for their endless love, support, and encouragement,
and
To all brave men and women fighting for freedom in Iran.

Table of Contents

List of Figures

List of Tables

Chapter 1

Introduction

Microorganisms have prominent roles in ecosystems. They break down complex compounds into more basic and usable molecules, eliminate other organisms' waste products, adjust the level of nutrients in the environment, etc. They directly or indirectly impact human health and welfare. While pathogenic microorganisms are responsible for many diseases and death, some other microorganisms carry out some processes in agriculture, food industries, and energy systems which have immense value to human society [5, 36, 72, 101].

1.1 Motivations

Some evidence indicates that most bacteria behave differently in their natural habitat and nutrient-rich media in laboratories. In nature, some kinds of bacteria form sessile microcolonies, where an extensive glycocalyx protects the bacteria against the antibacterial agents. In contrast, they do not follow their routine methods in microcolonies formation as they are tested in laboratories. In particular, their colicin sensitivity, antibiotic susceptibility, mating ability, etc. change in the nutrient-rich media where the competitive natural environment and its challenges are removed. In this regard, doing numerical studies are more affordable than recreating the natural environment to understand bacterial behavior better. Definitely, these investigations improve our understanding of the effects of several physical and geometrical parameters on bacterial behavior and significantly decrease the number of experiments required to be carried out in the laboratory or nature to discover the microorganisms world [15, 26, 69].

Positive and negative impacts of bacteria on human life have spurred interest in developing practical techniques to culture, sort, and purify the bacteria for various purposes or

fight against them. A deep understanding of bacterial behavior including their locomotion in bounded and unbounded environments facilitates the development of these techniques. Below, some beneficial and harmful effects of bacteria on human life are reviewed. In addition, recent development in designing and fabricating microrobots inspired by bacteria, and using the bacteria for biomedical applications are discussed.

Biofilms, which are the result of bacteria colonization, cause major problems in many industries [111]. Some food industries including brewing, dairy processing, fresh produce, poultry, and red meat processing are faced with this problem, for example. In particular, biofilm formation on equipment and work surfaces could lead to some serious hygiene problems and product spoilage. The microorganisms in the biofilm, facilitate the equipment corrosion by increasing the rate of chemical and biological reactions as well [111]. The thick biofilms reduce the efficiency of heat exchangers by preventing convection from the surfaces. It is estimated that the cost related to the heat exchangers biofouling alone in the UK is £ 300-500 million per year [32]. Regularly cleaning and replacing the tanks, pipes, and heat exchangers are the only practical solutions against biofilms in many industries. Biofouling on hulls of ships increases the drag force and accelerates metal corrosion and causes considerable economic losses for the transportation industry every year. Other industry sectors including refinery, power generation, etc. are also affected by the destructive effects of biofilm growth.

Today, approximately 45 percent of all nosocomial infections arise from implant devices. Defense systems of living cells usually eliminate bacterial colonization and contamination, but the implant surfaces as an external object are vulnerable to bacterial colonization. The contaminated implants can cause chronic infection or tissue necrosis which are extremely resistant to antibiotics and persist until the contaminated implant is removed [100]. Simultaneously, the biofilms on the implant surfaces provide a desirable environment for other kinds of harmful microbes to grow and be released into the body. In this regard, the interaction between the swimming bacteria and the surfaces is the first step in the formation of biofilm. For this reason, examining their behavior in this step, especially the hydrodynamic attraction between the swimming cells and the surfaces, sheds light on the main reasons and aspects of biofilm development. Then, more effective solutions against biofilm formation and its destructive consequences are achievable.

Designs of many swimming micro- and nanoscale robots are inspired by the microorganisms' structure. The design of these tiny robots requires a swimming mechanism that operates at low Reynolds numbers, hence they should execute a non-reciprocal motion to be able to swim and overcome the viscous forces. Like the microorganisms, these microscale swimmers are powered by chemically driven motors, otherwise, external stimuli, such as ultrasonic or magnetic fields have been proposed as alternatives. These controllable

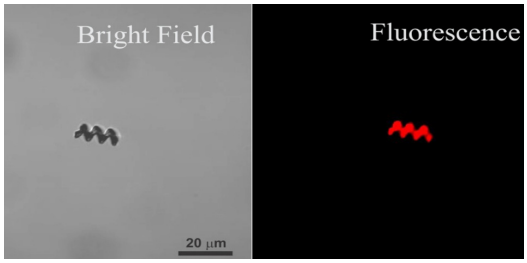

Figure 1.1: Artificial bacterial flagella under low-strength rotating magnetic fields can be used for drug delivery [91]. *Reprinted from Sensors and Actuators B: Chemical, Vol 196, Famin Qiu, Rami Mhanna, Li Zhang, Yun Ding, Satoshi Fujita, and Bradley J Nel- son, Artificial bacterial flagella functionalized with temperature-sensitive liposomes for controlled release, Pages 676-681, Copyright (2022), with permission from Elsevier (License Number:* 5396640965689*).*

machines enable us to get access to additional locations in the human body not possible before. Therefore new diagnoses and treatments become achievable by employing them. The microrobots have enormous potential for a variety of applications including directed drug delivery (Fig. 1.1), sensing of biological targets, detoxification, and also precision surgery [102, 64]. Interestingly, using live bacteria to implement some biomedical tasks had optimistic results. In this regard, Felfoul et al. used *M. marinus* bacteria to deliver a drug to tumor regions under magnetic field guidance. They showed that this method of drug delivery significantly improves the therapeutic index. These kinds of applications are not limited to magnetotactic bacteria (MTB); naturally non-magnetic microorganisms can also be directed by magnetic field after incorporation of magnetic particles ([84, 4]). In all the mentioned applications, the competition between the hydrodynamic forces and the external stimuli (magnetic field in the last example) has an important role in directing the microswimmers toward the target, so discovering the different aspects of these interactions facilitates the development of the swimmer microrobots.

Separating, sorting, and purifying some specific species of bacteria are inseparable parts of their applications in medicine, agriculture, industry, etc. Recently and for these purposes, several microfabricated devices have been designed and employed to separate some bacteria with specific features from the other microorganisms. As an illustration, the bacteria hydrodynamic entrapment near the surfaces offer interesting ways to manipulate them. It has been shown that motile *Escherichia coli* bacteria can be separated from non-motile cells by using a series of funnel walls between two or more reservoirs [41]. In another experimental study, a combination of ratcheting microchannels is used to sort *E. coli* by the cells' lengths [50]. Indeed, designing and fabricating such devices are not possible without a better understanding of the hydrodynamic interactions between the surfaces and the

bacteria.

Many pathogenic bacteria that cause disease in plants, animals, and humans are motile and use flagella to move. In these bacteria, motility is a key factor in the life cycle, especially in the initial phase of the infection. Some experimental studies have shown that *Helicobacter* species should have a complete motility organelle to initiate and develop an infection, for example. In this regard, some other observations have shown that *H. mustelae* and *H. pylori* mutants lacking flagella are completely unable to colonize [51].

All in all, studying the locomotion of the flagellated bacteria behavior not only sheds light on different aspects of their life (which can be used to control their harmful effects and maximize the benefits) but also provides inspiration to design artificial microrobots and microdevices.

1.2 Bacteria overview

According to the ribosomal RNA sequences, living cells phylogenetically can be classified into three major groups: Bacteria, Archaea and Eukarya. As shown in Fig. 1.2, Prokaryotes which include Bacteria and Archaea have a simpler structure than Eukaryotes which are fundamental units of animals, plants and fungi. In this figure, Prokaryotes are placed at the top and separated by a circular arc from the other microorganisms. The groups of microorganisms possessing flagella are within the central circle, and the flagellated Prokaryotes (including flagellated bacteria) are inside the overlap seen in the figure. Prokaryotes cell size varies from 0.1-0.2 µm to more than 50 µm in diameter and can be more than 0.5 mm in length [72]. Some specific species of flagellated bacteria as sub-group of Prokaryotes are the topic of interest in this thesis. Swimming flagellated bacteria have one or several flagella protruding from the cell membrane. Length, composition, and arrangement of flagella on the bacteria differ among species. In monotrichous (uniflagellated) bacteria, a flagellum is mainly attached to one end of the cell body, whereas in peritrichous (multi-flagellated) bacteria, the flagella can protrude from anywhere around the cell body. The rotation mechanism of each flagellum is almost the same among the monotrichous and peritrichous bacteria but their swimming mechanisms are completely different.

Monotrichous bacteria swim forward and backward by reversing the rotation direction of the flagellum from clockwise (CW) to counterclockwise (CCW) and vice versa. In this regard, the observations have illustrated that the monotrichous bacteria reorient by exhibiting different kinds of instabilities in the flagellar hook (universal joint which connects the flagellar motor to the flagellar filament) [115]. On the other hand, peritrichous bacteria

Figure 1.2: A general overview of microorganisms. *Reproduced from [65]. Copyright 1976 Society for Industrial and Applied Mathematics. Reprinted with permission. All rights reserved.*

mainly use bundling of flagella and tumbling to move in a specific direction or change their orientation, respectively [30].

As shown in Fig. 1.3, the flagellum structure consists of three different parts: a basal body, a hook, and a filament. The basal body is embedded in the inner membrane and forms the base of the flagellum. It includes four rings in gram-negative bacteria and two stacked rings in gram-positive bacteria which encompass a relatively rigid straight rod that connects the motor to the hook. The rotation of the flagellum is generated by a rotary motor that belongs in the basal body. In this regard, the motor power comes from the ion motive force in which the ion translocation (usually H^+ and/or Na^+) through a transmembrane stator induces the central rod rotation [78].

The hook that connects the central rod to the flagellar filament and transmits the torque, is composed of a special protein called hook protein [125]. A unique structure of this protein allows the hook to be more flexible than the filament. The level of hook flexibility is important because its deformations and instabilities play a prominent role in the locomotion of uni and multiflagellated bacteria. Particularly, the hook bending in peritrichous bacteria allows the flagella to bundle together and push the cell body forward [80]. On the other hand, the uniflagellated bacteria benefit from the specific structure of the hook to exhibit buckling instability and change the swimming direction. The hook's buckling leads to a misalignment between the cell body and the filament axes and results in a reorientation of the cell body [115]. In addition to the hook stiffness, its length can also affect the stability of bacterial locomotion. A longer/more flexible hook buckles more easily and causes buckling instability, whereas a shorter/stiffer hook is not flexible enough to act as a universal joint [78].

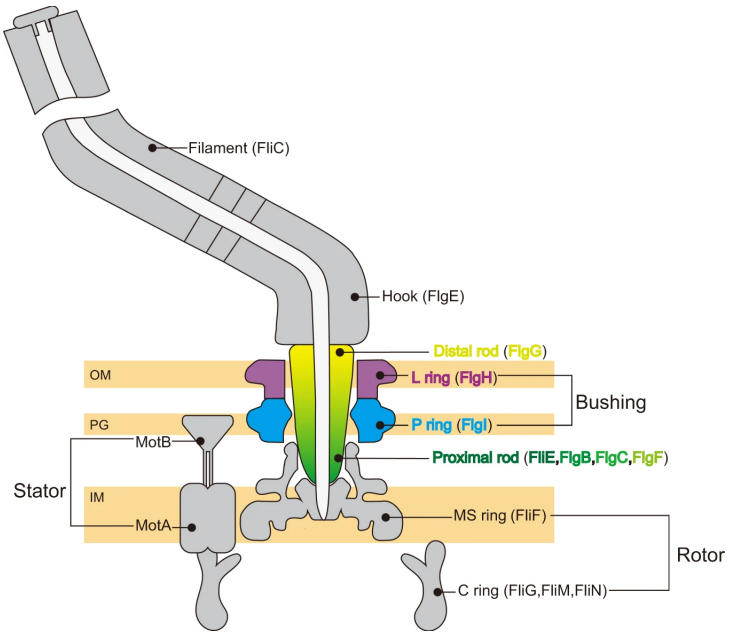

Figure 1.3: Structure of bacterial flagellum with a rotary motor embedded in the inner membrane. *Adapted from Yamaguchi et al. (2021), Structure of the molecular bushing of the bacterial flagellar motor [129].*

The flagellar filament is relatively flexible and forms the main part of the flagellum. Experimental measurements have demonstrated that the flagellar filaments are longer ($\approx$50 times) and stiffer ($\approx$100-1000 times) than the hook and are mostly helical in uni and

multiflagellated bacteria [78, 115]. For example, some measurements on *E. coli* and *S. typhimurium* have shown that the helical filament length and diameter are approximately 5-10 µm and 20 nm, respectively; and the properties are almost uniform along the filament [125]. Since the filament sub-units, called Flagellin, are not identical among the bacteria, the filament stiffness varies among the species [78].

Observations show that some motile bacteria tend to adhere to surfaces and establish microcolonies. The attachment to a surface becomes possible by using some protein fibrils called fimbriae, and/or nonfibrillar substances or secreting extracellular materials called Glycocalyx. Fimbriae protrude from the surface of most gram-negative bacteria and have adhesion which enables the bacteria to stick to the surfaces [125]. When the bacteria adhere to a surface, they start to grow and divide. During this process, the exuded polysaccharides and lipopolysaccharides (LPS) on the cell walls provide a permeability barrier especially for hydrophobic compounds (e.g. antibiotics, bile salts, hydrophobic dyes, etc.) [72]. By continuous division and joining to the microcolony, the bacteria develop a biofilm which is resistant to antibacterial chemicals and organisms.

1.3 Bacterial locomotion and flagellar arrangements

1.3.1 General experimental observations and modeling

Analysis of microscopic organisms' swimming in a viscous fluid began with Taylor [117, 118]. He noted that the stresses due to the viscosity on the microorganisms' bodies are many thousands of times greater than inertia. By ignoring the inertia effect, he described the different forces acting on microorganisms' bodies and employed Slender Body Theory (SBT) [16, 44] to calculate their magnitudes. Gray and Hancock [43] first implemented Resistive-Force Theory (RFT) to calculate the hydrodynamic forces along the tail of a spermatozoon of *Psammechinus miliaris*. RFT and SBT are closely related and use the slenderness of the flagellum to reduce the object to a one-dimensional structure [110]. Many studies [20, 55, 65, 46] have used these theories and published their analytical and numerical results for a microswimmer with a spherical cell body and helical or sinusoidal flagella in the unbounded viscous fluid. These theories are successful in the prediction of microswimmers' dynamics in unbounded fluids except where the hydrodynamic interactions between different parts of the microswimmer are considerable because the theories ignore such interactions.

Phan-Thien et al. [89] used the boundary-element method (BEM) to model the motion of a microswimmer with an ellipsoidal cell body and a rigidly rotating helical flagellum.

There was a good agreement between their results and Higdon's [46] who used SBT. In 2001, Fujita and Kawai [40] used BEM and performed an optimization on the parameters which represent the cell body and the flagellum shape. The numerically optimized architecture had a good agreement with the shape of typical bacteria except for the flagellum cross-section shape. These results imply that the shape of actual microorganisms is close to optimal in terms of power efficiency.

As already mentioned, each bacterial flagellum is driven by an independent rotary motor. Several experimental studies [17, 18] have been done to uncover the characterization of the flagellar motors. In this respect, the torque-speed curve of the *E. coli*'s flagellar motors indicates that depending on the motor's speed, the torque decreases gradually to a certain value and then drops to zero. For this reason, in many numerical simulations done to study the locomotion of this bacteria in low and medium speeds [80, 95, 96], the motor torque is assumed to be constant. In this thesis and depending on the bacteria species, we assume that the motor torque is constant or dynamically varies with the motor speed. However, some experimental studies [17, 73, 77] have shown that environment temperature and intracellular pH can change the motor's torque-speed curve. As a result, the constant torque or speed assumption is only valid in a short range of the environment temperature and the intracellular pH.

Experimental observations have shown that biofilm is formed when the bacteria sense that environmental conditions are suitable for life on surfaces. For instance, *E. coli K-12* and *Vibrio cholera* form biofilm in the environment where enough amino acids resources exist; whereas *P. aeruginosa* and *P. fluorescens* do under any conditions. The first step of biofilm formation consists of cell-cell and cell-surface interactions, and it is the most important and complex stage in the transition from a planktonic mode to a community-based mode [83]. Consequently, understanding the bacteria behavior in this step paves the way for finding effective protection against the biofilm. The motile bacteria's role in biofilm formation has directed recent scientific research toward studying bacterial locomotion either near surfaces or in confined spaces. Berke et al. [9] observed a strong increase of *E. coli* concentration at the boundaries when they deposited a uniform distribution of the cells between two glass plates. They theoretically demonstrated that the hydrodynamic interactions of cells and the boundary redirect the cells' orientation to the parallel with the surface where the cells are being attracted. Li et al. [62] observed a heavy accumulation of *Caulobacter crescentus* (mutant cells to swim exclusively forward (pusher mode)) near a surface when they deposited the cells on a glass slide. They reported that collisions between the cells and the surface cause the cells to be aligned parallel to the surface. They also found that the cells only spend a brief time close to the surface and do not follow a circular trajectory; hence the biofilm formation chance becomes low. Unlike the mutant cells,

they observed that the wild-type cells follow a circular path and be trapped by the surfaces when they move backward (puller mode). Lopez and Lauga [71] theoretically indicated that both slippery and non-slippery rigid surfaces reorient the bacteria parallel to the wall, but the direction of the circular orbits is different in these surfaces. Nevertheless, some experimental observations showed that both clockwise (CW) and counterclockwise (CCW) directions are seen near the slippery boundaries. Further investigations [61] indicated that some particles and surfactants in the swimming medium can change the boundary condition on slippery surfaces and reverse the rotation direction. These polymers can even alter the rotation direction close to non-slippery boundaries.

Observing the swimming patterns of *M. marinus*, *P. putida* and *V. fischeri* near a flat surface has had interesting results. Lin's observations [67] showed some circular trajectories for *P. putida*; these kinds of trajectories have been previously reported for peritrichous bacteria such as *E. coli* [59] and monotrichous bacteria like *Caulobacter crescentus* [63]. Several experiments have shown that all these species are hydrodynamically attracted to the surfaces, therefore a correlation between the exhibiting circular trajectories and being trapped to the surfaces is conceivable. Next, he found that *V. fischeri*'s swimming pattern is more random than *M. marinus* and *P. putida*. It swims at a constant speed in a straight line and then stops for a long period of time. He hypothesized that van der Waals and electrostatic forces may be the reason for such behavior. His observation on *M. marinus* indicated that this bacterium prefers to swim in straight trajectories with a high constant speed and fewer turns in the bulk, but it reduces the speed and turns away at the side boundaries.

Besides the experimental studies, some models have been introduced to investigate the microorganisms' behavior near surfaces or through confined environments. In 1995, Reynolds [98] developed Taylor's model to study an infinite waving sheet's behavior near a wall and between two parallel walls. His results indicate that the propulsive speed, first, rises slightly and then drops as the swimmer (the waving sheet) approaches the wall. Katz and Blake [53] found approximate resistance coefficients for slender bodies near a plane and between two parallel planes. These coefficients can be used in RFT to calculate the hydrodynamic forces on the microorganisms' flagella.

In 2009, Smith and Blake [114] tried to mathematically model the spermatozoa's tendency to swim near a surface. They used SBT and the boundary integral method to calculate the hydrodynamic forces on the cell body and the flagellum, respectively. As a study case, they showed the surface accumulation behavior of sperm cells. They also demonstrated that the sperm cell's size and shape are key factors in their tendency to swim near surfaces. Ramia et al. [93] used BEM to model the motion of slender and sphere bodies near a planar boundary. They compared their results with exact analytical solutions

and also SBT results and found an excellent agreement. They then applied their model to simulate the swimming of a microorganism with a spherical cell body and a rotating rigid flagellum. They investigated its swimming behavior near a planar boundary and between two parallel surfaces. Their results indicate less than 10% increase in the swimmer's mean speed which arises from the flagellar propulsive advantage near a solid boundary. Like many other studies, they also showed that the model bacterium moves on a circular path when it swims near a planar surface. In this regard, Frymier et al. [39] suggested that hydrodynamic interactions alone can not explain the bacteria's tendency to remain near the surfaces. They calculated the interaction potential energy, consisting of electrostatic repulsive and van der Waals attractive potentials, between the solid planar surface and the bacterium, then showed that this potential is minimum when the bacterium swims adjacent to the surface. As a result, it is concluded that the interaction potential might also play a role in trapping the cells close to the surfaces. A few years later, experimental observations by Vigeant et al. [123] refuted this argument. They observed two distinct behaviors of *E. coli* close to a planar surface: some motile bacteria which swim on a circular path and some non-motile bacteria. By this observation, they found that the motile bacteria are too distant from the surface to be affected by electrostatic interactions; therefore, the hydrodynamic interaction draws the cells to swim along the surface. In fact, the electrostatic interactions are only responsible for the adhesion of non-motile bacteria.

In the current thesis, we will study the locomotion of uni-, bi- and multiflagellated bacteria separately. In studying the behavior of uniflagellated bacteria we will mainly focus on *Vibrio alginolyticus*. For the biflagellated and multiflagellated bacteria, we will mainly explore the locomotion of *Magnetococcus marinus* and *Escherichia coli*. For this reason, we review the experimental and theoretical findings specific to these different groups of bacteria.

1.3.2 Uniflagellated bacteria

Monotrichous bacteria, such as *Vibrio alginolyticus*, have a single flexible flagellum that mainly extends from one pole of the cell body. The flagellum is approximately helical and is connected to the cell body via a very flexible and short hook. Previous experimental observations of monotrichous bacteria locomotion show that the bacteria move forward and backward by rotating the flagellum in two opposite directions, and changing the swimming orientation by buckling the hook [115, 126].

V. alginolyticus is one of many gram-negative bacteria. It can live and grow in the highly salted (with concentrations of 10%) marine environment. V. alginolyticus is known

as one of the pathogenic bacteria in humans since it may cause eye, ear, and wound infections [97]. Clinical data show that many patients suffering from this kind of infection have already been in contact with the seawater at the beaches. This species also lives in the bodies of animals such as pufferfish, where it produces the potent neurotoxin [70].

Whereas the flexibility of the hook and flagellum plays a subtle role in the movement of monotrichous bacteria, there are several studies that model their locomotion by assuming that the hook and flagellum are rigid. Shum et al. demonstrated that the hydrodynamic interactions of uniflagellated bacteria and a surface may cause the bacteria to become trapped in circular paths. Furthermore, their results indicated that the bacteria's tendency to swim close to the surfaces and their stable distances strongly depend on the cell body shape and the flagellum length [110]. They also showed that the uniflagellated bacteria are still attracted to a surface and exhibit stable periodic orbits when they swim between two parallel surfaces or at the corner of a rectangular channel [109, 108]. Even though these results are consistent with the experimental observations in some aspects, their model is unable to disclose the effects of the swimming speed, and hook/flagellum stiffness on the bacterial behavior.

To study the effects of hook bending on monotrichous bacteria motility, Shum and Gaffney assumed that a spherical rigid cell body is connected to a rigid flagellum via a naturally straight and flexible hook. Unlike the most common models in which an amplitude envelope factor is described to connect the flagellum to the cell body, in this study the hook joins tangentially to the helical flagellar filament. They found that effective swimming is possible if the hook stiffness and its length belong in specific intervals at a given motor torque. In addition, they indicated that steady swimming of the bacteria near a surface is very sensitive to hook rigidity, cell body, and flagellum shapes [107]. Park et al. revealed more details about the dynamics of the monotrichous bacterial flagellum by studying the instabilities of a flagellum with and without a hook. They demonstrated that a flexible rotating rod can get into three dynamical states: stable twirling, unstable whirling, and stable overwhirling, depending on physical properties like rotation frequency and filament stiffness. In addition, and in order to model the flagellum flick observed in *V. alginolyticus*, they assumed that motor reversal causes the hook to get into the relaxed mode in which the hook acquires smaller stiffness and becomes susceptible to buckling. In this regard, they calculated the buckling angle for different relaxed bending moduli by assuming that the hook remains in the relaxed mode for 0.03 seconds. It should be emphasized that even though the hook elastic properties change by the hook's load in their model, it is assumed that the bending moduli are constantly minimal during the flick state, independent of the hook's load, curvature, and twistness [86]. By adding a spheroidal cell body to the flagellum, they completed their model and reported the hook stiffness and

the rotation frequency critical thresholds for buckling instability. By assuming that the hook is in a relaxed mode for a short period of time, they investigated the effects of the hook stiffness and the rotation frequency on the buckling angles [88]. In another study, Park et al. numerically simulated the locomotion of a uniflagellated bacterium with a rigid cell body and a flexible flagellum close to a planar surface. They studied the influences of geometrical parameters, rotation frequency, and flagellum stiffness on the swimming features of the model bacterium [87].

Experimental observations of the locomotion of *V. alginolyticus* in a chemically homogeneous medium and near a source of attractant have underpinned that it executes a three-step strategy (forward, reverse and flick) to migrate. Moreover, the flagellar flicking is only seen in the transition from backward (puller mode) to forward (pusher mode) swimming. There is no flagellar instability in the transition from forward to backward swimming, and for this reason, this transition is three times faster than backward-flick-forward one [127]. Son et al. quantified the flagellar flicking process by imaging the locomotion of *V. alginolyticus*. They demonstrated that reorientation of the cell body occurs 10 ms after the onset of forward swimming. In addition, they measured the hook's bending stiffness in both relaxed and loaded states by applying thermal fluctuations. In this regard, their measurements indicate that the loaded hook is approximately 6 times stiffer than the relaxed hook and this difference likely initiates the flagellar flicking. In particular, the hook unwinds on motor reversal and becomes susceptible to buckling. After the flagellar flicking, the hook is loaded and stable forward swimming is achieved [115].

In modeling of *V. alginolyticus* it is mainly assumed that the motor applies either constant torque or speed to the flagellum. However, Sowa et al. [116] demonstrated that the torque generated by the *V. alginolyticus*'s motor increases with NaCl concentration in the swimming medium. Moreover, the rotation rate of the motor is inversely proportional to the motor load. Motivated by the conclusions of Sowa et al., we use three different torque-speed relationships for three levels of NaCl concentrations (50, 10 and 3 mM) to actuate the flagellar motor in simulating the locomotion of *V. alginolyticus*. In another study, the entrapment of three different strains of *V. alginolyticus* near surfaces is experimentally studied by Wu et al. [126]. They found that the cells can be entrapped near a surface in both puller and pusher modes. However, the entrapment behavior strongly depends on the cells' swimming speeds controlled by sodium concentration in the aqueous medium. Investigating the behavior of *V. alginolyticus* near a surface, in either puller or pusher modes and in different levels of NaCl concentrations is another aim of the present study.

1.3.3 Biflagellated bacteria

As already stated, the interest in using bacteria or fabricating bacterium-mimicking microrobots has grown in recent years [64, 36]. In this regard, magnetotactic bacteria (MTB) are of particular interest since they can be steered by applying external magnetic fields. Among the magnetotactic bacteria, *Magnetococcus marinus* (MC-1) is commonly studied and its biomedical applications for drug delivery have already been examined [36]. One of the striking differences between the *M. marinus* and widely studied bacteria, such as *E. coli*, is that *M. marinus* has two sheathed bundles of flagella on one side of the cell body. Each bundle is composed of seven flagellar filaments and many fibrils enveloped in a sheath. This structure of two bundles allows the bacteria to swim at speeds of up to $500\,\mu\mathrm{m\,s^{-1}}$ [6]. Magnetosomes, intracellular structures containing iron sulfide or iron oxide nanoparticles, allow *M. marinus* to navigate by the Earth's magnetic field [74].

Whereas the locomotion of uniflagellated bacteria has been well studied and, in many cases, a uniflagellated model adequately reproduces behavior in experiments even with multi-flagellated bacteria [108, 88, 87, 119], more specialized models are required to understand bundling, wrapping, and other complex phenomena with multiple flagella [37, 23, 80]. The unusual morphology and swimming style of *M. marinus* warrants further study. In earlier theoretical studies of *M. marinus*, it is assumed that the two flagellar bundles are behind the cell body and their synchronous rotations push the cell forward. Based on this assumption, the model bacterium swims in a relatively straight trajectory in the absence of a magnetic field [106]; it exhibits helical motion when a magnetic field is applied [130]. These results are inconsistent with some experimental observations [6], indicating that *M. marinus* travels along a double helical trajectory in the absence of magnetic field effects. Numerical simulations based on the Stokesian dynamics simulation method showed that such a double helical trajectory can be produced if one of the flagellar bundles pushes the cell while the other pulls.

Yang et al. [130] numerically and experimentally studied the effects of an external magnetic field on the locomotion of *M. marinus*. In their model, two rigid helical flagella push forward a prolate spheroidal cell body containing a magnetosome chain in a specific alignment. They employed resistive force theory (RFT) to model the hydrodynamic interactions and showed that there is a good agreement between the numerical and experimental results as they apply a wide range of magnetic fields for different inclinations of magnetic moment.

Shum [106] used a boundary element method (BEM) to simulate the motion of a model bacterium with two rigid pusher flagella near a surface. He found that placing the two flagella far apart reduces the cell body rotation rate. This could help the bacterium to move faster and achieve a better alignment with an external magnetic field. In addition, he

showed that the position and orientation of the flagella are two main factors that determine the bacterium's behavior in remaining trapped at a solid surface or escaping back to the bulk fluid.

Mohammadinejad et al. [74] developed a model based on Stokesian dynamics and Kirchhoff's rod model to investigate the locomotion of an MTB with a flexible pusher flagellum and spherical cell body in the presence of an external magnetic field. They focused on the response of MTB to the reversal of the external magnetic field and found that the diameter of the U-turn and the turning time are smaller for stronger magnetic fields. Moreover, they noted that the model bacterium undergoes a double helical motion when, simultaneously, the magnetic field is strong and the angle between the flagellum axis and the magnetic moment is large enough.

1.3.4 Multiflagellated bacteria

Peritrichous and monotrichous motile bacteria have different swimming mechanisms. In *E. coli* as a peritrichous bacteria, the hydrodynamic interactions between the flagella can lead to flagellar bundling, when all motors rotate CCW. It is discovered that the hydrodynamic interactions between the helical flagella are sufficient to induce the attraction and synchronize the flagella if they have sufficient flexibility [56, 94]. A switch in the rotation direction of any of the motors causes the bundled configuration to unravel and the cell begins to change orientation unpredictably, known as tumbling. Measurements have demonstrated that the duration of the "run" state (i.e. forward swimming) in *E. coli* swimming in bulk fluid is approximately 1s, whereas tumbling takes only 0.1s to be completed [75, 35]. In this regard, several experimental observations have reported that the averaged angle of change in the swimming direction of *E. coli* after a tumbling event is about 57° [121, 120].

In 2005, Flores et al. [37] employed regularized Stokeslets and Rotlets to model the hydrodynamic interactions among the three flagella and used a network of elastic springs to describe the flagella deformation. Since the modeling of the flagella is done by discrete points, they define a repulsive force to prevent the flagella from crossing each other. Reigh et al. [95] used a combination of molecular dynamic simulation (MD) and multiparticle collision dynamics (MPC) to simulate the bundling process of the flagella. They reported that increasing the number of flagella at a fixed radius decreases the bundling time. Huang and Jawed [49] numerically investigated the bundling behavior of two flexible filaments rotating close to each other. They concluded that the propulsive force decreases as the filaments are brought closer during the bundle formation. Kanehl et al. [52] numerically

investigated the swimming of multiflagellated bacteria by using BEM. They assumed that the cell body is a rigid ellipsoid and the flagellar filaments are rigid helices suspended on flexible hooks. They showed that flagellar bundling is possible with rigid filaments. They noted that the propulsive efficiency, defined as a function of swimming speed, increases by the number of flagella. In contrast, the energetic efficiency decreases. They also indicated that the cell body counter rotation and the number of flagella facilitate the bundling of flagella by decreasing the processing time.

Nguyen and Graham [80] numerically investigated the uni- and multiflagellated bacterial locomotion in an unbounded viscous fluid. They used SBT to compute the hydrodynamic forces on the swimmer and applied Kirchhoff's classical theory to model the flagella deformations. They investigated the possibility of stable swimming and bundle formation in different stiffness of the hook and the filaments. Finally, they found that the range of stiffness for stable swimming strongly depends on the number of flagella. In other words, they showed that a specific hook and filament's stiffness which leads to stable swimming in a biflagellar swimmer might cause an unstable motion in a quadriflagellar swimmer.

Following some experimental observations [54, 47], Liu et al. [68] studied the impacts of an upcoming fluid flow on run and tumble behavior of wild-type *E. coli*. They numerically and experimentally showed that the imposed fluid flow affects the bacteria behavior by decreasing the tumbling time and increasing the run time. In another study, Qu et al. [92] numerically and experimentally studied the effects of the fluid viscosity on the behavior of *E. coli*. They noted that bundling time and skewness of the speed distribution increase with the viscosity whereas the average swimming speed decreases.

Molaei et al. [75] experimentally showed that within 20 µm of a surface, the tumbling behavior of *E. coli* is suppressed by 50%. Their results also illustrate that the mean run time near the surfaces is approximately two times longer than the bulk fluid and its swimming speed during the run is 9% higher. The high viscous forces due to a no-slip boundary are responsible for these differences. In other experimental observations, it is demonstrated that *E. coli* swims in a circular trajectory when it is close to a planar boundary [8]. In this respect, by employing RFT and simulating the locomotion of *E. coli*, it is confirmed that the cells exhibit circular trajectories near solid surfaces [58]. Watari et al. [124] used the bead-spring model to reproduce the experimentally observed behavior of *E. coli* including the flagella bundling, tumbling, and polymorphic transformation. They showed that a flagellum polymorphic transformation enhances the cell body reorientation during the tumbling.

Clopes et al. [21] studied the impacts of flagellar arrangement on the swimming speed and the bundle formation in peritrichous bacteria. They compared three helical, ring, and

random anchoring patterns and found that regular patterns (helical, ring) do not provide any advantages in terms of the swimming speed in comparison with the random pattern, but they lead to single-bundle configuration.

1.4 Outline of the thesis

This thesis is comprised of six chapters. In chapter 1, we introduce the morphology of the flagellated bacteria as a subgroup of the microorganisms. Then, we describe the motivations and the reasons behind the investigation of bacterial locomotion. since we separately focus on the behavior of the uni, bi-, and multiflagellated bacteria, the literature review has three sub-sections for each group of bacteria.

In chapter 2, we describe our model and present the governing equations including hydrodynamic, elasticity, kinematics, force and torque balance equations, etc. In this chapter, we explain how we discretize the cell body surface and the flagella into some curved triangular elements and straight segments. In the rest of the chapter, we employ several numerical techniques to evaluate the relevant equations and speed up the calculations. At the end, we verify our model by comparing the obtained results with other analytical and numerical studies.

Chapter 3 is dedicated to investigating the locomotion of uniflagellated bacteria in unbounded fluid and near a planar surface. We mainly focus on the locomotion of *V. alginolyticus* and quantitatively shed light on the differences between the pusher and puller modes. We then investigate the effects of different physical parameters including hook/flagellum rigidity, cell body aspect ratio, initial condition, ions concentration, etc. on the tendency of the bacteria to swim close to the planar surfaces. At the end, the obtained results are compared with the experimental measurements.

Motivated by the experimental observation of MC-1, we dedicate chapter 4 to studying the locomotion of a biflagellated model bacterium with a spherical cell body and puller-pusher flagella. We examine how the bacteria migrate with puller-pusher flagella and why the bacteria move along a double-helical trajectory. Next, we investigate the effect of the flagella rigidity, the position and/or orientation of the flagella, and the motor torque ratio on the properties of the helical trajectory. We also show how overwhirling of the pusher flagellum changes the swimming characteristics. In the rest of chapter 4, we demonstrate how an external magnetic field is employed to direct the magnetotactic bacteria in a desirable direction. At the end, we compare the obtained results with the experimental measurements to shed light on the morphology of MC-1.

In chapter 5, we look into the behavior of multiflagellated bacteria by focusing on the swimming properties and the flagellar bundling. We specifically examine how the flagella arrangement and hook/flagella rigidity change the peritrichous bacteria's trajectory, swimming speed, and bundling time of the flagella. We show that the tumbling event may cause the bacteria to switch between the first and second stable swimming modes. In the rest of the chapter, the impacts of a planar surface on the swimming properties are explored. At the end, the variation of the translational and rotational speeds of the model bacteria with respect to the width of a rectangular confined channel is investigated.

Chapter 6 summarizes the methodology and results of the thesis, and also provides suggestions for future works.

Chapter 2

Governing Equations and Numerical Methods

2.1 Introduction

In the last four decades, the boundary element method (BEM) has been a powerful numerical technique to address a variety of complicated problems in science and engineering. The ability of the method in solving problems with complex geometry in an efficient way is one of the advantages of this method which has made it more popular over the traditional methods [90] such as Resistive Force Theory (RFT), Slender Body Theory (SBT), etc. The complexity of the bacteria geometry encourages us to employ this method to model the hydrodynamic interactions in the swimming of bacteria. Implementation of BEM in our framework has four steps: deriving the boundary integral equations, discretizing the swimmer surfaces into triangular elements and straight segments, approximating the integrals over the elements, and solving the boundary integral equations. In this respect, the weak singularity that exists in the fundamental Stokes solution forces us to employ the regularized Stokeslet approach in evaluating the integral along the flagella [24]. The image system for the Green's function, which is introduced by Blake [13] and developed by Cortez et al. [25, 3], is used here to model the hydrodynamic interactions near a planar surface. In our framework, we combine these methods with the standard Kirchhoff rod model to track the deformations of the rotating flagella in the viscous fluid. At the end, we construct a system of linear equations by including the kinematic and force/torque balance equations and solve it for the velocity vectors to update the bacterium configuration accordingly. In this chapter, we derive these equations and explain the numerical techniques utilized in

our framework.

2.2 Hydrodynamic equations

Brownian motion might pose a challenge in the modeling of bacterial locomotion, but findings of Dusenbery and Slovak et al. [34, 113] show that the effects of the Brownian motion are negligible for microorganisms with lengths of at least 1.73 µm. In this thesis, all the studied bacteria meet this condition so those effects will be neglected in the proposed model.

In modeling of the bacterial locomotion, the Reynolds number is very small ($\approx 10^{-5} - 10^{-4}$). Consequently, the inertia term in the Navier-Stokes equation is neglected and the hydro-dynamic interactions are governed by the incompressible Stokes equations:

$$-\nabla p + \mu \Delta \vec{u} + \vec{F_b} = \vec{0}, \tag{2.1}$$

$$\nabla \cdot \vec{u} = 0, \tag{2.2}$$

where μ is the fluid viscosity, p is the fluid pressure, $\vec{u}$ is the fluid velocity, and $\vec{F_b}$ is the force per unit volume applied to the fluid by the immersed body. In our model, the bacterium exerts a distribution of viscous stress $\vec{f}_{\mathrm{B}}$ over the surface B of the cell body (3D spherical or spherocylindrical cell body) and distributions of the viscous stress $\vec{f}_{\mathrm{F}}$ and viscous torque $\vec{n}_{\mathrm{F}}$ along the centerlines of the flagella $\Gamma^{(i)}$.

In a Lagrangian description, the elastic filaments $\Gamma^{(i)}$, which rotate and deform in time, and the cell body B are represented by a three-dimensional space curve $\vec{\gamma}(s,t)$ and surface $\vec{\Psi}(\theta,\phi,t)$, respectively. The variables s, θ, and ϕ are respectively material coordinates along the filament (initialized as arclength) and the cell body surface, and t is time. To ease the presentation, we let the variables $\vec{f}_{\mathrm{F}}(s,t)$, $\vec{n}_{\mathrm{F}}(s,t)$, and $\vec{\gamma}(s,t)$ denote the respective quantities for all flagella with the understanding that the integral over $\Gamma^{(i)} (i = 1, 2, \cdots, N_{\mathrm{F}})$ involves the variables associated with the respective flagellum. Using these definitions, the body force $\vec{F_b}$ is written as:

$$\begin{aligned}\vec{F_b}(\vec{x},t) = &\oint_B \vec{f}_{\mathrm{B}}(\theta,\phi,t)\delta(\vec{x} - \vec{\Psi}(\theta,\phi,t))dA(\theta,\phi) + \sum_{i=1}^{N_{\mathrm{F}}} \int_{\Gamma^{(i)}} \vec{f}_{\mathrm{F}}(s,t)\delta(\vec{x} - \vec{\gamma}(s,t))ds \\ &+ \sum_{i=1}^{N_{\mathrm{F}}} \frac{1}{2}\nabla \times \int_{\Gamma^{(i)}} \vec{n}_{\mathrm{F}}(s,t)\delta(\vec{x} - \vec{\gamma}(s,t))ds,\end{aligned} \tag{2.3}$$

where N_{F} denotes the number of flagella in the model bacteria. The evaluation point $\vec{x}$ can be anywhere in $\mathbb{R}^3$ including the model bacterium surface. To represent the flagella thickness and avoid the singularity to enhance the stability of the solution, we use regularized stokeslet formulation for the flagella. For this reason, we replace the delta function (δ) with cut-off functions ψ_ϵ and Φ_ϵ in the integrals. The radially symmetric cut-off functions approximate the delta function in three dimensions, and have the following property:

$$\int_{\mathbb{R}^3} \psi_\epsilon(\vec{x}) d\vec{x} = \int_{\mathbb{R}^3} \Phi_\epsilon(\vec{x}) d\vec{x} = 1. \tag{2.4}$$

Following Park et al. scheme [87], we choose cut off function Φ_ϵ to regularize the rotlet and ψ_ϵ to regularize the other kernels. These functions are defined as:

$$\psi_\epsilon(\vec{x}) = \frac{15\epsilon^4}{8\pi(\|\vec{x}\|^2 + \epsilon^2)^{7/2}}, \tag{2.5}$$

$$\Phi_\epsilon(\vec{x}) = \frac{3\epsilon^2}{4\pi(\|\vec{x}\|^2 + \epsilon^2)^{5/2}}, \tag{2.6}$$

where we assume that $\epsilon_F = \frac{d}{2}$ to represent the effective flagellum radius. The idea behind employing two different cut-off functions is related to applying the image system. In fact, the different decay rates of the two functions are necessary for finding combinations to exactly cancel out on the wall and satisfy the boundary conditions in the image system. terms [25, 3].

The solution for the Stokes equation with the body force Eq. 2.3 can be written as the boundary integral equation (see ref. [87, 24] for more details):

$$\vec{u}(\vec{x}, t) = \oint_B \vec{U}_s(\vec{f}_B, \vec{r}_B, \epsilon_B) dA(\theta, \phi) + \sum_{i=1}^{N_{\mathrm{F}}} \int_{\Gamma^{(i)}} \left[\vec{U}_s(\vec{f}_F, \vec{r}_F, \epsilon_F) + \vec{U}_r(\vec{n}, \vec{r}_F, \epsilon_F)\right] ds, \tag{2.7}$$

where $\vec{r}_B = \vec{x} - \vec{\Psi}(\theta, \phi)$, $\vec{r}_F = \vec{x} - \vec{\gamma}(s)$ are respectively the vectors from points on the cell body and flagella to the evaluation point $\vec{x}$. In this equation, $\vec{U}_s(\vec{f}, \vec{r}, \epsilon)$ and $\vec{U}_r(\vec{n}, \vec{r}, \epsilon)$ are respectively the velocities at the relative position $\vec{r}$ from a regularized stokeslet of strength $\vec{f}$ and a regularized rotlet of strength $\vec{n}$, with regularization parameter ϵ, given by the formulas [82]:

$$\vec{U}_s(\vec{f}, \vec{r}, \epsilon) = \frac{1}{8\pi\mu}\Big[\vec{f} J_1(r, \epsilon) + \big(\vec{f} \cdot \vec{r}\big)\vec{r} J_2(r, \epsilon)\Big], \tag{2.8}$$

$$\vec{U}_r(\vec{n}, \vec{r}, \epsilon) = \frac{1}{8\pi\mu}\Big[\frac{1}{2} P(r, \epsilon)\big(\vec{n} \times \vec{r}\big)\Big], \tag{2.9}$$

where $r = |\vec{r}|$. The other functions in Eqs. 2.8-2.9 are defined as below:

$$J_1(r,\epsilon) = \frac{2\epsilon^2 + r^2}{(r^2+\epsilon^2)^{3/2}}, \tag{2.10}$$

$$J_2(r,\epsilon) = \frac{1}{(r^2+\epsilon^2)^{3/2}}, \tag{2.11}$$

$$P(r,\epsilon) = \frac{5\epsilon^2 + 2r^2}{(r^2+\epsilon^2)^{5/2}}. \tag{2.12}$$

It is worth mentioning that the regularized stokeslet formulation is only used for flagella, and that is because we approximate the surface integral over the flagellum with a line distribution of forces and torques along the centerline. Such integrals are singular when the evaluation point is also on the centerline; therefore, regularization is required here to evaluate the velocity field on the flagellum and the regularization parameter corresponds to the effective radius of the flagellum. On the other hand, the weakly singular forms of the boundary integral equations are evaluated over the cell body surface, as explained in section 2.4; in other words, it is assumed that $\epsilon_B = 0$ in the presented equations. Therefore, functions in Eqs. 2.10-2.12 take a simple form in terms of r_B for the cell body.

By taking curl of the flow velocity, the angular velocity equation is obtained and simplified in the following form:

$$\vec{w}(\vec{x},t) = \frac{1}{2}\nabla\times\vec{u}(\vec{x},t) = \oint_B \vec{W}_s(\vec{f}_B,\vec{r}_B,\epsilon_B)dA + \sum_{i=1}^{N_F}\int_{\Gamma^{(i)}} \Big[\vec{W}_s(\vec{f}_F,\vec{r}_F,\epsilon_F) + \vec{W}_r(\vec{n}_F,\vec{r}_F,\epsilon_F)\Big]\, ds, \tag{2.13}$$

where $\vec{W}_s$ and $\vec{W}_r$ are respectively the angular velocities of the regularized stokeslet and rotlet, given as:

$$\vec{W}_s(\vec{f},\vec{r},\epsilon) = \frac{1}{8\pi\mu}\Big[\frac{1}{2}P(r,\epsilon)\big(\vec{f}\times\vec{r}_i\big)\Big], \tag{2.14}$$

$$\vec{W}_r(\vec{n},\vec{r},\epsilon) = \frac{1}{8\pi\mu}\left\{\frac{-1}{4}\Big[K_3(r,\epsilon)\vec{n} + K_4(r,\epsilon)\big(\vec{n}\cdot\vec{r}\big)\vec{r}\Big]\right\}. \tag{2.15}$$

The functions $K_3(r,\epsilon)$ and $K_4(r,\epsilon)$ are also defined as:

$$K_3(r\epsilon) = \frac{-4\epsilon^2 + 2r^2}{(r^2+\epsilon^2)^{5/2}}, \tag{2.16}$$

$$K_4(r\epsilon) = \frac{-6}{(r^2+\epsilon^2)^{5/2}}. \tag{2.17}$$

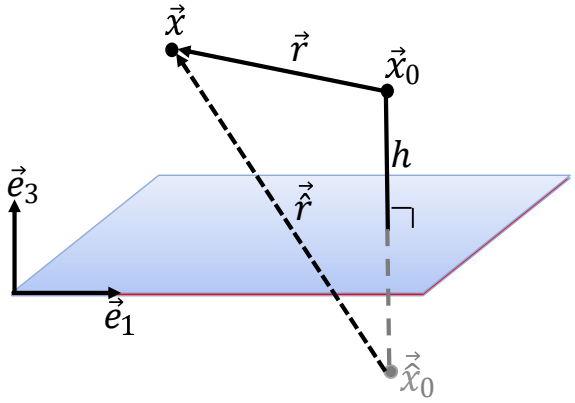

Figure 2.1: The image system to satisfy no-slip boundary condition on the planar boundary. An image point across the planar boundary is considered to satisfy this condition. The point force and torque are applied at $\vec{x}_0$ and the image point associated with $\vec{x}_0 = (x_0, y_0, h)$ is $\vec{\hat{x}}_0 = (x_0, y_0, -h)$. $\vec{x}$ is the evaluation point of the velocity and angular velocity fields.

The translational and angular velocities of the regularized stokeslet and rotlet developed thus far are based on Green's function in the absence of any boundary. In this thesis, we study bacterial locomotion near a planar surface as well. Therefore, a revised version of Green's function is required to satisfy the no-slip boundary condition on the plane boundary. In this regard, the image system is employed here to enforce this boundary condition into the model. The idea behind the image system is to assume an image point across the planar boundary (see Fig. 2.1), apply the singular solutions of the Stokes equations at that image point, and use the linear combination of the singular solutions for the real point and its image, so that the flow velocity becomes zero at the wall. Following the scheme of Cortez et al. [24], the translational and angular velocities at the evaluation point $\vec{r}$ due to a regularized stokeslet and rotlet (i.e. $\vec{U}_s$, $\vec{U}_r$ in Eqs. 2.8-2.9 and $\vec{W}_s$, $\vec{W}_r$ in Eqs. 2.14-2.15) in the image system are revised as:

$$\vec{U}_s(\vec{f},\vec{r},\hat{\vec{r}},\epsilon) = \frac{1}{8\pi\mu}\Bigg\{\Big[\vec{f}J_1(r,\epsilon) + \big(\vec{f}\cdot\vec{r}\big)\vec{r}J_2(r,\epsilon)\Big] - \Big[\vec{f}J_1(\hat{r},\epsilon) + \big(\vec{f}\cdot\hat{\vec{r}}\big)\hat{\vec{r}}J_2(\hat{r},\epsilon)\Big]$$
$$+ h^2\Big[-\big(\vec{b}\cdot\hat{\vec{r}}\big)\hat{\vec{r}}K_2(\hat{r},\epsilon) - \vec{b}\,K_1(\hat{r},\epsilon)\Big] + 2h\Big[\big(\vec{b}\cdot\vec{e}_3\big)\hat{\vec{r}}J_2(\hat{r},\epsilon)$$
$$+ \big(\hat{\vec{r}}\cdot\vec{b}\big)\vec{e}_3\big(J_3(\hat{r},\epsilon) - J_2(\hat{r},\epsilon)\big) + \big(\hat{\vec{r}}\cdot\vec{e}_3\big)\vec{b}J_2(\hat{r},\epsilon)$$
$$+ \frac{1}{2}\big(\hat{\vec{r}}\cdot\vec{e}_3\big)\big(\hat{\vec{r}}\cdot\vec{b}\big)\hat{\vec{r}}K_2(\hat{r},\epsilon)\Big] + 2hJ_3(\hat{r},\epsilon)\big(\vec{m}\times\hat{\vec{r}}\big)\Bigg\}, \tag{2.18}$$

$$\vec{U}_r(\vec{n},\vec{r},\hat{\vec{r}},\epsilon) = \frac{1}{8\pi\mu}\Bigg\{\frac{1}{2}\Big[P(r,\epsilon)\big(\vec{n}\times\vec{r}\big) - P(\hat{r},\epsilon)\big(\vec{n}\times\hat{\vec{r}}\big)\Big] + h\Big[\vec{p}K_1(\hat{r},\epsilon) + \big(\vec{p}\cdot\hat{\vec{r}}\big)\hat{\vec{r}}K_2(\hat{r},\epsilon)\Big]$$
$$- \Bigg[\Big[\big(\vec{p}\cdot\hat{\vec{r}}\big)\vec{e}_3 + \big(\vec{e}_3\cdot\hat{\vec{r}}\big)\vec{p}\Big]J_3(\hat{r},\epsilon) + \big(\vec{e}_3\cdot\hat{\vec{r}}\big)\big(\vec{p}\cdot\hat{\vec{r}}\big)\hat{\vec{r}}K_2(\hat{r},\epsilon)\Big] - J_3(\hat{r},\epsilon)\big(\vec{q}\times\hat{\vec{r}}\big)$$
$$+ h^2\,J_4(\hat{r},\epsilon)\big(\vec{n}\times\hat{\vec{r}}\big) - h\Big[\vec{p}J_3(\hat{r},\epsilon) + \big(\vec{e}_3\cdot\hat{\vec{r}}\big)\big(\vec{n}\times\hat{\vec{r}}\big)J_4(\hat{r},\epsilon)\Big]\Bigg\}, \tag{2.19}$$

$$\vec{W}_s(\vec{f},\vec{r},\hat{\vec{r}},\epsilon) = \frac{1}{8\pi\mu}\Bigg\{1/2\Big[P(r,\epsilon)\big(\vec{f}\times\vec{r}\big) - P(\hat{r},\epsilon)\big(\vec{f}\times\hat{\vec{r}}\big)\Big] + h^2J_4(\hat{r},\epsilon)\big(\vec{b}\times\hat{\vec{r}}\big) + h\Big[K_2(\hat{r},\epsilon)$$
$$- J_4(\hat{r},\epsilon)\Big]\big(\vec{b}\cdot\hat{\vec{r}}\big)\big(\vec{e}_3\times\hat{\vec{r}}\big) + h\Big[\vec{m}\Big[\hat{r}^2J_4(\hat{r},\epsilon) + 2J_3(\hat{r},\epsilon)\Big] - J_4(\hat{r},\epsilon)\big(\vec{m}\cdot\hat{\vec{r}}\big)\hat{\vec{r}}\Big]$$
$$+ hP(\hat{r},\epsilon)\vec{m}\Bigg\}, \tag{2.20}$$

$$\begin{aligned}\vec{W}_r(\vec{n},\vec{r},\vec{\hat{r}},\epsilon) =& \frac{1}{8\pi\mu}\Bigg\{\frac{-1}{4}\Big[K_3(r,\epsilon)\vec{n}+K_4(r,\epsilon)\big(\vec{n}\cdot\vec{r}\big)\vec{r}-K_3(\hat{r},\epsilon)\vec{n}-K_4(\hat{r},\epsilon)\big(\vec{n}\cdot\vec{\hat{r}}\big)\vec{\hat{r}}\Big]\\ &+\big(\vec{p}\cdot\vec{\hat{r}}\big)\big(\vec{e}_3\times\vec{\hat{r}}\big)+\frac{1}{2}\Big[J_4(\hat{r},\epsilon)-K_2(\hat{r},\epsilon)\Big]\big(\vec{e}_3\cdot\vec{\hat{r}}\big)\big(\vec{p}\times\vec{\hat{r}}\big)\\ &-hJ_4(\hat{r},\epsilon)\big(\vec{p}\times\vec{\hat{r}}\big)-\frac{1}{2}\Big[\hat{r}^2J_4(\hat{r},\epsilon)+2J_3(\hat{r},\epsilon)\Big]\vec{q}+\frac{1}{2}J_4(\hat{r},\epsilon)\big(\vec{q}\cdot\vec{\hat{r}}\big)\vec{\hat{r}}\\ &-\frac{h}{2}\Bigg[\Big[\hat{r}^2J_5(\hat{r},\epsilon)+3J_4(\hat{r},\epsilon)\Big]\big(\vec{e}_3\cdot\vec{\hat{r}}\big)\vec{n}-J_4(\hat{r},\epsilon)\Big[\big(\vec{n}\cdot\vec{e}_3\big)\vec{\hat{r}}+\big(\vec{p}\times\vec{\hat{r}}\big)\Big]\\ &-J_5(\hat{r},\epsilon)\big(\vec{e}_3\cdot\vec{\hat{r}}\big)\big(\vec{n}\cdot\vec{\hat{r}}\big)\vec{\hat{r}}\Bigg]+\frac{h^2}{2}\Bigg[\vec{n}\Big[2J_4(\hat{r},\epsilon)+\hat{r}^2J_5(\hat{r},\epsilon)\Big]\\ &-J_5(\hat{r})\big(\vec{n}\cdot\vec{\hat{r}}\big)\vec{\hat{r}}\Bigg]\Bigg\},\end{aligned}\tag{2.21}$$

where $\vec{\hat{r}}$ connects the image point to the evaluation point and

$$\vec{b} = 2(\vec{f}\cdot\vec{e}_3)\vec{e}_3-\vec{f},\tag{2.22}$$

$$\vec{m} = \vec{f}\times\vec{e}_3,\tag{2.23}$$

$$\vec{p} = \vec{n}\times\vec{e}_3,\tag{2.24}$$

$$\vec{q} = \vec{n}-(\vec{n}\cdot\vec{e}_3)\vec{e}_3,\tag{2.25}$$

$$J_3(r,\epsilon) = \frac{-3\epsilon^2}{(r^2+\epsilon^2)^{5/2}},\tag{2.26}$$

$$J_4(r,\epsilon) = \frac{15\epsilon^2}{(r^2+\epsilon^2)^{7/2}},\tag{2.27}$$

$$J_5(r,\epsilon) = \frac{-105\epsilon^2}{(r^2+\epsilon^2)^{9/2}},\tag{2.28}$$

$$K_1(r,\epsilon) = \frac{-10\epsilon^4+7\epsilon^2r^2+2r^4}{(r^2+\epsilon^2)^{7/2}},\tag{2.29}$$

$$K_2(r,\epsilon) = \frac{-21\epsilon^2-6r^2}{(r^2+\epsilon^2)^{7/2}}.\tag{2.30}$$

2.3 Elasticity

In our model, the flagella are flexible filaments rotated by independent motors, and their shapes and positions change over time. Generally, a time-dependent curve in a three-

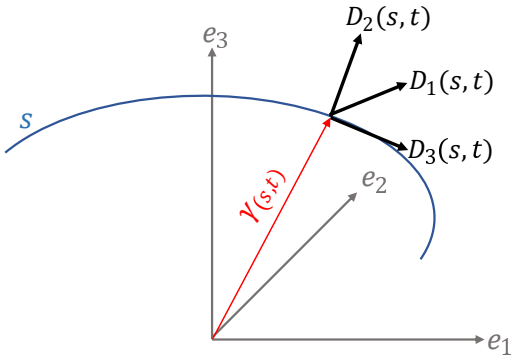

Figure 2.2: Configuration of a space curve as the flagella centerline.

dimensional space can be defined by a continuously differentiable vector-valued function γ [19]:

$$\gamma : I \times \mathbb{R}_+ \subset \mathbb{R} \times \mathbb{R}_+ \to \mathbb{E}^3. \tag{2.31}$$

This function maps any open interval $I \in \mathbb{R}$ into Euclidean space $\mathbb{E}^3$ at time t. In fact, for each $s \in I$ the vector $\vec{\gamma}(s,t)$ gives the position of the point specified by s at t. We assume that the parameter s represents the arc length and the curve $\vec{\gamma}(s,t)$ is a regular curve, i.e. $\vec{\gamma}'(s,t) \neq 0$ (derivative with respect to s). By this definition, the unit tangent vector to the curve $\vec{\gamma}$ is $\vec{\tau}(s,t) = \vec{\gamma}'(s,t)$ for any $s \in I$.

To describe the orientation of the material points in the cross-section of flagella at s, we need to introduce a right-handed orthonormal frame $\left\{\vec{D}_1(s,t), \vec{D}_2(s,t), \vec{D}_3(s,t)\right\}$ which specifies the orientation at each s, as shown in Fig. 2.2. Since the flagella in our model are inextensible, unshearable, we assume that $\vec{D}_3(s,t)$ is always the tangent vector to the curve γ [i.e. $\vec{D}_3(s,t) = \tau(s,t)$] to simplify the model. As we move along the arc-length s the frame $\left\{\vec{D}_1(s,t), \vec{D}_2(s,t), \vec{D}_3(s,t)\right\}$ changes smoothly with respect to a frame $\{\vec{e}_1, \vec{e}_2, \vec{e}_3\}$. In this regard, the evolution of $\left\{\vec{D}_1(s,t), \vec{D}_2(s,t), \vec{D}_3(s,t)\right\}$ with respect to the arc-length s and time t can be found by [42]

$$\vec{D}_i'(s,t) = \vec{\kappa}(s,t) \times \vec{D}_i(s,t), \tag{2.32}$$

$$\dot{\vec{D}}_i(s,t) = \vec{\omega}(s,t) \times \vec{D}_i(s,t). \tag{2.33}$$

Where $(')$ and $(\dot{})$ stand for derivatives with respective to arc-length and time, respectively,

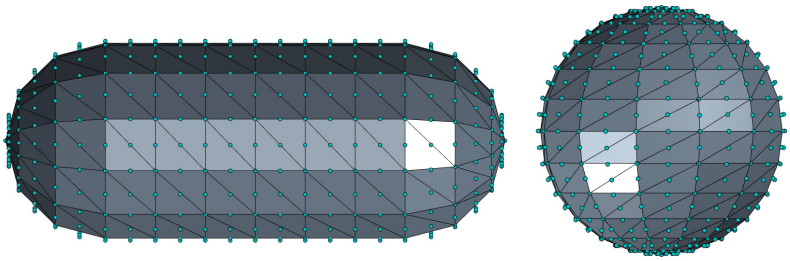

Figure 2.3: The cell body surface is covered by curved triangular elements. Each triangle element is defined by three nodes at the vertices and three nodes at the middle of the edges

and $\vec{\kappa}(s,t)$ and $\vec{\omega}(s,t)$ are the twist and spin vectors.

The hydrodynamic forces exerted on the flagellar filaments deform the flagella out of their static equilibrium configurations. To model the deformations, we use the standard Kirchhoff rod model and assume that the flagella are inextensible, unshearable, and only allowed to bend and twist. If the centerline of the flagella at the rest configuration is represented by the space curve $\vec{\gamma}(s)$, and the orientation of the local orthonormal triads is denoted by the twist vector $\hat{\vec{\kappa}}(s)$, based on the linear theory of elasticity, the internal moments $\vec{N}(s,t)$ transmitted along the flagella can be computed by

$$\vec{N}(s,t) = EI\Big[(\kappa_1(s,t)-\hat{\kappa_1}(s))\vec{D}_1(s,t)+(\kappa_2(s,t)-\hat{\kappa_2}(s))\vec{D}_2(s,t)+\Upsilon(\kappa_3(s,t)-\hat{\kappa_3}(s))\vec{D}_3(s,t)\Big], \tag{2.34}$$

where $\vec{\kappa}(s,t) = (\kappa_1, \kappa_2, \kappa_3)$ is the twist vector at point s and time t, and $\Upsilon = \frac{GJ}{EI}$ is the ratio of twisting stiffness GJ to bending stiffness EI. In this thesis, we assume that the flagella are homogeneous, isotropic and $\Upsilon = 1$[87, 88].

2.4 Discretization

To evaluate the boundary integral equations (i.e. Eqs. 2.7 and 2.13) over the cell body surface (B), a finite number (N_B) of triangular elements is generated on the cell body surface. To yield better accuracy, a tessellation of curved triangles is used to cover the cell body surface, where six nodes are required to construct an element. Three nodes are vertices and the other three nodes are in the middle of the three edges (see Fig. 2.3). We aim to use the Gauss-Legendre quadrature method to evaluate the integrals over the

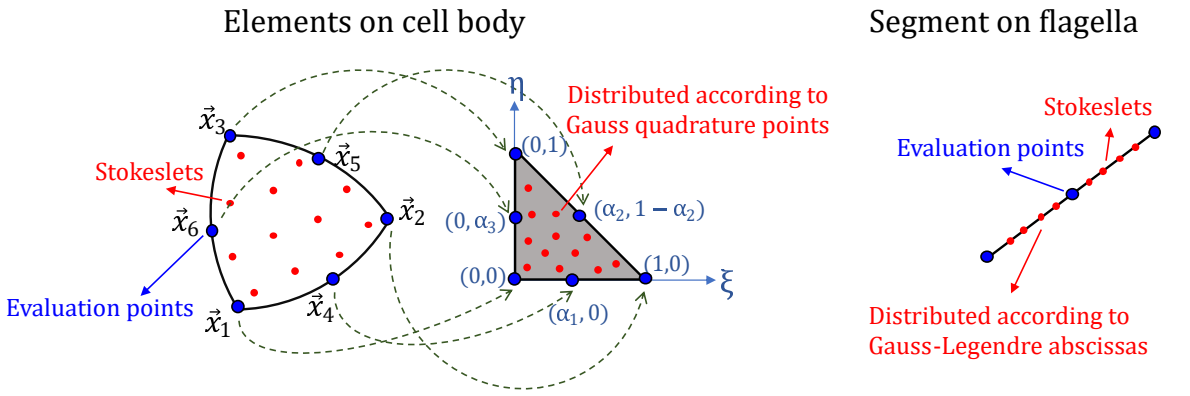

Figure 2.4: Each triangular element on the cell body is mapped to a right-angled isosceles in $\xi - \eta$ parameter space. Gauss points on a standard triangle are used to describe the distribution of the force densities on the elements. The force and torque densities along each segment of the flagella are distributed according to Gauss-Legendre abscissas.

elements. In this regard, we fit a quadratically varying force density on each triangular element and map the surface of the triangles to a right-angled isosceles in $\xi - \eta$ parameter space, following Pozrikidis's scheme [90]. In this scheme, the mapping from the physical elements to a standard element is mediated by:

$$\vec{x} = \sum_{i=1}^{6} \vec{x}_i \phi_i(\xi, \eta). \tag{2.35}$$

where $\phi_i(\xi, \eta)$ are the cardinal interpolation functions defined as:

$$\begin{aligned}
\phi_2 &= \frac{1}{1-\alpha_1}\xi(\xi - \alpha_1 + \frac{\alpha_1 - \alpha_2}{1-\alpha_2}\eta), \\
\phi_3 &= \frac{1}{1-\alpha_3}\eta(\eta - \alpha_3 + \frac{\alpha_3 + \alpha_2 - 1}{\alpha_2}\xi), \\
\phi_4 &= \frac{1}{\alpha_1(1-\alpha_1)}\xi(1 - \xi - \eta), \\
\phi_5 &= \frac{1}{\alpha_2(1-\alpha_2)}\xi\eta, \\
\phi_6 &= \frac{1}{\alpha_3(1-\alpha_3)}\eta(1 - \xi - \eta), \\
\phi_1 &= 1 - \phi_2 - \phi_3 - \phi_4 - \phi_5 - \phi_6,
\end{aligned} \tag{2.36}$$

and

$$\alpha_1 = \frac{1}{1+\frac{|\vec{x}_4-\vec{x}_2|}{|\vec{x}_4-\vec{x}_1|}}, \quad \alpha_2 = \frac{1}{1+\frac{|\vec{x}_6-\vec{x}_3|}{|\vec{x}_6-\vec{x}_1|}}, \quad \alpha_3 = \frac{1}{1+\frac{|\vec{x}_5-\vec{x}_2|}{|\vec{x}_5-\vec{x}_3|}}. \tag{2.37}$$

If $\vec{x}_4$, $\vec{x}_5$ and $\vec{x}_6$ are located at the middle of the edges then $\alpha_1 = \alpha_2 = \alpha_3 = 0.5$ and $\phi_i(\xi, \eta)$ are simplified to:

$$\begin{aligned} &\phi_1 = (1-\xi-\eta)(2-2\xi-2\eta-1), \quad &&\phi_2 = \xi(2\xi-1), \quad &&\phi_3 = \eta(2\eta-1), \\ &\phi_4 = 4\xi(1-\xi-\eta), &&\phi_5 = 4\xi\eta, &&\phi_6 = 4\eta(1-\xi-\eta). \end{aligned} \tag{2.38}$$

Unlike a flat triangle, the surface metric at a point on the curved surface is not constant and is calculated by:

$$h_s(\xi, \eta) = |\vec{e}_\xi \times \vec{e}_\eta| = \left| \frac{\partial \vec{x}}{\partial \xi} \times \frac{\partial \vec{x}}{\partial \eta} \right|. \tag{2.39}$$

At the end, the integral of the function $g(\vec{x})$ (here $\vec{U}_s, \vec{W}_s$) over a curved triangular CT element is given by:

$$\int_{C_T} g(\vec{x}) dA(\vec{x}) = \int_0^1 \int_0^{1-\xi} g[\vec{x}(\xi, \eta)] h_s(\xi, \eta) d\eta \, d\xi. \tag{2.40}$$

The force densities $\vec{f}$ appear in the integrand of all the integrals over the curved triangles. We can assume that the force density quadratically vary with respect to the local triangle and use the same interpolation functions $\phi(\xi, \eta)$ to approximate it as before. Therefore, the jth component of the force density at each element can be written as:

$$f^{(j)}(\xi, \eta) = \sum_{i=1}^{6} f_i^{(j)} \phi_i(\xi, \eta), \tag{2.41}$$

where $f_i^{(j)}$ is the jth component of the force density at the ith evaluation point of a triangular element.

Each hook and filament in our model is respectively discretized into N_{H} and N_{S} connected equal-length straight rods called segments. We assume that the stokeslet and rotlet vary along each segment, and a second-order polynomial interpolation is employed to express the stokeslet/rotlet strengths along a segment in terms of the nodal force/torque densities at the evaluation points, located at the middle and ends of each segment (blue points in Fig. 2.4).

2.4.1 Gaussian quadrature method

According to the Gaussian quadrature method the integral of a function $g(x)$ over the range $[-1, 1]$ is approximated by:

$$\int_{-1}^{1} g(x)dx \approx \sum_{q=1}^{N_Q} g(x^q)\omega^q, \tag{2.42}$$

where we evaluate the function at N_Q Gauss-Legendre abscissas denoted by x^q and use appropriate weightings for each evaluation. Table of Gauss-Legendre abscissas (x^q) and weightings (ω^q) can be found in [31].

By scaling the interval length, this method can be used for more general intervals. In one-dimensional integrals, the scaling can be done in the following form:

$$\int_{a_l}^{a_u} g(x)dx \approx \frac{a_u - a_l}{2} \sum_{q=1}^{N_Q} g(x^q)\omega^q, \tag{2.43}$$

where $x^q = \frac{a_u+a_l}{2} + x_n^q \cdot \frac{a_u-a_l}{2}$, x_n^q and ω^q are standard Gauss-Legendre abscissas and weightings. In this thesis, we use this method to evaluate the boundary integral equations over each segment of the flagella.

Similarly, the integral of a function $g(\vec{x})$ over a standard triangle $\Delta = \{(\xi, \eta)|\xi \geq 0, \eta \geq 0, \xi + \eta \leq 1\}$ is approximated by:

$$\int_{\Delta} g[\vec{x}(\xi, \eta)]dA \approx \frac{1}{2} \sum_{q=1}^{N_Q} g[\vec{x}(\xi^q, \eta^q)]\omega^q, \tag{2.44}$$

where the function $g(\vec{x})$ is evaluated at N_Q quadrature points (ξ^q, η^q) and multiplied by the corresponding weightings ω^q. The table of the pairs (ξ^q, η^q) and weightings ω^q for triangular quadrature scheme is available at [33]. In order to evaluate the integral over a general triangular element, it is necessary that the surface of the triangle is mapped to a right-angled isosceles in $\xi - \eta$ parameter space.

The first integral in Eq. 2.7 is weakly singular when the evaluation point $\vec{x}$ lies on the body B due to the singularity of the kernels Eqs. 2.10, and 2.11 when $r = 0$ and $\epsilon = 0$. This motivates us to distinguish between non-singular boundary elements of B and singular elements of B In particular, when the evaluation point (blue points in Fig. 2.4) lies on a triangular element we evaluate the integral over, that element is known as singular. Otherwise, the element is non-singular. We apply different numerical schemes to each group of triangles, to resolve the singularity and yield better accuracy.

2.4.2 Non-singular triangle

We use the triangular quadrature scheme to integrate the non-singular curved triangles (CT). In this regard, the two-dimensional integrals are approximated by:

$$\int_{C_T} g(\vec{x})dA(\vec{x}) = \int_0^1 \int_0^{1-\xi} g[\vec{x}(\xi,\eta)]h_s(\xi,\eta)d\eta\, d\xi \approx \frac{1}{2}\sum_{q=1}^{N_Q} g(\vec{x}^q)h_s(\xi^q,\eta^q)\omega^q. \tag{2.45}$$

In this expression, the value of function $g(\vec{x})$ ($\vec{U}_s$ and $\vec{W}_s$ in boundary integral equations) is evaluated at the qth quadrature point, and each contribution to the quadrature is scaled by h_s reflects the transformation from the curved elements to the standard triangle (i.e. $\vec{x}^q \rightarrow [\xi^q, \eta^q]$.

2.4.3 Singular triangle

When $\vec{U}_s$ and $\vec{W}_s$ are evaluated at the evaluation points (blue points in Fig. 2.4), they exhibit $O(\frac{1}{r})$ singularities, where r represents the distance from a stokeslet to an evaluation point. This singularity is due to the characteristic of the Green's function in solving Laplace's equation in three dimensions.

Suppose that the singularity is lied at one vertex, say $\vec{x}_1$, of the curved triangle. Without loss of generality, we can assume that this vertex corresponds to the vertex $\eta = \xi = 0$ in the standard triangle. After the transformation to the standard triangle, we change the coordinate system to polar. With our assumption, the integral over a curved triangle can be written in the following form:

$$I = \int_{C_T} \frac{q(\vec{x})}{r(\vec{x})} dA, \tag{2.46}$$

where $r(\vec{x}) = |\vec{x} - \vec{x}_1|$. If we transform the integral into the standard triangle, we obtain the following double integral:

$$I = \int_0^1 \int_0^{1-\xi} \frac{h_s(\xi,\eta)q(\vec{x}(\xi,\eta))}{r(\vec{x}(\xi,\eta))} d\eta d\xi. \tag{2.47}$$

By change the coordinate system to polar, and defining $\xi = \rho\cos(\theta)$ and $\eta = \rho\sin(\theta)$, the integral can be expressed as:

$$I = \int_0^{\frac{\pi}{2}} \int_0^{R(\theta)} \frac{h_s(\rho,\theta)q(\vec{x}(\rho,\theta))}{r(\vec{x}(\rho,\theta))} \rho\, d\rho d\theta, \tag{2.48}$$

where $R(\theta) = 1/[\cos(\theta)+\sin(\theta)]$. In Eq. 2.48, the inner and outer integrals can be accurately computed by two sequential Gauss-Legendre quadratures in one dimension. In this regard, the distribution of ρ and θ is required to be based on standard Gauss-Legendre abscissas in the standard triangle. According to this distribution, many numbers of the stokeslets are located close to the evaluation point which increases the accuracy of the integration over the singular elements (see Fig. 2.5A). By applying these rules, the integral is approximated by:

$$I = \frac{\pi}{8} \sum_{i=1}^{N_Q} \frac{\omega^i}{\cos(\theta^i) + \sin(\theta^i)} \sum_{j=1}^{N_Q} \omega^j (\frac{h_s^{ij} \rho^{ij}}{r^{ij}}) q^{ij}, \tag{2.49}$$

where

$$\theta^i = \frac{\pi}{4}(1 + x^i), \tag{2.50}$$

$$\rho^{ij} = \frac{1}{2[\cos(\theta^i) + \sin(\theta^i)]}(1 + x^j), \tag{2.51}$$

x^i,x^j, ω^i and ω^j are standard Gauss-Legendre abscissas and the corresponding weightings. If the original element is a standard triangle, then r and ρ can be canceled out from the numerator and denominator of the integrand, and therefore the singularity disappears. In a general triangular element, the ratio $(h_s^{ij}\rho^{ij}/r^{ij})$ is about unity as long as the quality of the meshing on the cell body is good. Therefore, we do not have a large numerical error due to the integrand singularity.

If the singularity is located at a point on the edge, the element is divided into four descendant triangles as shown in Fig. 2.5B. In this division, one element ④ is a non-singular element, and three other elements (①-③) are singular. Depending on the condition, the schemes mentioned above are applied to each sub-triangle separately.

2.4.4 Construct a system of linear equations

As stated so far, we apply the Gauss-Legendre quadrature method to evaluate the boundary integral equations (Eqs. 2.7,2.13) over the cell body and along the flagella. Moreover, we use the proper interpolation functions to express the stokeslets and rotlets at the Gauss points along the segments in terms of the force/torque densities at the evaluation points. If we let $N_{\mathrm{P_B}}$ denote the number of evaluation points (blue points in Fig. 2.4) on the cell body and $N_{\mathrm{P_F}} = 2(N_{\mathrm{H}}+N_{\mathrm{S}})+1$ denotes the number of evaluation points on each flagellum,

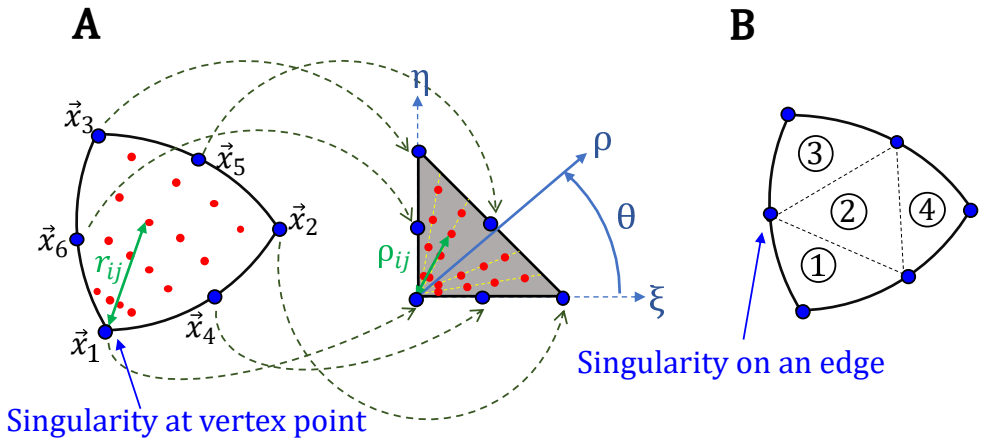

Figure 2.5: A) If the singularity is at a vertex of a singular element, the integral is transformed into the polar coordinate to yield better accuracy. B) If the singularity is at a point on the edge, the element is divided into four descendant triangles which results in three singular elements and one non-singular element.

the boundary integral equations 2.7 and 2.13 can be summarized as:

$$\begin{bmatrix} \vec{u}_1 \\ \vdots \\ \vec{u}_{N_{\mathrm{P_B}}+N_{\mathrm{F}}\cdot N_{\mathrm{P_F}}} \\ \vec{\omega}_1 \\ \vdots \\ \vec{\omega}_{N_{\mathrm{F}}\cdot N_{\mathrm{P_F}}} \end{bmatrix} = \begin{bmatrix} A_1 \\ A_2 \end{bmatrix} \begin{bmatrix} \vec{f}_1 \\ \vdots \\ \vec{f}_{N_{\mathrm{P_B}}+N_{\mathrm{F}}\cdot N_{\mathrm{P_F}}} \\ \vec{n}_1 \\ \vdots \\ \vec{n}_{N_{\mathrm{F}}\cdot N_{\mathrm{P_F}}} \end{bmatrix}, \tag{2.52}$$

where $\vec{u}_i$ is the translational velocity of ith evaluation point on the cell body and flagella, and $\vec{\omega}_j$ is the angular velocity of jth evaluation point on the flagella. A_1 and A_2 are dense matrices with dimensions of $3(N_{\mathrm{P_B}} + N_{\mathrm{F}} \cdot N_{\mathrm{P_F}}) \times 3(N_{\mathrm{P_B}} + 2N_{\mathrm{F}} \cdot N_{\mathrm{P_F}})$ and $3(N_{\mathrm{F}} \cdot N_{\mathrm{P_F}}) \times 3(N_{\mathrm{P_B}} + 2N_{\mathrm{F}} \cdot N_{\mathrm{P_F}})$ constructed based on the coefficients in Eqs. 2.7 and 2.13, the mapping and the interpolation matrices. Constructing the matrices A_1 and A_2 is the most time-consuming process in our numerical scheme at each time step. In this process, the pairwise distances between all the evaluation points and the stokeslets, and subsequently the kernels of the boundary integral equations are calculated. The computational cost of this process quadratically increases with the product of the number of evaluation points and the number of stokeslets.

2.4.5 Discretization of channel walls

To study the locomotion of the model bacteria inside a rectangular channel, we need to discretize the four walls of the channel and evaluate the boundary integral equations over the channel surfaces in addition to over the bacteria components. In this respect, the surface of the walls is covered by flat triangular elements and the singular form of the boundary integral equations are evaluated over them. Moreover, the edges of the channel are filleted to maintain a continuously varying normal vector. This avoids singular solutions of the stokeslet distribution, which may reduce the results' accuracy. A mesh gradient is defined along the channel to reduce computational costs. In the gradient, the grids away from the bacterium are coarse and the grids close to the cell body are fine.

The channel is stationary with respect to the model bacterium (zero velocity), but depending on the position of the model bacterium at each time step, we move the channel in $\vec{X}$ direction to ensure that the closest regions to the bacterium have always fine grids. In addition to the $\vec{X}$ direction, we have defined gradients in $\vec{Y}$ and $\vec{Z}$ directions such that the center of the gradient is updated by the position of the model bacterium in YZ plane. This adaptive meshing method is a great way to ensure accuracy by guaranteeing that the surfaces close to the bacterium are covered by fine grids. Some stokeslets with zero velocity on the channel walls reflect the walls' effect on the model bacterium and the fluid flow inside the channel. The schemes used to evaluate the integral over the elements on the walls are exactly the same as the cell body's schemes. The only difference is that the elements on the cell body have unknown transnational velocities, whereas the velocity of the elements on the walls are always zero. Consequently, equation 2.52 is modified to:

$$\begin{bmatrix} \vec{u}_1 \\ \vdots \\ \vec{u}_{N_{\mathrm{P_B}}+N_{\mathrm{F}}\cdot N_{\mathrm{P_F}}} \\ \vec{0}_1 \\ \vdots \\ \vec{0}_{N_{\mathrm{P_W}}} \\ \vec{\omega}_1 \\ \vdots \\ \vec{\omega}_{N_{\mathrm{F}}\cdot N_{\mathrm{P_F}}} \end{bmatrix} = \begin{bmatrix} A_1 \\ A_2 \end{bmatrix} \begin{bmatrix} \vec{f}_1 \\ \vdots \\ \vec{f}_{N_{\mathrm{P_B}}+N_{\mathrm{F}}\cdot N_{\mathrm{P_F}}+N_{\mathrm{P_W}}} \\ \vec{n}_1 \\ \vdots \\ \vec{n}_{N_{\mathrm{F}}\cdot N_{\mathrm{P_F}}} \end{bmatrix}, \tag{2.53}$$

where $N_{\mathrm{P_W}}$ represents the number of the evaluation points on the walls. The dimensions of matrices A_1 and A_2 change to $3(N_{\mathrm{P_B}} + N_{\mathrm{P_W}} + N_{\mathrm{F}} \cdot N_{\mathrm{P_F}}) \times 3(N_{\mathrm{P_B}} + N_{\mathrm{P_W}} + 2N_{\mathrm{F}} \cdot N_{\mathrm{P_F}})$ and $3(N_{\mathrm{F}} \cdot N_{\mathrm{P_F}}) \times 3(N_{\mathrm{P_B}} + N_{\mathrm{P_W}} + 2N_{\mathrm{F}} \cdot N_{\mathrm{P_F}})$, respectively.

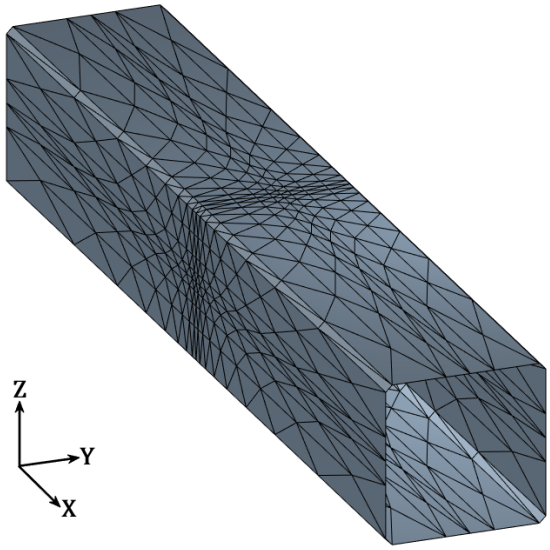

Figure 2.6: The surface of the rectangular channel is covered by flat triangular elements. The adaptive meshing method is employed to reduce the computational cost and maintain the accuracy of the numerical solution.

2.4.6 Discretization of flagella

We discretize each hook and filament into N_{H} and N_{S} segments, respectively, by introducing uniform intervals $\Delta s_{\mathrm{H}} = l_{\mathrm{H}}/N_{\mathrm{H}}$ and $\Delta s_{\mathrm{F}} = (l - l_{\mathrm{H}})/N_{\mathrm{S}}$ of the Lagrangian variable s. The length of the hook is l_H and the total length of the flagellum (hook and filament) is l. Following the scheme presented in section 2.3, the triads $\vec{D}_{\hat{i}}^{(i)n}$ ($n = 1, 2, ..., N_{\mathrm{H}} + N_{\mathrm{S}}$, $\hat{i} = 1, 2, 3$, $i = 1, ..., N_{\mathrm{F}}$), which are updated over the time as the segments rotate, are employed in our model to represent the orientation of the nth segment of the ith flagellum (see Figs. 2.7 and 2.8). The segment with index $n = N_{\mathrm{H}}$ is the last segment of the hook and index $n = N_{\mathrm{H}} + 1$ represents the first segment of the filament. Since the segments on the hook are identical in length, the principal square root of the rotation matrix $M^{(i)n}$ that maps the triad $\{\vec{D}_{\hat{i}}^{(i)n}\}$ to the triad $\{\vec{D}_{\hat{i}}^{(i)n+1}\}$ is used to describe the orientation at the joint between neighboring segments (see Fig. 2.7A). A similar technique is applied to the segments on the filament.

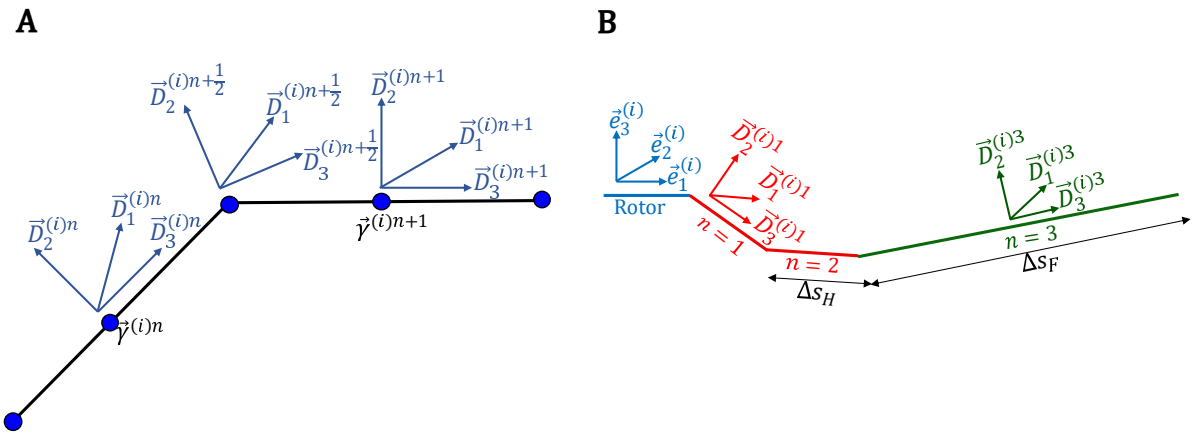

Figure 2.7: A) Positions $\vec{\gamma}^{(i)j}$ and triads $\{\vec{D}_{\hat{j}}^{(i)j},\ \hat{j}=1,2,3\}$, at two successive segments $j=n$ and $j=n+1$ of filament i. The triad at the joint, denoted $\{\vec{D}_{\hat{j}}^{(i)n+\frac{1}{2}},\ \hat{j}=1,2,3\}$, is obtained by interpolation of the triads of the neighboring segments. B) The hook, connecting the rotor to the first segment of the filament, is discretized into $N_{\mathrm{H}}=2$ equal-length (Δs_{H}) segments.

$$M^{(i)n}=\sum_{\hat{i}=1}^{3}\vec{D}_{\hat{i}}^{(i)n+1}(\vec{D}_{\hat{i}}^{(i)n})^{T}, \tag{2.54}$$

$$\vec{D}_{\hat{i}}^{(i)n+\frac{1}{2}}=\sqrt{M^{(i)n}}\,\vec{D}_{\hat{i}}^{(i)n}. \tag{2.55}$$

By discretizing Eq. 2.34 and following Lim et al. scheme [66], the internal moments at the joints between segments are defined by:

$$N_{\hat{i}}^{(i)n+\frac{1}{2}}=E_{\varrho}I_{\varrho}\left(\frac{\vec{D}_{\hat{j}}^{(i)n+1}-\vec{D}_{\hat{j}}^{(i)n}}{\Delta s_{\varrho}}\cdot\vec{D}_{\hat{k}}^{(i)n+\frac{1}{2}}-\hat{\kappa}_{\hat{i}}^{(i)n+\frac{1}{2}}\right), \tag{2.56}$$

$$\vec{N}^{(i)n+\frac{1}{2}}=\sum_{\hat{i}=1}^{3}N_{\hat{i}}^{(i)n+\frac{1}{2}}\vec{D}_{\hat{i}}^{(i)n+\frac{1}{2}}, \tag{2.57}$$

where subscript $\varrho=H,F$ distinguishes the hook from the filament ($\varrho=H$ for segment indices $n=1,...,N_{\mathrm{H}}$ and $\varrho=F$ for $n=N_{\mathrm{H}}+1,...,N_{\mathrm{H}}+N_{\mathrm{S}}-1$); $(\hat{i},\hat{j},\hat{k})$ is any cyclic

permutation of $(1,2,3)$; $\vec{N}^{(i)n+\frac{1}{2}}$ is the internal moment transmitted from nth to $(n+1)$st segment of the ith flagellum; $\hat{\kappa}_{\hat{i}}^{(i)n+\frac{1}{2}}$ represents the twist vector's $\hat{i}$th component in the rest configuration, and $n = 1, ..., N_{\mathrm{H}} + N_{\mathrm{S}}$ denotes the segment number.

$\vec{N}^{(i)\frac{1}{2}}$ denotes the internal moment transmitted from the rotor to the first segment of the hook. In the present scheme, the magnitude and direction of $\vec{N}^{(i)\frac{1}{2}}$ are estimated by employing a sub-iterative method (explained in section 2.7) to impose the motor torque and satisfy the Kirchhoff rod model, simultaneously.

2.5 Kinematics

In this thesis, the model bacteria consist of one rigid spherical or spherocylindrical cell body, and some puller and/or pusher flagella. As a sample model and in order to introduce the different position vectors and frames used to govern the kinematic equations, a schematic view of a model bacterium with two flagella is displayed in Fig. 2.8. The cell body has centroid position denoted by $\vec{X}^{(B)}$ and orientation described by the basis $\left\{\vec{e}_1^{(B)}, \vec{e}_2^{(B)}, \vec{e}_3^{(B)}\right\}$. The first flagellum has position $\vec{X}^{(1)}$ and basis $\left\{\vec{e}_1^{(1)}, \vec{e}_2^{(1)}, \vec{e}_3^{(1)}\right\}$, and the second one has position $\vec{X}^{(2)}$ and basis $\left\{\vec{e}_1^{(2)}, \vec{e}_2^{(2)}, \vec{e}_3^{(2)}\right\}$. In this study, it is assumed that all flagella have identical physical and elastic properties and their initial and rest configurations are right-handed helices. In the proposed model bacteria, the flagella complexes, depending on the model, are driven by constant or variable torque motors. Let $\vec{U}^{(B)}$ and $\vec{\Omega}^{(B)}$ denote the translational and rotational velocity of the cell body, respectively. Let $\vec{\omega}_s^{(i)1}$ represent the angular velocity vector of the first segment of the ith flagellum relative to the cell body and $\vec{\omega}_s^{(i)n}$ denote the angular velocity of the nth segment of the ith flagellum with respect to the $(n-1)$st segment, for $n = 2, 3, ..., N_{\mathrm{H}} + N_{\mathrm{S}}$. Then, the overall instantaneous translational velocity of any given evaluation point $\vec{X}^E$ on the swimmer can be written as:

$$\vec{U}(\vec{X}^E) = \begin{cases} \vec{U}^{(B)} + \vec{\Omega}^{(B)} \times \left(\vec{X}^E - \vec{X}^{(B)}\right), & \vec{X}^E \text{ on cell body,} \\ \vec{U}^{(B)} + \vec{\Omega}^{(B)} \times \left(\vec{X}^E - \vec{X}^{(B)}\right) + \sum_{n=1}^{m} \vec{\omega}_s^{(i)n} \times \vec{X}_{\mathrm{rel}}^{(i)n}, & \vec{X}^E \text{ on } m\text{th segment of } i\text{th flagellum,} \end{cases} \tag{2.58}$$

where

$$\vec{X}_{\mathrm{rel}}^{(i)n} = \vec{X}^E - \vec{X}^{(i)} - \vec{\gamma}^{(i)n-\frac{1}{2}} \quad n = 1, 2, ..., N_{\mathrm{H}} + N_{\mathrm{S}}, \tag{2.59}$$

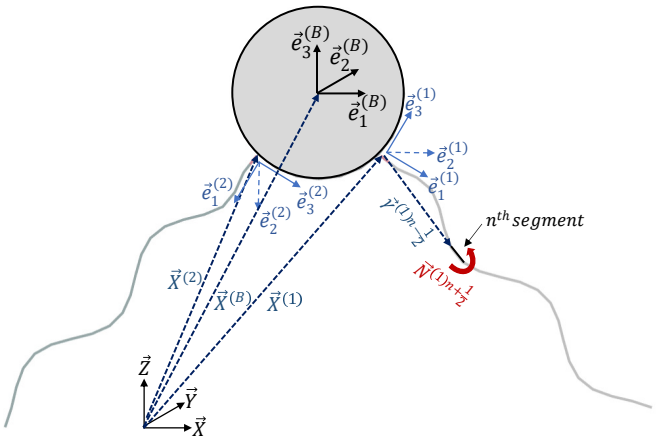

Figure 2.8: Schematic view of a model bacterium with two flagella. Several position vectors and local frames are used to define the configuration of the bacterium

and $\vec{\gamma}^{(i)n-\frac{1}{2}}$ is the position vector of the nth joint with respect to the flagellum fixed frame, as shown in Fig. 2.8. The angular velocity of any given point $\vec{X}^E$ on the flagella is written as:

$$\vec{\omega}(\vec{X}^E) = \vec{\Omega}^{(B)} + \sum_{n=1}^{m} \vec{\omega}_s^{(i)n}, \qquad \vec{X}^E \text{ on } m\text{th segment of } i\text{th flagellum.} \tag{2.60}$$

According to Eqs. 2.58 and 2.60, the translational velocities at $N_{\mathrm{P_B}}$ evaluation points on the cell body, and the translational and rotational velocities at $N_{\mathrm{F}} \cdot N_{\mathrm{P_F}}$ evaluation points on the flagella are summarized in terms of $\vec{\omega}_s^{(i)n}$, $\vec{U}^{(B)}$, and $\vec{\Omega}^{(B)}$ in the following form:

$$\begin{bmatrix} \vec{u}_1 \\ \vdots \\ \vec{u}_{N_{\mathrm{P_B}}+N_{\mathrm{F}}\cdot N_{\mathrm{P_F}}} \end{bmatrix} = A_3 \begin{bmatrix} \vec{U}^{(B)} \\ \varpi \end{bmatrix}, \qquad \begin{bmatrix} \vec{\omega}_1 \\ \vdots \\ \vec{\omega}_{N_{\mathrm{F}}\cdot N_{\mathrm{P_F}}} \end{bmatrix} = A_4 \varpi, \qquad \varpi = \begin{bmatrix} \vec{\Omega}^{(B)} \\ \vec{\omega}_s^{(1)1} \\ \vdots \\ \vec{\omega}_s^{(1)(N_{\mathrm{H}}+N_{\mathrm{S}})} \\ \vdots \\ \vec{\omega}_s^{(N_{\mathrm{F}})1} \\ \vdots \\ \vec{\omega}_s^{(N_{\mathrm{F}})(N_{\mathrm{H}}+N_{\mathrm{S}})} \end{bmatrix}. \tag{2.61}$$

The matrices A_3 and A_4 are functions of the position vectors employed in Eqs. 2.58 and 2.60. Since the position vectors vary as the model bacterium makes a progress, these matrices are updated at each time step.

2.6 Forces and torques

In addition to the hydrodynamic and elastic forces and torques, steric repulsive force and magnetic torque might be applied to the model bacteria. In particular, we apply the steric repulsive force to avoid collisions, and the magnetic torque to model the magnetotactic bacteria locomotion under an external magnetic field.

2.6.1 Steric repulsive force

When the flagella get close to each other and/or to the cell body, they likely collide. Moreover, the bacteria components are susceptible to touching the surfaces as the bacteria swim too closely. In this regard, any collision causes the model to break, therefore we apply steric repulsive forces between the components and the wall at a short-range distance to keep them away. As shown in Fig. 2.9, we apply these pairwise repulsive forces between the evaluation points on the cell body and flagella.

Following [80, 1], a truncated Lennard-Jones potential is employed here to calculate the potential energy and the corresponding repulsive forces between the nodes. Specifically, we calculate the magnitude of the repulsive force between the ith evaluation point and the wall by finding the derivative of the Lennard-Jones potential ($U^i_{LJ}(h^i)$) with respect to the vertical distance of the point from the surface (h^i). Then, this force is applied to the point in the direction of the surface's normal vector. In applying the repulsive force between the bacterium components, the magnitude of the steric repulsive force between a pair $\{i, j\}$ of the evaluation points is obtained by finding the derivative of the Lennard-Jones potential ($U^{i,j}_{LJ}(r^{i,j})$) with respect to the distance between the points ($r^{i,j}$). Then two forces in opposite directions are applied to the pair such the force vectors are coincident with the line connecting the points (see Fig. 2.9).

$$U^i_{LJ}(h^i) = \frac{F_s\sigma}{6}\left[\left(\frac{\sigma}{h^i}\right)^{12} - \left(\frac{\sigma}{h^i}\right)^{6}\right] H(2^{1/6}\sigma - h^i), \tag{2.62}$$

$$\vec{F}^i_{\text{rep}} = -\frac{dU^i_{\text{LJ}}}{dh^i}\vec{e}_3, \tag{2.63}$$

$$U^{i,j}_{LJ}(r^{i,j}) = \frac{F_s\sigma}{6}\left[\left(\frac{\sigma}{r^{i,j}}\right)^{12} - \left(\frac{\sigma}{r^{i,j}}\right)^{6}\right] H(2^{1/6}\sigma - r^{i,j}), \tag{2.64}$$

$$\vec{F}^{i,j}_{\text{rep}} = -\vec{F}^{j,i}_{\text{rep}} = -\frac{dU^{i,j}_{\text{LJ}}}{dr^{i,j}}\vec{r}^{\,i,j}. \tag{2.65}$$

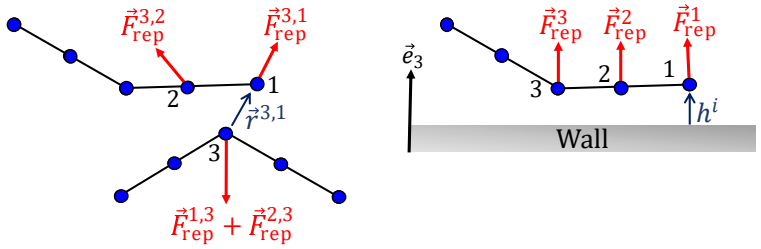

Figure 2.9: Pairwise steric repulsive forces prevent the bacteria components from touching each other. The repulsive force is also applied between the bacteria components and the walls.

We use a Heaviside step function H to restrict the range of the repulsive forces to distances less than the defined threshold $2^{1/6}\sigma$ between interacting points. In these equations, σ is the cut-off distance, and the parameter F_s is the repulsion strength. Our tests indicate that the magnitude of the repulsion strength does not have a significant impact on the locomotion of the flagella and cell body as long as it is large enough to avoid collisions. For this reason, we choose a medium value for F_s which guarantees no collision. Moreover, we choose $2^{1/6}\sigma$ fairly greater than the thickness of the filaments to ensure that the filaments do not intersect. The values for these parameters are given in each chapter, separately.

2.6.2 Magnetic torque

In the presence of a uniform magnetic field $\vec{B}$, the magnetic force on the cell body is zero and the magnetic torque is given by [130]:

$$\vec{T}_{\text{Mag}} = \vec{M}_{\text{Mag}} \times \vec{B}, \tag{2.66}$$

where $\vec{M}_{\text{Mag}}$ is the magnetic moment of the cell body. This magnetic moment is due to the presence of chains of magnetosomes, intracellular structures containing iron sulfide or iron oxide nanoparticles, inside the cell body. We non-dimensionalize the magnetic torque T_{Mag} with the motor torque in chapter 4, where the motor torque is constant.

2.6.3 Total force and torque balance

Since bacteria swim at a low Reynolds number, the inertial term is neglected. Furthermore, we assume that there is no gravity acting on the bacteria or the bacteria are neutrally buoyant and the center of the mass coincides with the center of the volume. Based on these assumptions, we impose the total torques and forces balance equations on the model [110, 106], i.e.

$$\sum_{n=1}^{N_{\mathrm{B}}} \int_{B_n} \vec{f}_{\mathrm{B}} dA_n + \sum_{i=1}^{N_{\mathrm{F}}} \sum_{n=1}^{N_{\mathrm{H}}+N_{\mathrm{S}}} \int_{\Gamma^{(i)n}} \vec{f}_{\mathrm{F}} ds_n + \sum_{i=1}^{N_{\mathrm{P_B}}+N_{\mathrm{F}}\cdot N_{\mathrm{P_F}}} \vec{F}^{i}_{\mathrm{rep}} = \vec{0}. \tag{2.67}$$

In our model, the total force balance Eq. 2.67 includes the integrals of viscous force densities over the cell body elements (first integral) and along the straight segments of the flagella (second integral). Moreover, the steric repulsive forces applied from the wall to the bacteria's components are taken into account in this equation. By applying the Gauss-Legendre quadrature method (as explained in section 2.4), these integrals are expressed in terms of the nodal force densities at the evaluation points (i.e., $\vec{f}_1, \ldots, \vec{f}_{N_{\mathrm{P_B}}+N_{\mathrm{F}}\cdot N_{\mathrm{P_F}}}$).

In the torque balance Eq. 2.68, the integrals represent the total viscous torques about the center of the cell body. The magnetic torque $\vec{T}_{\mathrm{Mag}}$, and the torques due to the steric forces $\vec{T}_{\mathrm{rep}}$ are also added to the equation. Like the force balance equation, the torque balance equation is written in terms of the nodal force and torque densities at the evaluation points (i.e., $\vec{f}_1, \ldots, \vec{f}_{N_{\mathrm{P_B}}+N_{\mathrm{F}}\cdot N_{\mathrm{P_F}}}, \vec{n}_1, \ldots, \vec{n}_{N_{\mathrm{F}}\cdot N_{\mathrm{P_F}}}$).

$$\begin{aligned}
&\sum_{n=1}^{N_{\mathrm{B}}} \int_{B_n} (\vec{\Psi} - \vec{X}^{(B)}) \times \vec{f}_{\mathrm{B}} dA_n + \sum_{i=1}^{N_{\mathrm{F}}} \sum_{n=1}^{N_{\mathrm{H}}+N_{\mathrm{S}}} \int_{\Gamma^{(i)n}} (\vec{X}^{(i)} + \vec{\gamma} - \vec{X}^{(B)}) \times \vec{f}_{\mathrm{F}} ds_n \\
&+ \sum_{i=1}^{N_{\mathrm{F}}} \sum_{n=1}^{N_{\mathrm{H}}+N_{\mathrm{S}}} \int_{\Gamma^{(i)n}} \vec{n}_{\mathrm{F}} ds_n + \vec{T}_{\mathrm{Mag}} + \vec{T}_{\mathrm{rep}} = \vec{0}.
\end{aligned} \tag{2.68}$$

To complete the system of the equations, we balance the torques about each joint of the flagella chains with the transmitted internal moment. These torque balance equations are expressed as:

$$\sum_{n=m}^{N_{\mathrm{H}}+N_{\mathrm{S}}} \left(\int_{\Gamma^{(i)n}} (\vec{\gamma} - \vec{\gamma}^{m-\frac{1}{2}}) \times \vec{f}_{\mathrm{F}} ds_n + \int_{\Gamma^{(i)n}} \vec{n}_{\mathrm{F}} ds_n + \vec{T}^{(i)2n}_{rep} + \vec{T}^{(i)2n+1}_{rep} \right) + \vec{N}^{(i)m-\frac{1}{2}} = \vec{0}, \tag{2.69}$$

where $m = 1, \ldots, N_{\mathrm{H}} + N_{\mathrm{S}}$ and $i = 1, \cdots, N_{\mathrm{F}}$. In the above equation, $\vec{T}^{(i)2n}_{rep}$ and $\vec{T}^{(i)2n+1}_{rep}$ represent the torques caused by the steric repulsive forces at $(2n)$th and $(2n+1)$st evaluation

points of ith flagellum. In fact, the torque balance Eq. 2.69 is written for all the joints we have on the flagella, thus $N_{\mathrm{F}} \cdot (N_{\mathrm{H}} + N_{\mathrm{S}})$ torque balance equations are obtained in total. These equations are also written in terms of the nodal force and torque densities at the evaluation points on the flagella.

2.7 Overview

To sum up, substituting Eq. 2.59 in Eq. 2.52 gives $3(N_{\mathrm{P_B}} + N_{\mathrm{F}} \cdot 2N_{\mathrm{P_F}})$ linear equations in which the unknowns are the components of the nodal force and torque densities at the evaluation points, the components of the angular velocities of the segments ($3(N_{\mathrm{F}} \cdot (N_{\mathrm{H}} + N_{\mathrm{S}})$) unknowns) and the components of the cell body's angular and translational velocities (6 unknowns). By adding Eqs. 2.67, 2.68 and 2.69, a solvable system of linear equations is constructed. In this thesis, `mldivide` solver (based on QR decomposition) in Matlab is used to evaluate the system of the equations and determine the unknowns.

Since quaternions have a lot of advantages over rotation matrices, they are employed in this study to transfer the parameters between the different frames of reference (Motor-fixed, body-fixed and global). We prefer the quaternions because only 4 of 9 elements in a rotation matrix are independent and so using the rotation matrix seems redundant. Moreover, the geometrical interpretation of the rotational matrix is not as obvious as the quaternion in which the rotational axis and angle can be trivially recovered. Besides these advantages, quaternions are also more efficient and straightforward in composing a sequence of rotations. As a brief definition, a quaternion q has four components and is defined as the sum of a scalar part q_0 and a vector part $\vec{q}$,

$$q = q_0 + \vec{q} = q_0 + q_1\hat{i} + q_2\hat{j} + q_3\hat{k}. \tag{2.70}$$

By using quaternion, the rotation of a vector $\vec{\nu_q} \in \mathbb{R}^3$ through an angle θ_q about a unit vector $\vec{u}_q$ (as the rotation axis) is obtained by:

$$\vec{L}_q(\vec{\nu_q}) = q\vec{\nu}_q q^*, \tag{2.71}$$

where $q^* = q_0 - q_1\hat{i} - q_2\hat{j} - q_3\hat{k}$ is the conjugate of q, and $q = q_0 + q_1\hat{i} + q_2\hat{j} + q_3\hat{k} = \cos\frac{\theta_q}{2} + \vec{u}_q \sin\frac{\theta_q}{2}$ is a unit quaternion (i.e. $\sqrt{qq^*} = 1$). More details about the quaternion algebra and their relationships with rotation matrices are available in [104, 99, 48].

If the connections between the frames are established by quaternions, the state of the model bacteria at each time step can be represented by a state vector $\vec{Q}$ defined as:

$$\vec{Q} = \left[\vec{X}^{(B)}, q^{(B)}, q^{(1)1}, \cdots, q^{(1)N_{\mathrm{H}}+N_{\mathrm{S}}}, \cdots, q^{(N_{\mathrm{F}})1}, \cdots, q^{(N_{\mathrm{F}})N_{\mathrm{H}}+N_{\mathrm{S}}}\right] \tag{2.72}$$

where $q^{(B)}$ represents the orientation of the cell body with respect to the global frame and $q^{(i)j}$, $i = 1, \cdots, N_{\mathrm{F}}$ and $j = 1, \cdots, N_{\mathrm{H}} + N_{\mathrm{S}}$, represent the orientations of the segments of the flagella with respect to the body frame. The state vector $\vec{Q}$ evolves over time according to the system of ODEs

$$\dot{\vec{X}}^{(B)} = \vec{U}^{(B)}, \quad \dot{q}^{(B)} = \frac{1}{2} W(q^{(B)}) \vec{\Omega}^{(B)}, \quad \dot{q}^{(i)n} = \frac{1}{2} W(q^{(i)n}) \sum_{j=1}^{n} \vec{\omega}_s^{(i)j}, \tag{2.73}$$

where

$$\begin{aligned} n &= 1, 2, ..., N_{\mathrm{H}} + N_{\mathrm{S}}, \\ i &= 1, \cdots, N_{\mathrm{F}}, \end{aligned} \tag{2.74}$$

$$W(q) = \begin{bmatrix} -q_1 & -q_2 & -q_3 \\ q_0 & q_3 & -q_2 \\ -q_3 & q_0 & q_1 \\ q_2 & -q_1 & q_0 \end{bmatrix}, \tag{2.75}$$

and $\vec{U}^{(B)}$, $\vec{\Omega}^{(B)}$, and $\vec{\omega}_s^{(i)n}$ have already been determined by solving the system of linear equations.

Combining a boundary element method with a Kirchhoff rod model to simulate the dynamics of a flexible filament in viscous fluid leads to a stiff set of ODEs that is computationally expensive to solve using general implicit schemes. Instead, we use an explicit multirate time integration scheme, as suggested by Bouzarth et al. [14] (without implementing their proposed spectral deferred corrections). In this approach, we update the nodal force densities and the angular and translational velocities of the cell body on coarse time steps while nodal force and torque densities on the flagella and angular velocities of the flagellar segments are updated on finer time steps (50-100 fine time steps per coarse time step), as shown in Fig. 2.10.

This splitting procedure significantly decreases the computational cost because the non-stiff cell body portion is solved less frequently. By comparing the multirate method with simply using a single (fine) time step size in a test simulation, we found a 55% reduction in computational time and only a 0.85% relative difference in the computed net displacement. In fact, we divided the difference in the displacement by the net displacement).

Since we are faced with a stiff set of ODEs, computational speed is crucial in the implementation of the numerical scheme. For this reason, we compared the computational speeds between Python, Fortran, and Matlab and decided to choose Matlab to implement

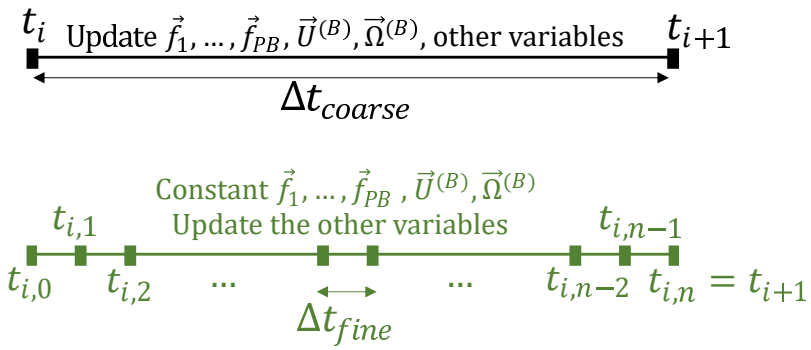

Figure 2.10: Each coarse time step $[t_i, t_{i+1}]$ is split into n fine time steps $[t_{i,m}, t_{i,m} + \Delta t_{fine}]$, $m = 0, \ldots, n-1$.

the model. Matlab provides not only a competitive computational speed (in comparison with Fortran) but also many built-in functions which ease the development of the code. We used Matlab R2019b-2022b to implement the model and conduct the simulations. The developed code is serial, and thus CPUs with higher clock speeds 2.8-3.7GHz are mainly used to conduct the simulations. Among the several types of CPUs employed in this project, "Intel(r) Xeon (r) gold 6244 @ 3.60GHz" and "Intel(r) core (tm) i9-10900 @3.7GHz" are on the top of the usage list. The minimum RAM required to conduct the simulations in the unbounded and near-wall spaces is 1.5GB. Depending on the complexity of the geometry, the swimming space (bounded/unbounded), the stiffness of the flagella, and the duration of the simulation, the actual simulation time varies from a few days to three months.

After proposing the current numerical scheme, we can highlight the main differences between our scheme and the popular schemes used in the literature to simulate bacterial locomotion. Unlike the previous schemes in which the penalty method is mainly used to enforce the rigidity of the cell body [87, 88, 85], we already assume that the cell body is rigid and boundary integral equations are solved over the cell body surface. In the penalty method, a network of stiff springs is employed to enforce the rigidity, therefore very small time steps are required to solve the resultant ODEs. Furthermore, the regularized stokeslet is used in those schemes to model the hydrodynamic interactions between the cell body and the surrounding fluid and it adds regularization error ($O(\epsilon)$ or $O(\epsilon^2)$) to the obtained results, whereas we solve the singular form of the boundary integral equations over the cell body without the regularization error.

In our numerical scheme, the flagellum complex is composed of a chain of some rigid segments, therefore inextensibility of the flagella is already satisfied. However, very large

stretching and shear moduli are assigned to the flagella in the previous schemes to ensure that the flagella remain inextensible and unshearable [86, 82]. These moduli lead to smaller time steps and increase the computational cost.

As already stated in section 2.4.6, $\vec{N}^{(i)\frac{1}{2}}$ which denotes the internal moment transmitted from the rotor to the first segment of the hook is computed using a sub-iterative method. At the beginning of the simulations, since the first segment of the hook is aligned with the rotor, we can take $\vec{N}^{(i)\frac{1}{2}} = T_i \vec{e}_1^{(i)}$. However in the next time steps, this identity is not valid anymore, and $\vec{N}^{(i)\frac{1}{2}}$ should be computed in a way such that the motor torque constraint and Kirchhoff rod model are satisfied at the rotor-hook joint, simultaneously. In our model, the orientation of the rotor is determined by the axial direction $\vec{e}_1^{(i)}$, $i = 1, \cdots, N_{\mathrm{F}}$, which are fixed relative to the cell body frame. At the joint connecting the hook to the rotor, the projection of the internal moment onto $\vec{e}_1^{(i)}$ is equal to the motor torque, i.e.,

$$\vec{N}^{(i)\frac{1}{2}} \cdot \vec{e}_1^{(i)} = T_i, \quad i = 1, \cdots, N_{\mathrm{F}}. \tag{2.76}$$

In this equation, $\vec{e}_1^{(i)}$ and T_i are known, and $\vec{N}^{(i)\frac{1}{2}}$ is determined by employing a sub-iterative method explained below.

To simplify notation in this section, we explain our model for a single flagellum and drop indices for distinguishing between the flagella. We define the orientation vectors of the flagellum $\{\vec{e}_1, \vec{e}_2, \vec{e}_3\}$, to be those of the rotor. The rotor axis is $\vec{e}_1$, and is fixed in the cell body frame. The transverse direction vectors $\vec{e}_2$ and $\vec{e}_3$ rotate about the rotor axis with a variable rotational speed W^{rot} that we calculate iteratively at each time step to be consistent with the prescribed motor torque.

In our model, the rotor, denoted by superscript 0, is embedded inside the cell body and its length is supposed to be equal to the hook's segments. For the Kirchhoff rod description, we adopt the common convention that the third director, $\vec{D}_3$, is the tangential direction along the curve. Thus, we define the relationships for the rotor segment

$$\vec{D}_3^0 = \vec{e}_1, \quad \vec{D}_1^0 = \vec{e}_2, \quad \vec{D}_2^0 = \vec{e}_3. \tag{2.77}$$

At any given time, we assume that all positions and orientations of the segments are known. The angular velocities $\vec{\omega}_s^n$, $n = 1, 2, .., N_{\mathrm{fl}}$, are determined by solving the system of linear equations described in the main text. The orientations of segments $n = 1, 2, ..., N_{\mathrm{fl}}$ are determined at the next time step using an explicit time integration rule. The orientation of the rotor, however, is not updated in this manner because explicit time-stepping would generally not satisfy the motor torque constraint Eq. 2.76, where the torque transmitted from the rotor to the hook $\vec{N}^{\frac{1}{2}}$ depends on the directors at the zeroth and first segments

of the rod according to the Kirchhoff rod model [Eqs. 2.56-2.57 with $n = 0$]. Note that this motor torque condition prescribes only the component of torque in the axial direction. The other two components of torque are due to bending.

In our methodology, we use an iterative method to adjust $\vec{e}_2$ and $\vec{e}_3$ at each time step so that Eq. 2.76 is satisfied. We start with an initial trial value of the rotor angular velocity W^{rot} equal to its value at the previous time step. We next update $\vec{e}_2$ and $\vec{e}_3$ based on their values at the previous time step and the estimate for W^{rot}. Then, the projection of $\vec{N}^{\frac{1}{2}}$ onto $\vec{e}_1$ is compared with the target value of T. According to the obtained error, W^{rot} is adjusted and the iteration continues so that a desirable error for the motor torque constraint is achieved. The steps of this iterative method are presented schematically in Fig. 2.11.

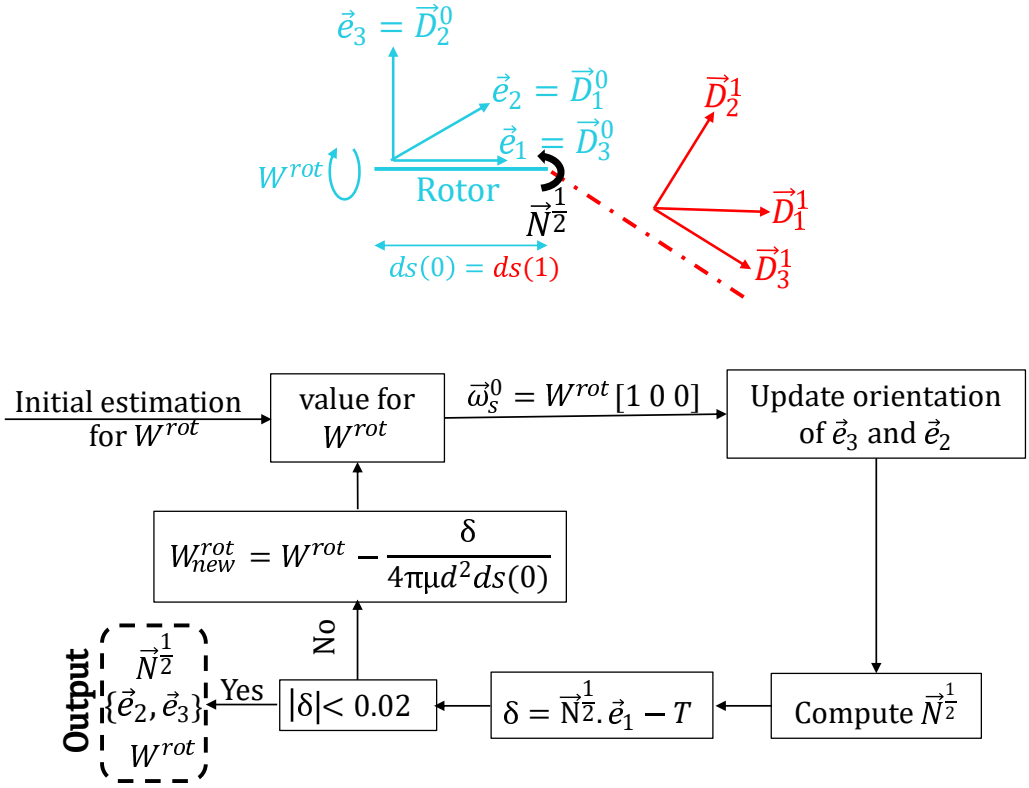

Figure 2.11: Flowchart of the iterative method to find the rotor orientation, the motor speed, and the internal moment at the joint connects the hook to the rotor. The rotor and the corresponding triad are marked by blue color. The first segment on the hook is also represented by the red dashed line.

2.8 Verification

We begin with a comparison of numerical results from our method with those obtained by Higdon et al. [46] to verify our boundary element method. In this test, we calculate the swimming speed of a model bacterium with a single rigid flagellum and a spherical cell body. The flagellum is divided into 30 and 60 segments for the shorter ($l/R = 5$) and longer ($l/R = 10$) flagellum, respectively, and we choose the other parameters according to Higdon's model. As shown in Fig. 2.12, the swimming speeds of the model bacterium for two different flagellum lengths are in good agreement with the published results.

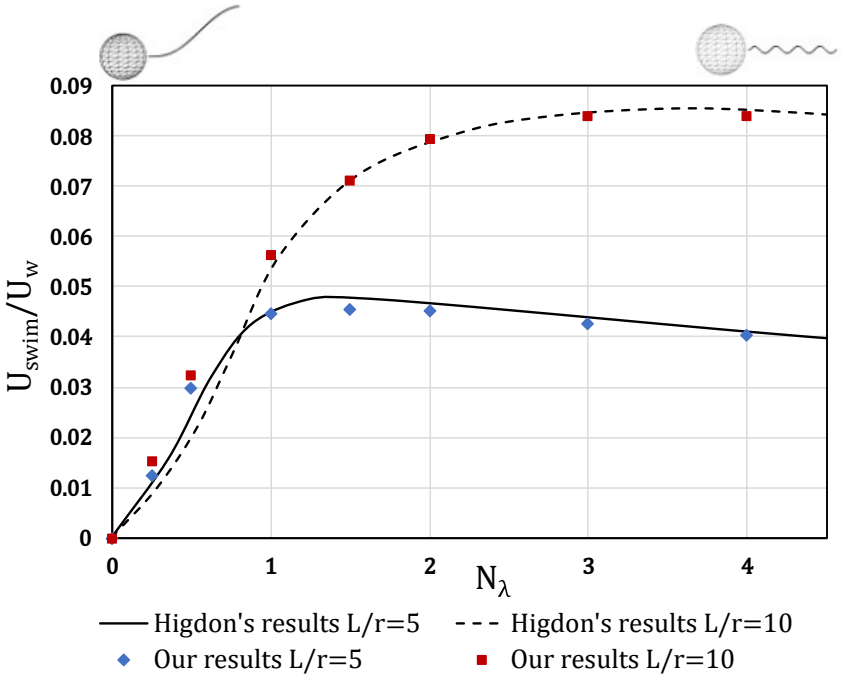

Figure 2.12: Comparison of the obtained results for swimming speed of a uni-flagellated bacterium with Higdon's. U_{swim}/U_w is the progressive speed non-dimensionalized by the linear wavespeed of the flagellum. R and l are the cell body radius and the flagellum length, respectively. N_λ represents the flagellum wavenumber.

To verify the elastic model, the equilibrium shape of a flexible filament settles in a viscous fluid is compared with an analytical solution derived by Xu et al. [128] for the case of small deformation amplitudes. In particular, if it is assumed that a flexible filament with

dimensionless length 2 and a large bending modulus (3 in our test) settles horizontally under a uniform force, by applying the force correction factor (according to the source reference) the maximum dimensionless deflection becomes about 0.07 and so the given solution is valid. If the filament is discretized into $n = 30$ segments, the relative l^2-norm of the deviation of the numerical displacements y^{num} from the analytical solution y^{an} evaluated at corresponding discrete points is $E_{l^2} = \sqrt{\sum_{j=1}^{n} |y_j^{\text{an}} - y_j^{\text{num}}|^2 / \sum_{j=1}^{n} |y_j^{\text{an}}|^2} \approx 0.022$. Since the deflection of the filament is small, the drag coefficient of the flexible filament should be comparable with a rigid straight rod in a viscous fluid ($C_N = 4\pi\mu l/(\ln(2l/d) + 0.5)$ [27]). The minimum difference between the drag coefficients achieved in higher stiffnesses is about 3.8%. Such a difference is reasonable because our filament has a finite length and a relatively large thickness, whereas the mentioned formula is accurate only for very long and thin filaments. In the last step of the numerical verification, it is verified that the swimming speed of a uni-flagellated bacterium with a flexible flagellum converges to the rigid model as the stiffness of the flagellum increases. In particular, if we consider Higdon's model bacterium with $N_\lambda = 1$ and $l/R = 5$, the swimming speeds of the model bacterium with flagellum stiffnesses $k_f = 3$, $k_f = 10$ and $k_f = 15$ are respectively 93.6%, 97.4% and 98.7% of the rigid model speed. It is worth mentioning that the swimming speeds of this model bacterium with a flexible flagellum are always lower than that with a rigid flagellum. Please see Appendix. B, for the convergence test of the numerical methods.

Chapter 3

Locmotion of Uniflagellated Bacteria

3.1 Introduction

The hydrodynamic interactions between the bacteria living in aqueous media and surrounding surfaces could significantly impact bacterial locomotion. Depending on the species, the bacteria are sometimes trapped close to the surfaces [126, 110, 87]. Entrapment of swimming bacteria near surfaces may lead to some biological processes such as biofilm formation which is a major problem in many industries and biomedical sectors [22, 100]. Finding practical solutions against biofilm formation needs a deep understanding of the preformation stages including the hydrodynamic interactions between the bacteria and the desired surfaces. We use our elastohydrodynamic model in this chapter to simulate the locomotion of a uniflagellated bacterium with a flexible hook and flagellum in free and near-surface spaces.

The vital role of hook in the locomotion of uniflagellated bacteria is experimentally and numerically proven [115, 86, 107]. For this reason, it is expected that the hook's stiffness, at the rest configuration, and types of filament and cell body connection considerably affect bacterial behavior. These effects and their importance on bacterial locomotion are further investigated in the first part of this chapter. We use the physical properties of *V. alginolyticus* to construct the model bacterium. Furthermore, we apply a dynamic torque to the flagellum according to the torque-speed relationship obtained experimentally for *V. alginolyticus*, unlike the other studies in which it is assumed that the motor applies either constant torque or constant speed to the flagellum. In this regard, investigations from Sowa et al. [116] demonstrate that the torque generated by the *V. alginolyticus*'s motor increases with NaCl concentration in the swimming medium. Moreover, the higher rotation

rate of the motor is achieved at lower loads. The reported torque-speed relationships for three levels of NaCl concentrations (50, 10, and 3 mM), are used in this chapter to rotate the flagellum [116]. This feature in our model distinguishes the obtained results in this section from the other studies already conducted to explore the locomotion of the uniflagellated bacteria.

Entrapment of three different strains of *V. alginolyticus* near surfaces is experimentally studied by Wu et al. [126]. They found that *V. alginolyticus* can be entrapped near a surface in both puller and pusher modes. However, the entrapment behavior strongly depends on the cells' swimming speeds which are controlled by sodium concentration in the aqueous medium. Investigating the behavior of *V. alginolyticus* near a surface, in either puller or pusher modes and in different levels of NaCl concentrations is another aim of this chapter. The importance of the hook and flagellum flexibility and the cell body aspect ratio in near-surface entrapment of the uniflagellated bacteria is investigated in the rest of the chapter.

3.2 Geometric model and mechanical properties

Following the dimensions and properties reported for *V. alginolyticus* by Son et al. [115], the uniflagellated model bacterium consists of a spherocylindrical cell body, flexible helical filament, and a very flexible straight hook which connects the filament to a pole of the cell body. As shown in Fig. 3.1, the cell body is a cylinder with two hemisphere caps, and we call it spherocylinder. A small gap is defined between the cell body and the hook to avoid singularities in the numerical scheme. The position and configuration of the model bacterium are described by three reference frames including $\left\{\vec{e}_1^{(1)}, \vec{e}_2^{(1)}, \vec{e}_3^{(1)}\right\}$ as motor-fixed, $\left\{\vec{e}_1^{(\mathrm{B})}, \vec{e}_2^{(\mathrm{B})}, \vec{e}_3^{(\mathrm{B})}\right\}$ as body-fixed and $\left\{\vec{X}, \vec{Y}, \vec{Z}\right\}$ as global frames. In this model bacterium, it is assumed that the initial and rest configurations of the hook and flagellum are straight and right-handed helix, respectively. In the global frame, the flagellum center line is given by

$$\vec{\Lambda}(\xi) = \vec{X}^{(1)} + (0.02l + \xi)\vec{e}_1^{(1)} + a\cos(\lambda\xi)\vec{e}_2^{(1)} + a\sin(\lambda\xi)\vec{e}_3^{(1)}, \tag{3.1}$$

where $\vec{X}^{(1)}$ denotes the position of the flagellum on the cell body and $\lambda = 2\pi/p$ is the wavenumber. The variable ξ parameterizes the distance along the axis of the helix with $0 \leqslant \xi \leqslant L_F$. In addition, a and p represent the helix amplitude and pitch, respectively. All lengths in the model bacterium are non-dimensionalized by the average cell body radius $\overline{R} = 0.81\mu\mathrm{m}$. In particular, this value is the radius of an equivalent sphere with the same volume as the cell body. Physical properties of the model bacterium are given in Table 3.1.

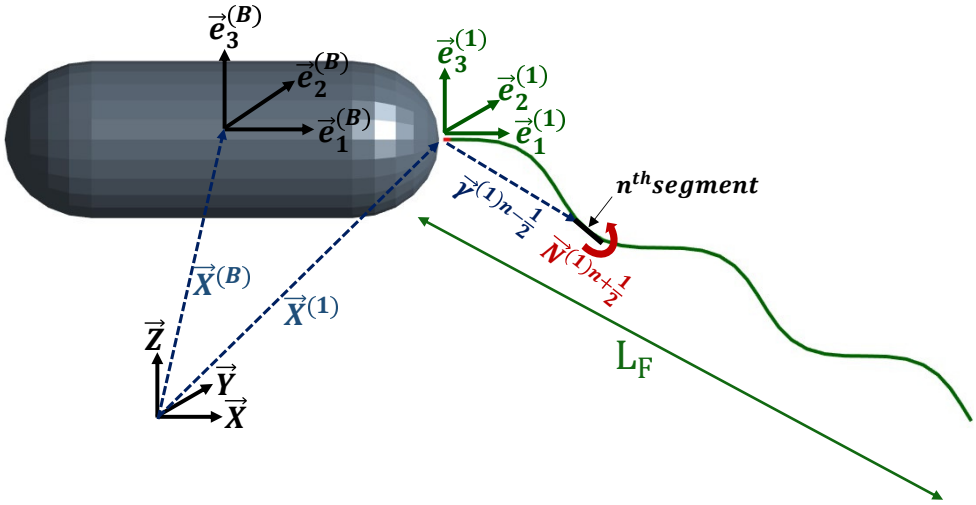

Figure 3.1: A schematic view of the uniflagellated model bacterium.

In this study, motor torques, flagellum, and hook stiffnesses are non-dimensionalized with the maximum motor torque $T_{\max} = 3.8\,\mathrm{pN\,\mu m}$ [116] in *V. alginolyticus*. We define the relative stiffnesses of the flagellum and hook $k_\varrho(\varrho = F, H)$ as:

$$k_\varrho = \frac{(EI)_\varrho}{T_{\max}\overline{R}}, \tag{3.2}$$

where E is Young's modulus of the material, I denotes the moment of inertia of the cross sections of the flagellum and hook, and $\overline{R}$ is the average cell body radius.

As already stated, the flagellar motor torque is adjusted according to the rotation frequency of the flagellum. In this regard, torque-speed relationships of *V. alginolyticus* at three different concentrations of NaCl are non-dimensionalized and employed here to apply a proper torque at a given medium concentration and motor rotation frequency. If we split the torque-speed plot into two parts, high torque-low speed, and low torque-high speed, and suppose that the relationship is linear in each part, a piece-wise function can be constructed to relate the motor torque to its rotation frequency. The two linear pieces intersect at the crossover point and the motor torque at a given frequency is the minimum of the two linear functions at that frequency. Specifically, for three levels of NaCl

Table 3.1: Physical properties of the model bacterium

Description	**Symbol**	**Dimensionless value**	**Dimensional value**
Cell body short radii	R_2, R_3	0.675	0.546 µm
Cell body long radius	R_1	$2.5R_2$	1.366 µm
Flagellum/Hook diameter	d	0.12	0.097 µm
Flagellum total length	l	5.53	4.479 µm
Flagellum rest/initial pitch	p	1.83	1.482 µm
Flagellum rest/initial amplitude	a	0.172	0.138 µm
Hook length	l_H	$0.02l$	0.089 µm
Flagellum relative stiffness	k_F	3.23	-
(Flexural rigidity)	$(EI)_F$	-	$(9.94\,\mathrm{pN\,\mu m^2})$
Loaded hook relative stiffness	k_H	0.125	-
(Flexural rigidity)	$(EI)_H$	-	$(0.38\,\mathrm{pN\,\mu m^2})$
Repulsion strength of Lennard-Jones potential	F_s	0.1	0.469 pN
Cut-off distance of Lennard-Jones potential	$2^{1/6}\sigma$	0.2	0.162 µm
Number of segments on filament	N_S	23	-
Number of segments on hook	N_H	2	-
Number of triangular elements on the cell body	N_B	112	-
Regularization parameter	ϵ_F	$0.5d$	0.049 µm
Fluid viscosity	μ	1	$0.001\,\mathrm{N\,s\,m^{-2}}$
Fine time step	Δt_fine	3.5×10^{-4}	4.98×10^{-8} s
Coarse time step	Δt_coarse	3.5×10^{-2}	4.98×10^{-6} s

concentration, we model the torque-frequency relationships as

$$\begin{aligned} T_H(\nu) &= \min\{-1.203\nu + 1, -25.197\nu + 2.543\}, \\ T_M(\nu) &= \min\{-1.691\nu + 0.789, -24.572\nu + 1.562\}, \\ T_L(\nu) &= \min\{-1.071\nu + 0.551, -33.079\nu + 1.164\}, \end{aligned} \tag{3.3}$$

where ν represents the dimensionless motor frequency, and T_H, T_M, and T_L denote the dimensionless motor torques at 50, 10, and 3 mM concentrations of NaCl, respectively. In both puller and pusher modes, the motor torque follows the same curves with a sign change.

3.3 Unbounded fluid

In this section, we investigate the locomotion of the model bacterium in free space. First, we compare the swimming speed of the model bacterium in both puller and pusher modes. Then, we explore the impacts of the hook's shapes and types of hook-flagellum connection on the swimming properties of the model bacterium.

3.3.1 Swimming speed

Before comparing the swimming speeds, it is necessary that a clear definition is given for the swimming speed of the uniflagellated model bacteria. In general, for steady swimming, the instantaneous velocity vector is not constant but precesses about an axis of average motion as the flagellum and cell body rotate. This causes the bacteria to move on helical trajectories. Following Higdon's formulation [45], we define the (average) swimming speed of the uniflagellated bacteria as:

$$U_{\text{swim}} = \frac{(\vec{\Omega}^{(B)} - \vec{\omega}_s^0) \cdot \vec{U}^{(B)}}{||\vec{\Omega}^{(B)} - \vec{\omega}_s^0||}. \tag{3.4}$$

This formula is accurate as long as the solution such as the instantaneous translational and angular velocities are time-independent on the motor-fixed frame $\left\{\vec{e}_1^{(1)}, \vec{e}_2^{(1)}, \vec{e}_3^{(1)}\right\}$. In our model bacterium, $\vec{e}_1^{(\mathrm{B})}$ is the axisymmetric axis of the cell body, and the flagellar motor is only allowed to spin in $\pm\vec{e}_1^{(\mathrm{B})}$ directions. Consequently, the flagellum rotates about the axis of the cell body after it reaches a steady shape and the assumptions are satisfied. The quantities in the formula are evaluated at any instant but the result is time-independent. As shown in Fig. 3.2A, the swimming speeds in both modes (puller/pusher) and various flagellum stiffnesses increase almost linearly with the motor torque. We increase the motor torque so that the rotation of the flagellum is stable. For this reason, the maximum torque in the more flexible flagellum is roughly up to their torque threshold. It is worth stating that when the motor torque surpasses the threshold, the pusher flagellum exhibits overwhirling rotation (will be discussed in section 4.4) and the puller flagellum bends toward the cell body and tends to wrap around it. Interestingly, these results demonstrate that the stiffness of the flagellum does not significantly affect the swimming speed of the model bacterium as long as the motor generates a constant torque and the rotation of the flagellum is stable. Conversely, in a constant motor speed, the results show that the swimming speed of the model bacterium decreases with the flagellum flexibility (i.e. lower

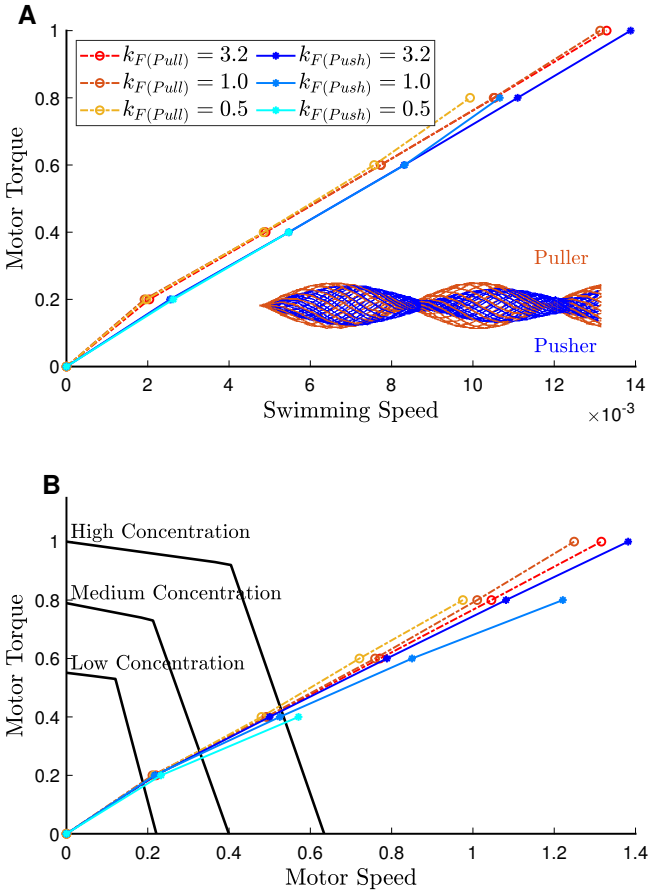

Figure 3.2: A) The relationship between the swimming speed of the model bacterium and the motor torque in three flagellum stiffnesses and two swimming modes (puller/pusher). A constant motor torque is applied, ranging from 0 to 1 in dimensionless units, and the steady swimming speeds in the puller and pusher modes are obtained. Comparing the steady shapes of the pusher and puller flagella indicates that the amplitude of the pusher flagellum is smaller than the puller one. B) By varying the motor torque from 0 to 1, the rotation speeds of the flagellar motor are obtained in the different stiffnesses of the flagellum and the swimming modes. There is almost a linear relationship between the motor torque and motor speed. When it is allowed that the motor torque dynamically changes according to the black torque-speed curve (which is a characteristic of the motor performance), the intersection of the colored and the black curves is the steady point where the motor torque and speed converge to.

stiffness k_F, lower speed). See Fig. B.1, for example. Comparing the rotation frequency of the flagellum in puller and pusher modes reveals that the flagellum slightly rotates faster in the pusher mode (Fig. 3.2B). Closer inspection of the flagellum shape indicates that the flagellar helix amplitude slightly increases from its rest amplitude in the puller mode; and, conversely, it slightly decreases in the pusher mode. Therefore, the pusher flagellum can rotate faster at a constant torque because of lower hydrodynamic resistance. The steady shapes of the rotating pusher and puller flagella are displayed in Fig. 3.2A. Unlike the swimming speed, the rotation frequency of the puller and pusher flagella are affected by the stiffness, such that the most flexible flagellum gets the maximum rotation speed in the pusher mode. In a wider perspective, it is expected that a more flexible flagellum in pusher mode produces lower propulsion at a constant rotation speed, but at constant torque, the propulsion in the more flexible flagellum is comparable with the stiffer one because the more flexible flagellum rotates faster. In puller mode, these correlations exist but in opposite directions, such that higher flexibility results in lower rotation frequency.

The slope of the curve in Fig. 3.2B indicates the effective rotational drag coefficient of the flagellum and is dependent on the flagellum stiffness. In contrast, the slope of the curve in Fig. 3.2A is found to be relatively insensitive to the flagellum stiffness. This is an interesting observation because even though the flagellum deforms at higher torques and the rotational drag coefficient changes, the swimming speed maintains a linear relationship with the torque.

In Fig. 3.2B, the intersection of the colored lines and the torque-speed relationships at different concentrations of NaCl (Eq. 3.3) represents the steady motor's torque and speed at the given flagellum stiffness and the ions concentration.

3.3.2 Hook shape

The hook, which acts as a universal joint to transmit the torque from the rotor to the flagellar filament, could be intrinsically straight or helical [115, 103]. Motivated by this difference, we numerically study the effects of the hook shape on the stable motor torque (when it dynamically changes with the rotation speed) and the swimming speed in an unbounded fluid with a medium concentration of NaCl.

The actual molecular structure of the filament is uniform so a pure helical shape is expected when the filament is stationary. However, in the rigid flagellum models, the helical filament is described with an amplitude envelope growth rate k_E to align the flagellum's axis with the cell body's axis. In this description, the pure helix equation (i.e. Eq. 3.1) is

revised to:

$$\vec{\Lambda}(\xi) = \vec{X}^{(1)} + (0.02l + \xi)\vec{e}_1^{(1)} + \Xi(\xi)\cos(\lambda\xi)\vec{e}_2^{(1)} + \Xi(\xi)\sin(\lambda\xi)\vec{e}_3^{(1)}, \tag{3.5}$$

where $\Xi(\xi) = a(1-e^{-(k_E\xi)^2})$ is the helix amplitude function and k_E represents the amplitude growth rate (the amplitude grows from zero to a over a region of length roughly $\frac{2}{k_E}$). Such a simplification is widely used in the literature but its effect on the swimming properties has not been quantitatively compared with the pure helical filament.

To do these comparisons, three model bacteria with different filament and hook configurations are taken into account. In the first configuration, the hook is straight and the shape of the filament at rest is pure helical as described by Eq. 3.1. In the second model bacterium, we assume that the hook is straight and the filament's shape at rest is described using a growing helical amplitude as in Eq. 3.5. In the third one, the hook's shape at rest is helical with the same helix shape as the filament and the filament is pure helical, as shown in Fig. 3.3.

The obtained results indicate that in the second configuration (i.e. employing k_E), the model bacterium in both puller and pusher modes reaches steady-state monotonically and very quickly and its stable motor torque is smallest among the studied cases. In contrast, in the first (straight hook and pure helical filament) and third (helical hook and filament) configurations, the swimming speed and motor torque converge with damped oscillations to steady states, as displayed in Fig 3.3. These oscillations are due to the misalignment of the filament axis and the swimming orientation at the beginning of the swimming. After a few rotations of the flagellum, those axes are aligned and the swimming properties become steadily smooth.

Even though the rotation rate of the pusher flagellum in the second configuration is the largest, its swimming speed is the smallest, and that is because the average amplitude of the filament in this configuration is smaller than in the others. Interestingly, the model bacterium with a helical hook has the highest swimming speed whereas it has the lowest motor speed. The variation of the motor speed with time is not specifically sketched here but by using the obtained results for the motor toque and according to the torque-speed curve at the medium concentration of NaCl the motor speed is achievable. The swimming speeds in the puller mode are almost identical, but the steady motor torque is the smallest in the second configuration. This is an interesting observation because this bacterium swims as fast as the other model bacteria by applying a smaller torque in the puller mode.

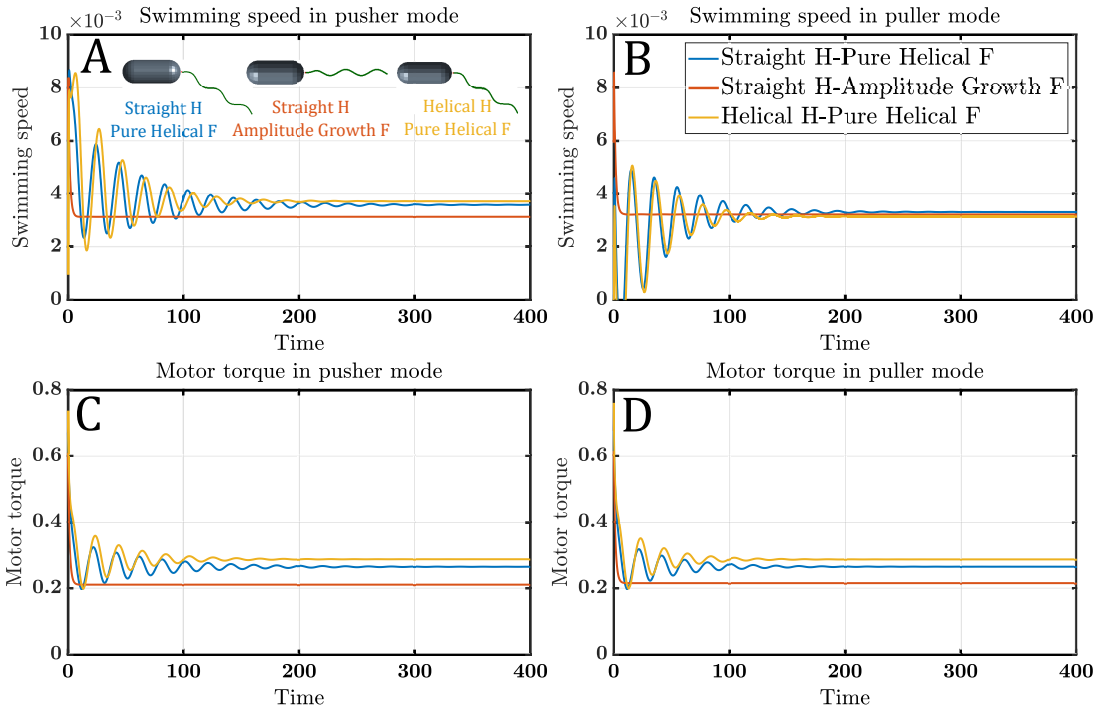

Figure 3.3: The steady-state swimming speed and motor torque of the model bacterium in an unbounded fluid. These results are obtained for different shapes of hook and filament at the rest configurations. The rest (stationary in the absence of motor torques) configurations of the three models are depicted in A. The physical properties of the model bacteria in these simulations are stated in Tab. 3.1. The reported values for the swimming speeds are not accurate during the transition period because of the limitations that exist in using Eq. 3.4 for the transition period. The transition periods are shown here to compare the convergence times.

3.4 Near a surface

The current section mainly focuses on the behavior of *V. alginolyticus* in a half space to discover more details about its tendency to swim next to a surface or escape from a planar wall in puller and pusher modes. To achieve this aim, the influences of the swimming modes, NaCl concentration, flagellar filament/hook stiffness, initial state, and the cell body aspect ratio on *V. alginolyticus*'s tendency to remain near a surface are investigated. In the following simulations, the cell body in the model bacterium is spherocylindrical and a pure

helical and flexible filament is connected to one pole of the body through a straight and very flexible hook. The rotor axis is always perpendicular to the cell membrane (i.e. aligned with $\vec{e}_1^{(B)}$) and the initial configuration is matched to the rest configuration according to Fig. 3.1.

3.4.1 Concentration of sodium chloride

V. alginolyticus utilizes a Na^+-driven type flagellar motor to rotate the flagellum complex in the CW and CCW directions. The concentration of sodium chloride in the swimming medium limits the maximum torque (stall torque) generated by the motor. For this reason, the torque-speed relationship varies with the sodium chloride concentration, as expressed in Eq. 3.3 and plotted in Fig. 3.2B.

The swimming trajectories in Fig. 3.4 demonstrate that the model bacterium in the pusher mode tends to escape from the surface in the different concentrations of NaCl. Moreover, these results illustrate that the escaping angle is significantly smaller in the lower concentrations and the bacterium has a strong tendency to swim close and almost parallel to the surface. These results are consistent with the experimental observation of *V. alginolyticus* in which a high concentration of cells is observed next to the surface when a dilute solution of ions is used in the swimming medium [126]. Closer inspections reveal that this difference in the escaping angles is related to the magnitude of the hydrodynamic drag forces on the cell body. Typically, when a bacterium with a flagellum at the rear swims near a surface, the cell body slightly points upward (away from the surface) to balance the hydrodynamic torques on the body. In the high concentration of NaCl, the propulsive force generated by the flagellum and the hydrodynamic drag force on the cell body are large. Thus, the large bending moment induced by these forces causes the hook to bend more, and so the long axis of the cell body finds a larger angle with respect to the surface. This variation in the cell body orientation increases the drag force on the cell body and facilitates escaping from the surface. Specifically, the maximum angles between the cell body's long axis and the surface in the studied concentrations are 14.05°, 8.79° and 7.01°, respectively, in decreasing order of NaCl concentrations.

As displayed in Fig. 3.5, the model bacterium in the puller mode is attracted to the surface, regardless of the ions concentration. Our numerical results show that the model bacterium moves on smaller orbits in higher concentrations of NaCl. Furthermore, the cell body's long axis becomes more parallel to the surface in higher concentrations because of large hydrodynamic drags on the cell body at higher swimming speeds. Even though the negative dipolar hydrodynamic field and also the viscous torque due to no-slip boundary

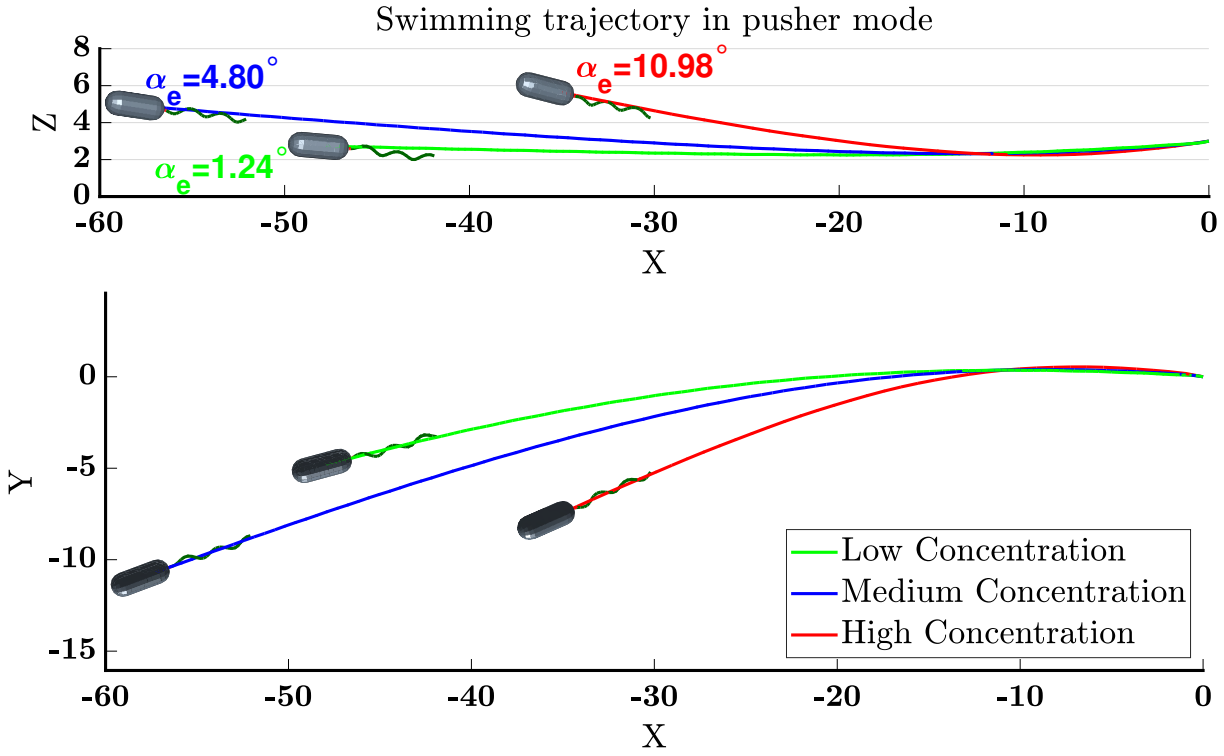

Figure 3.4: Swimming trajectory of the model bacterium near a flat surface in pusher mode. In higher concentrations of NaCl, the bacterium immediately escapes from the surface with a relatively large angle ($\alpha_e = 10.98°$). The escaping angle α_e represents the angle between the swimming trajectory during the escaping state and the surface. The initial distance and angle with respect to the surface are respectively 3 and 15°. Simulation times are $T_s = 23000$, $T_s = 17000$, and $T_s = 7000$ for the low, medium, and high concentrations, respectively.

drag tend to change the orientation of the long axis of the cell body such that $\vec{e}_1^{(B)}$ points toward the surface, the hydrodynamic drag overcomes these effects and enforces the cell body to be more parallel to the surface in higher concentrations. In our model bacterium, the mean angle between the cell body's long axis and the surface in High, Medium, and Low concentrations of NaCl are 2.66°, 3.32° and 4.11°, respectively. It is worth mentioning that in the puller mode, the steric repulsive force between the wall and the swimmer avoids the cell body and the flagellum colliding with the surface. According to these explanations, the stable orientation of the cell body might be different in other cell body shapes or sizes.

Fig. 3.6 represents the variation of the motor torque as the model bacterium swims

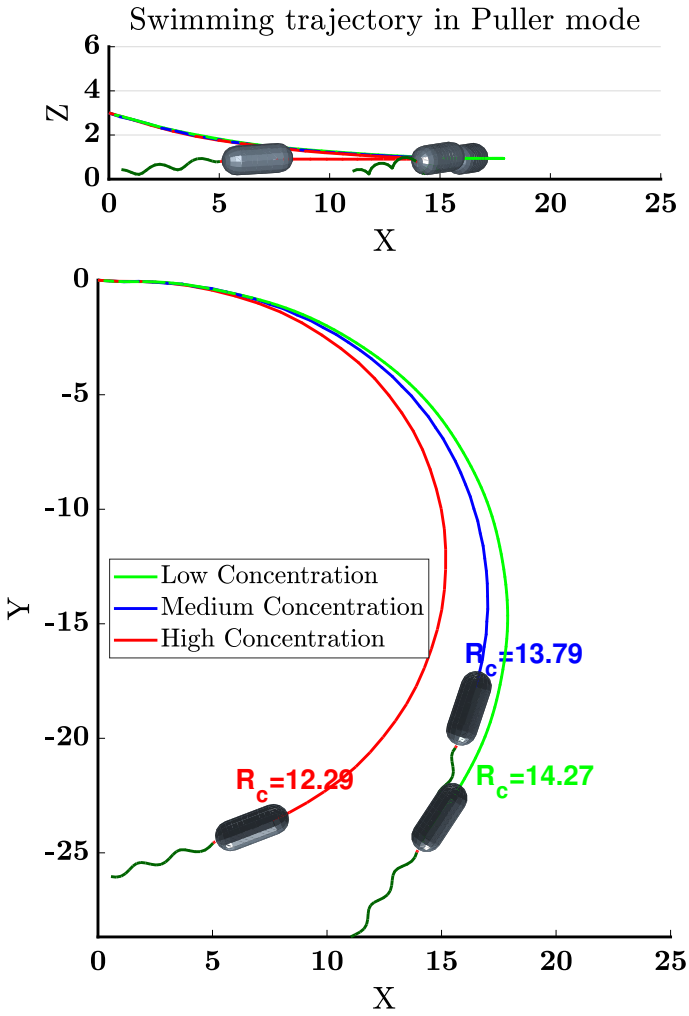

Figure 3.5: Near surface swimming trajectory of the model bacterium in the puller mode. In different concentrations of NaCl, the model bacterium is entrapped by the surface. The NaCl concentration in the swimming medium changes the radius of the circular trajectories (R_c). The initial conditions are the same as the pusher mode. Simulation times are $T_s = 17000$, $T_s = 15000$, and $T_s = 6800$ for the low, medium, and high concentrations, respectively.

next to a surface. After a very short transition period, the mean value of the motor torque does not change significantly as the model bacterium swims toward or escapes from the surface. However, when the flagellum is so close to the surface, the motor torque fluctuates between a minimum and maximum value at each rotation of the flagellum due to the variation of the no-slip boundary drag on the flagellum. The steric repulsive force between the flagellum and the wall is also responsible for those fluctuations in the puller mode. Closer inspection indicates that in all cases the mean motor torque is higher in the puller mode. The different stable shape of the helical filament in the puller and pusher modes explains those differences in the stable motor torque.

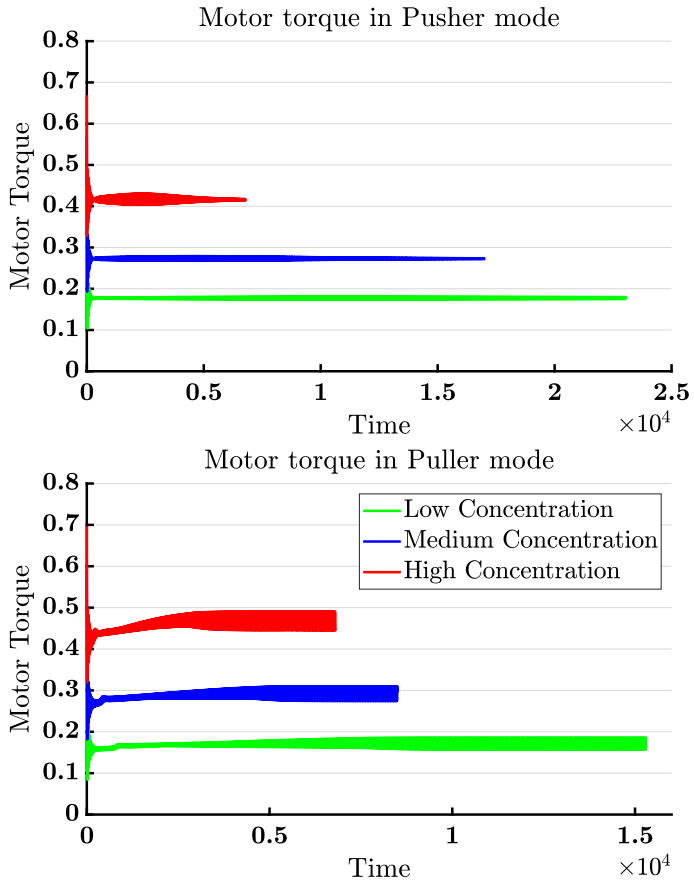

Figure 3.6: Variation of the motor load as the bacterium swims toward the surface and then is entrapped/pushed back by the surface.

Table 3.2: Escaping angles of the pusher-mode bacterium in different initial conditions and NaCl concentrations

Concentration	$H_0 = 3$ $\alpha_0 = 45°$	$H_0 = 3$ $\alpha_0 = 15°$	$H_0 = 1.5$ $\alpha_0 = 15°$	$H_0 = 1.1$ $\alpha_0 = 15°$
Low	1.65°	1.24°	1.55°	1.74°
Medium	6.19°	4.80°	5.76°	6.17°
High	28.12°	10.98°	18.04°	42.81°

3.4.2 Initial condition

We showed that the escaping angle of the pusher-mode model bacterium varies with the concentration of sodium chloride. To ensure that this near-surface behavior is independent of the initial distance and orientation, we compare the swimming trajectories of the model bacterium when it is initially placed in different distances ($H_0 = 1.1, 3$) and angles ($\alpha_0 = 15°, 45°$) from the surface. As shown in Fig. 3.7, the model bacteria mainly remain near the surface in the lowest concentration of NaCl (green trajectories), and conversely, they exhibit a weak tendency to remain longer near the surface in the highest concentration of NaCl (see red trajectories). The escaping angles are quantitatively compared in Tab. 3.2. These results clearly illustrate that regardless of the initial condition, pusher-mode bacteria strongly tend to swim close to the surface in the lower concentrations of the ions. Such a correlation between the concentration and the tendency to mainly move next to the surface is consistent with the experimental observations of Wu et al. [126]. The obtained results in Tab. 3.2 also demonstrate a meaningful correlation between the escaping angle and the initial distance and attack angle. In this respect, the bacterium escapes from the surface with a larger angle as it is initially placed closer to the surface and/or approaches the surface with a larger attack angle. Comparing the obtained angles indicate that the dependency of the escaping angle to the initial condition is notable in the high concentration of NaCl, and it is fairly negligible in the medium and low concentrations.

3.4.3 Flagellum/Hook stiffness

The hydrodynamic interactions between the uniflagellated bacteria and a planar surface have already been studied well when a single rigid helix mimics the role of the flagellum [93, 58, 105]. This simplification is taken into account in many studies whereas the flexibility of the hook and the flagellum could impact the mean swimming speed, the orientation of

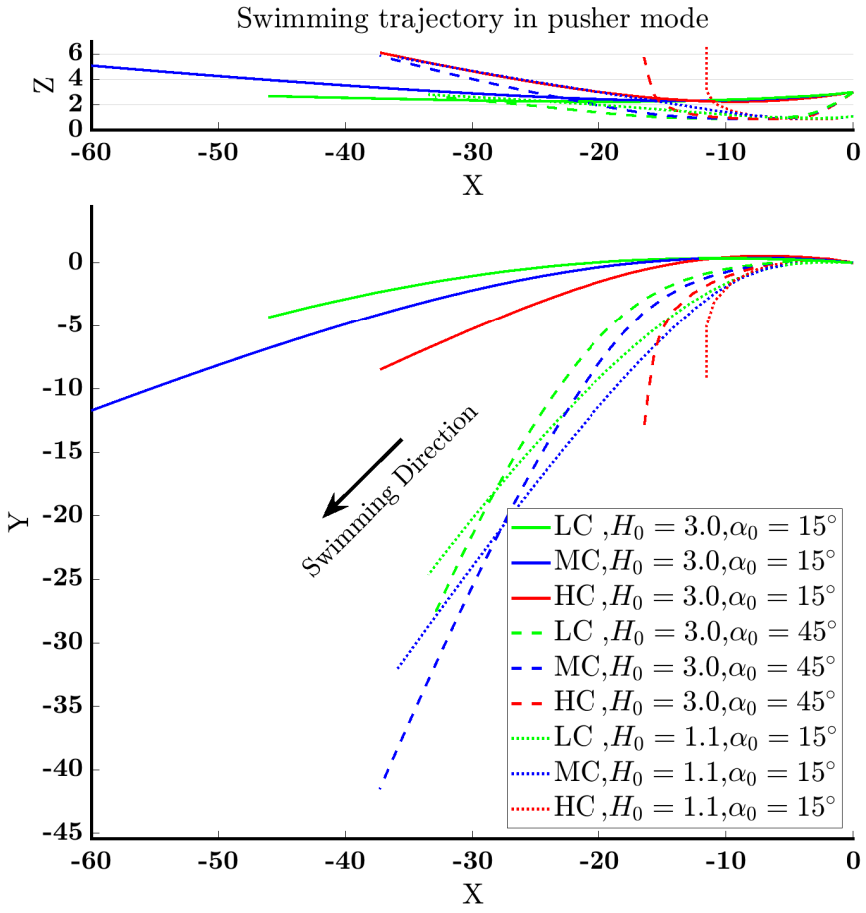

Figure 3.7: Swimming trajectories of the pusher-mode model bacterium in two different initial distances ($H_0 = 1.1, 3$) from the surface and two attack angles ($\alpha_0 = 15°$,$\alpha_0 = 45°$). LC, MC, and HC are respectively abbreviations of the low, medium, and high concentrations of NaCl.

the cell body, and the flagellum with respect to the surface. Therefore, it likely changes the boundary accumulating behavior of the bacteria close to the surfaces. To fill the research gap and better understand the behavior of different flagellated microorganisms near the surfaces, we study the locomotion of the model bacterium near the surface as different stiffnesses are assigned to the flagellum filament and the hook. As shown in Fig. 3.8, decreasing the rigidity of the filament and/or the hook helps the pusher-mode

model bacterium to escape from the surface more easily. When the cell body is pushed near the surface, the viscous torque tends to tilt up the cell body. Therefore, when the filament or hook is more flexible, they bend easily and do not resist changing the orientation of the cell body. Consequently, the angle between the cell body's long axis and the surface increases with time, and the bacterium escapes from the wall at a large angle.

Motivated by the obtained results which indicate that the escaping angle decreases by increasing the flagellum/hook rigidity, we compare the behavior of two model bacteria with the flexible and rigid flagellum. In both cases, we inevitably describe the flagellum helical shape with an amplitude envelope k_E to align the flagellum with the cell body axes. Interestingly, our simulations (Fig. 3.9) show that the model bacterium with rigid flagellum is entrapped by the surface whereas the bacterium with flexible flagellum escapes from the surface with a small escaping angle. The simulations are continued so that it is ensured that the average swimming speeds of the model bacterium in $\vec{Z}$ direction remain zero and positive in the rigid and flexible flagella, respectively. The obtained results in the last two simulations demonstrate that the flexibility of the flagellum in pusher-mode bacteria likely facilitates the escape from the surfaces.

Comparing the trajectories in the puller mode (Fig. 3.10) shows that the model bacterium moves on smaller circular orbits when it has a more flexible hook or flagellum. Furthermore, the radius of the orbits mainly changes with the filament stiffness than the hook stiffness. Calculating the stable orientation of the cell body demonstrates that the long axis of the cell body is more parallel to the surface as the hook or the filament is stiffer. In our simulations, this angle varies from 6.4° to 3.3°, depending on the stiffnesses. Like the pusher mode, the cell body more freely tilts upwards when the filament and hook are more flexible, hence the cell body gets a larger angle with respect to the surface.

3.4.4 Hook instability

As already stated in section 1.2, the hook in uniflagellated bacteria is very flexible and easily becomes unstable (buckled) if it is subjected to a load which is more than a critical value. When bacteria swim toward a boundary, the load on the hook gradually increases due to the no-slip boundary viscous forces, and therefore the hook is much more susceptible to becoming unstable.

In this section, we choose the hook's relative stiffness and the motor torque in a way such that the hook is stable and the applied load to the hook is very close to its critical value as the pusher model bacterium swims in an unbounded fluid. Our tests in unbounded space show that in a fixed motor torque $T = 1$, the critical rigidity of the hook is $k_H \approx 0.105$.

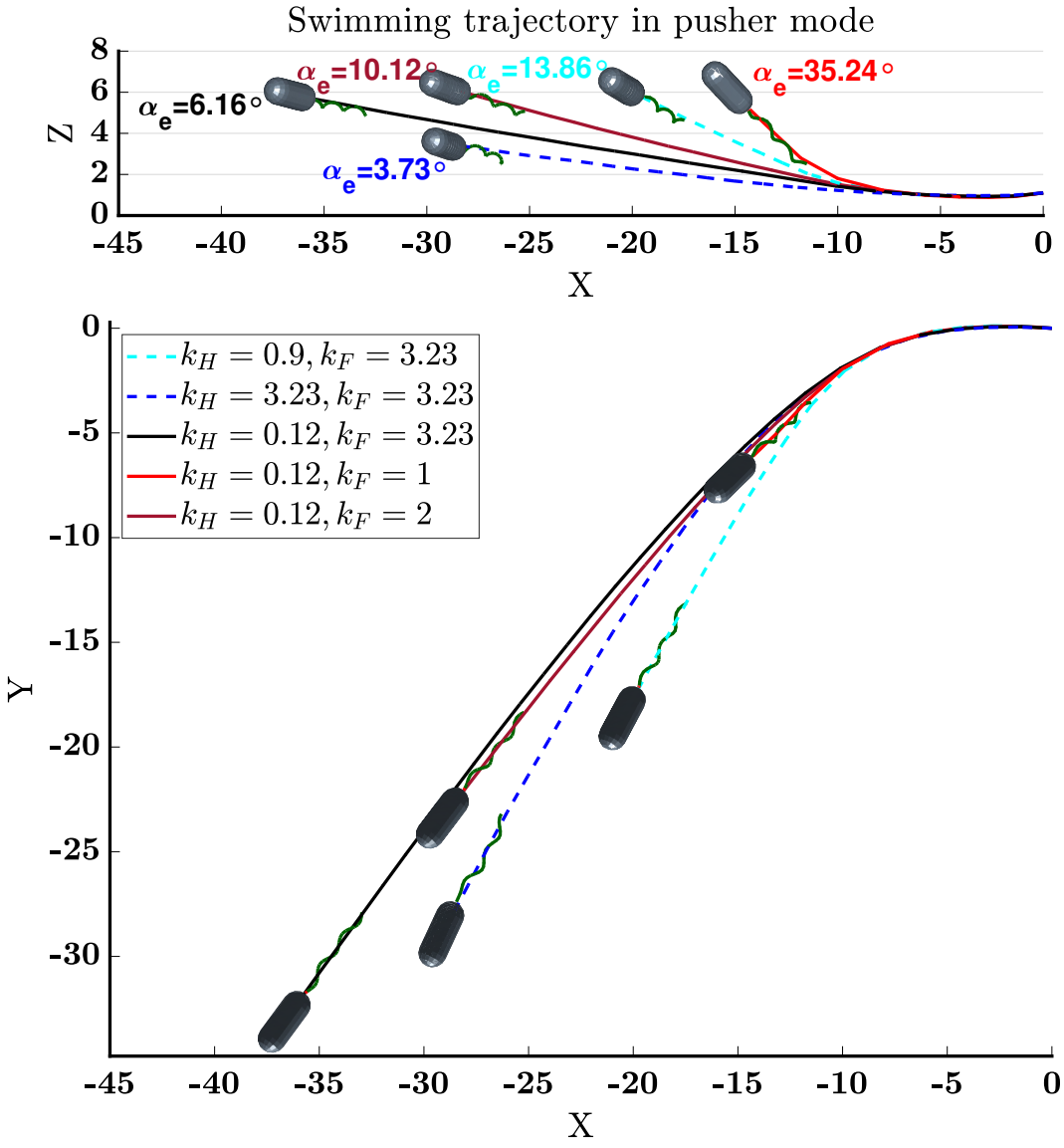

Figure 3.8: Swimming trajectories of the pusher-mode model bacterium in the different flagellum and hook stiffnesses. The concentration of NaCl is medium in all cases. Excluding the flagellum/hook stiffness, the physical properties of the model bacteria are according to Tab. 3.1.

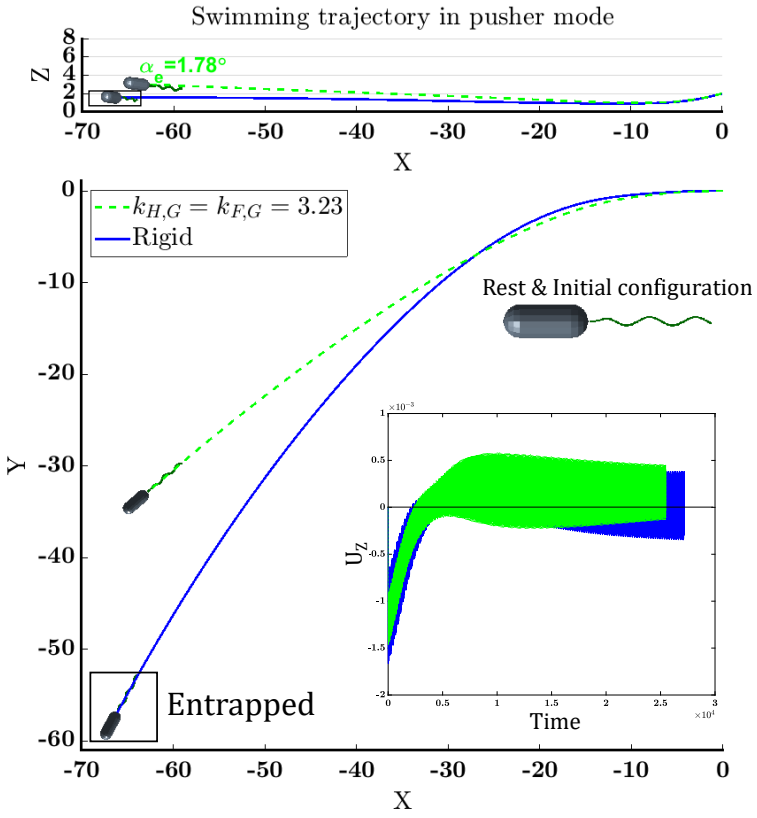

Figure 3.9: The uniflagellated model bacterium with rigid flagellum is entrapped by the surface, whereas it is pushed back as the flagellum is flexible. The amplitude growing factor $k_E = p$ is used to describe the flagellum shape and align the flagellum and cell body axes. There is no hook and the entire filament's relative stiffness is $k_F = 3.23$. The concentration of NaCl is medium.

Therefore, we choose the minimum rigidity $k_H = 0.106$ for the hook, and the motor torque $T = 1$ to study the locomotion of the pusher mode model bacterium near a surface. The other parameters are according to Tab. 3.1.

As shown in Fig. 3.11, the viscous forces due to the no-slip boundary cause the hook to become unstable. In this situation, the angle between the cell body's long axis and the flagellum axis increases so that the flagellum touches the cell body surface. In our simulations, the steric repulsion prevents the flagellum from touching the cell body surface. Misalignment of the cell body and flagellum axes results in a repetitive circular trajectory

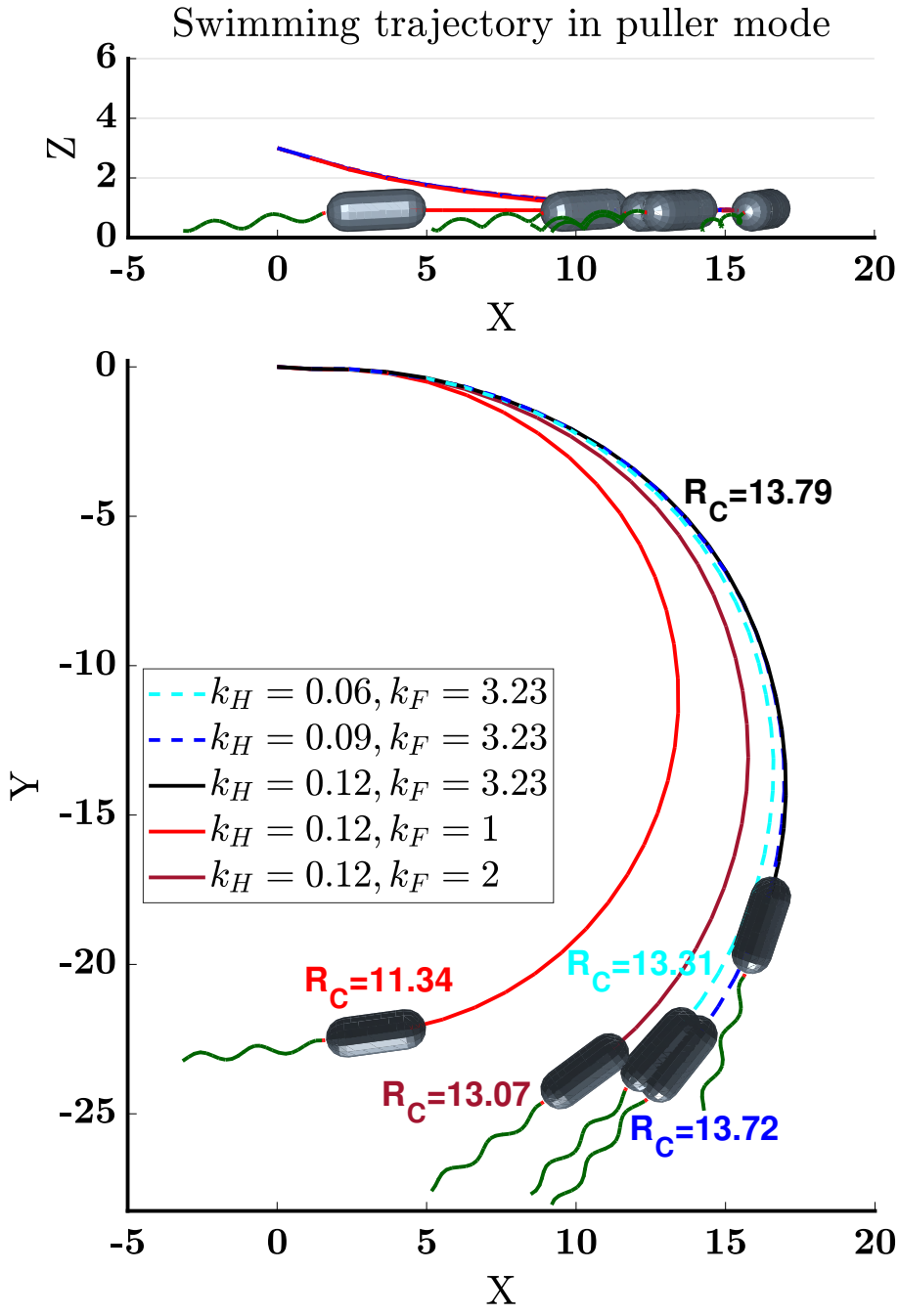

Figure 3.10: Swimming trajectories of the puller-mode model bacterium in different flagellum and hook stiffnesses. The concentration of NaCl is medium in all cases.

displayed in Fig. 3.11. In the low relative stiffness $k_H = 0.106$, it seems that the load on the hook is always above its critical value and thus the thrust from the flagellum causes spinning motion of the cell rather than directional propulsion of the body. As a result, the model bacterium is entrapped near the surface. Interestingly, experimental observations of *V. fischeri*'s locomotion near a surface have shown that some bacteria are locally entrapped at some points of the surface [119]. The hook instability, similar to what we see in this simulation, likely explains the high accumulation of *V. fischeri* at some points near the surface. By increasing the hook stiffness, the hook becomes more stable in wider ranges of viscous loads, therefore the angle between the cell body's long axis and the flagellum changes with the load applied to the hook. In this situation, the bacterium gradually gets away from the surface and the hook remains in its stable state by decreasing the no-slip boundary viscous load. In higher stiffness $k_H = 0.13$, the hook remains stable even near the surface and the bacterium moves on a trajectory as already seen in this section.

3.4.5 Cell body aspect ratio

Our results thus far have shown that the model bacterium (with aspect ratio $\alpha_{\text{cell}} = 2.5$) escapes from the surface regardless of the different flagellum stiffness, NaCl concentrations, and the initial conditions chosen in this study. Previous numerical investigations have shown that decreasing the aspect ratio of the cell body increases the pusher-mode bacteria's chance of entrapment near the surfaces [105]. To emphasize the importance of cell body aspect ratio in the entrapment of pusher-mode bacteria, we reduce the cell body's aspect ratio from 2.5 to 2.25 and 1.75. As expected and shown in Fig. 3.12, the escaping angle of the model bacterium decreases when the aspect ratio becomes 2.25. Further reduction of the aspect ratio (to $\alpha_{\text{cell}} = 1.75$), causes the bacterium to be entrapped by the surface. Our simulations demonstrate that independent of the initial distance from the surface, the bacterium reaches a unique stable distance $H_c = 1.71$ from the surface when the aspect ratio is $\alpha_{\text{cell}} = 1.75$.

Having found that for $\alpha_{\text{cell}} = 1.75$, the model bacterium with flexible flagellum and hook is attracted to the surface, we next consider the motion under higher concentrations of NaCl to see whether this qualitatively affects the behavior near boundaries, Interestingly, the model bacterium escapes from the surface when the concentration increases from medium to high, as shown in Fig. 3.13. This result is consistent with experimental evidence that the concentration of ions changes the pusher-mode bacteria's behavior in boundary accumulating; specifically, they tend to escape from the surfaces at higher concentrations of NaCl.

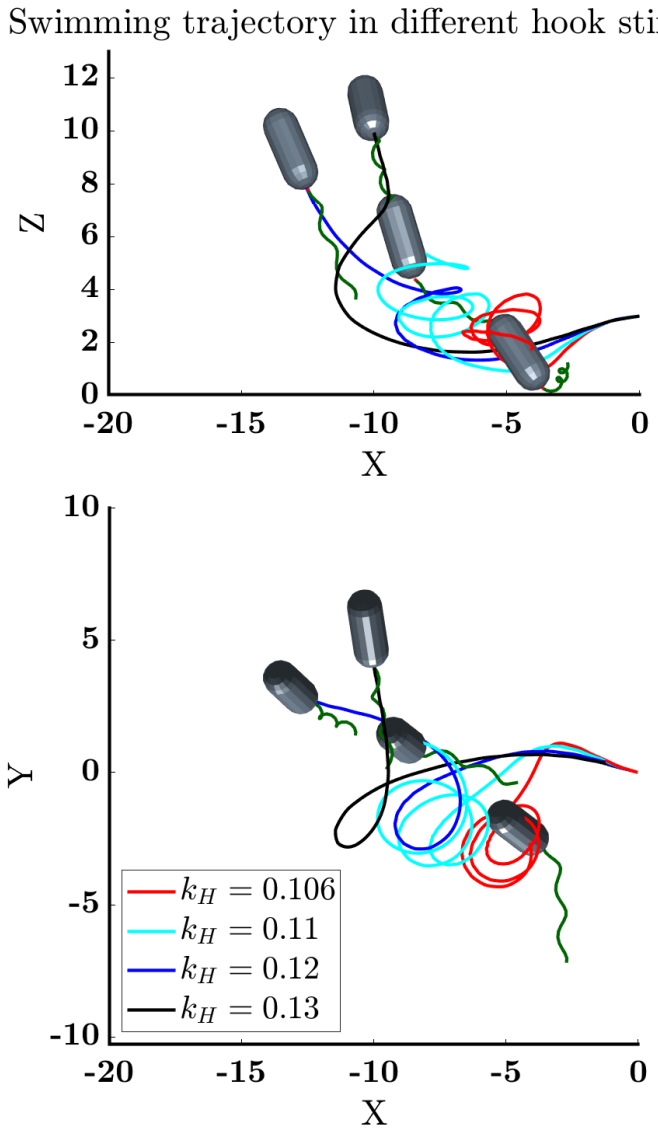

Figure 3.11: High viscous forces near a planar surface increase the load applied to the hook and make it unstable. As the bacterium gets away from the surface, the hook becomes stable and the bacterium travels on a straight trajectory. When the hook's relative stiffness is slightly above its critical value ($k_H = 0.106$), the bacterium is unable to escape from the surface.

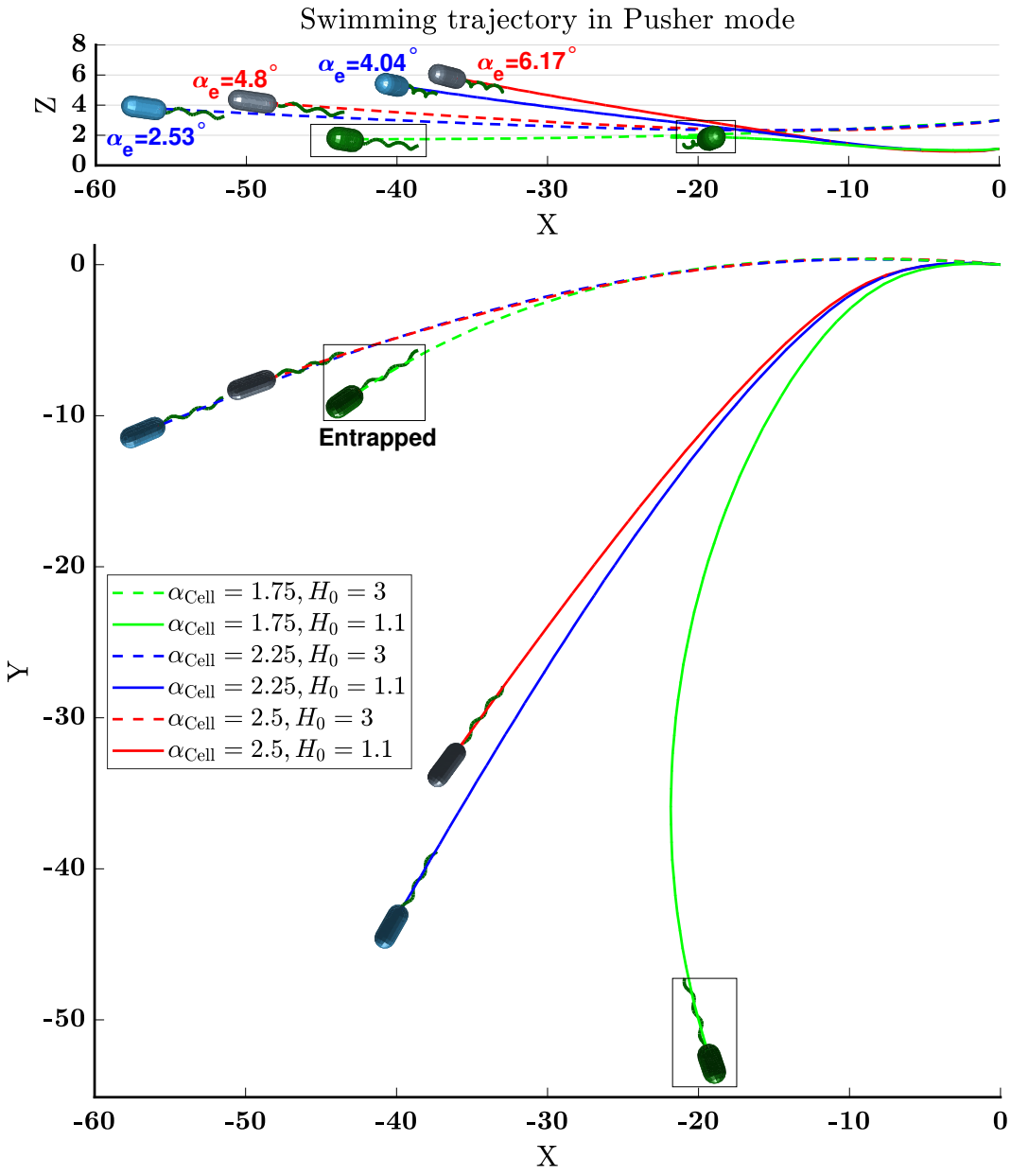

Figure 3.12: Swimming trajectories of the pusher-mode model bacterium in different cell body aspect ratios. The bacteria with the largest cell body's aspect ratio, $\alpha_{\text{Cell}} = 2.5$, escape from the surface with relatively large angles. In the smallest aspect ratio, $\alpha_{\text{Cell}} = 1.75$, the bacteria are entrapped near the surface. The concentration of NaCl is medium in all cases.

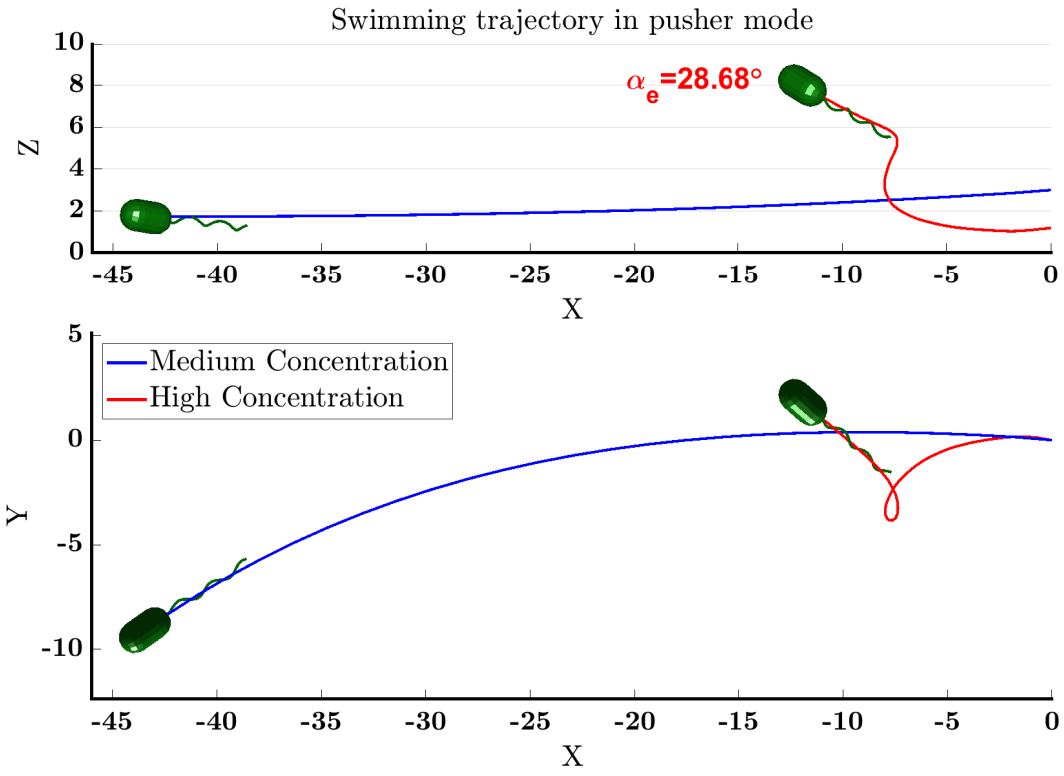

Figure 3.13: Changing the ions concentration from medium to high causes the boundary accumulating pusher-mode bacteria to escape from the boundary. In these simulations, $\alpha_{cell} = 1.75$, and the other parameters are stated in Tab. 3.1.

3.5 Summary and conclusion

The main aim of this chapter is to model and analyze the near-surface motion of uni-flagellated bacteria with flexible hook and filament by focusing on *V.alginolyticus*. By employing experimental measurements to relate the flagellar motor torque to its frequency, we note that the steady-state point in the torque-frequency plot is different in the puller and pusher modes. In comparison to the pusher mode, the larger amplitude of the flagellum in the puller mode changes the steady-state point and causes the model bacterium to swim faster in this mode. Unlike the constant speed flagellar motor, our results in this study indicate that the swimming speed of the model bacterium does not change significantly with the flagellum stiffness as the motor applies a constant torque to the flagellum.

Experimental observations have shown that the accumulation of *V. alginolyticus* near surfaces changes with the concentration of sodium chloride in the swimming medium. Depending on the swimming mode (pusher/puller), the relationship between the ions concentration and the tendency to swim near the surfaces could be direct or inverse [126]. We confirm that changing the ions concentration affects the near-surface behavior of bacteria. In particular, for certain geometries and mechanical properties of the model bacterium, the pusher mode swimmer is attracted to surfaces at low ion concentrations and escapes at high concentrations. In this regard, comparing the escaping angles of the pusher-mode model bacterium in different concentrations of NaCl shows an inverse relationship between these parameters. Further investigation indicates that this conclusion is independent of the initial conditions of the bacteria.

By contrast, our results in the puller mode show that if the model bacterium with a certain geometry is attracted to a surface in a specific concentration of NaCl, variation in the ion concentration only impacts the size of the circular orbits and also the stable orientation of the cell body with respect to the surface. In particular, the model bacterium tends to move on smaller circular paths in higher concentrations of NaCl. Despite the fact that several simplifications are taken into account to mimic the *V. alginolyticus* locomotion, the radius of the circular orbits in the puller mode ($R_c \approx$17.5 µm dimensionalized by the averaged radius $\overline{R}$) are comparable with the experimental measurements of Wu et al. ($R_c \approx$10-155 µm) [126].

In addition to *V. alginolyticus*, boundary accumulating and boundary escaping behavior has been observed in *Caulobacter crescentus* [62]. It is shown that this species is attracted to and escaped from the surfaces in the puller and pusher modes, respectively. *Caulobacter crescentus* is a monotrichous bacterium with a roughly spherocylindrical cell body and its flagellum length is close to *V. alginolyticus*. Therefore, the obtained results in this chapter and subsequently the explanations provided for the behavior of the model bacterium near the surfaces can extend to *Caulobacter crescentus* to justify its boundary accumulating or escaping behavior.

We note that the flexibility of the hook and filament (as long as they are in a stable state) facilitates the escaping from the surface by allowing the cell body to tilt upward more freely. Our simulations illustrate that the flexibility of the flagellum may change a pusher-mode model bacterium state from boundary accumulating to boundary escaping, for example. In general, it seems that there is an inverse relationship between the cell body's long axis angle with the surface and the hook/filament's relative stiffness in either puller or pusher modes.

Higher viscous forces applied to the flagellum and the cell body as the bacterium swims

near the surface, may cause the hook to become unstable. It requires that the load tolerated by the hook surpasses a critical value which exists for that specific rigidity of the hook. This kind of instability may lead to local entrapment of the bacteria near the surfaces. The variation in the viscous load near the surfaces may lead to a shift from an unstable to a stable state and vice versa. This transition between the states may help the bacteria to get away from the surface.

The simulations show that the pusher-mode bacterium with a flexible hook and filament is entrapped by the flat surface when the cell body has a small aspect ratio. This transition from escaping state to entrapment state in a specific aspect ratio of the cell body is already well studied for the bacteria with rigid flagellum [105]. Here, comparing the near-surface behavior of a model bacterium with a rigid and flexible flagellum, demonstrates that the flexibility of the flagellum can slightly change the threshold of the cell body aspect ratio for the surface entrapment.

To sum up, whereas a lot of investigations in studying the uniflagellated bacteria locomotion are done by assuming that the bacterial flagellum is rigid, our results in this chapter clearly show the hook and flagellum flexibility may change the bacteria behavior, especially in contact with a planar surface. For example, it may change the bacteria's behavior from boundary accumulating to boundary escaping or cause the bacteria to be locally entrapped near the surfaces. Therefore, it is necessary that more special attention is given to the hook and filament flexibility in studying the uniflagellated bacterial behavior.

Chapter 4

Locomotion of Biflagellated Bacteria

4.1 Introduction

A deep understanding of bacterial morphology and behavior is crucial to minimize undesirable and maximize the beneficial effects of microorganisms on human health and welfare. Interestingly, functionalities and mechanisms of some microrobots with promising biomedical applications are motivated by flagellated bacteria; therefore, investigating the influences of different types of flagella (puller/pusher) and their arrangement on the microrobots' locomotion paves the way to optimize and enhance the performance of the microrobots.

Motivated by experimental observations of MC-1 locomotion in unbounded fluid [6], we use our elastohydrodynamic model to study the motility of a biflagellated bacterium with one puller and one pusher flagella in this chapter. The pusher and puller flagella are both right-handed helices but rotate in the clockwise (CW) and counterclockwise (CCW) directions respectively (viewed with the flagellum between the cell body and the observer) and hence apply "pushing" and "pulling" forces respectively on the cell body. Generally, the bacterium then swims with the pusher flagellum at the rear of the cell body and the puller flagellum in front of the body. Such a morphology is inspired by the observations of Bente et al. [6], in which they concluded that *M. marinus* most likely swims with one puller and one pusher flagellar bundle.

Since the structure of the hook and its properties in MC-1 (a strain of *M. marinus*) are not well studied, there would be a lot of uncertainties in modeling the hook effects on the swimming of MC-1. For this reason, we neglect the specific role of the hook in our

model bacterium in this chapter, assuming that the properties of the hook are the same as those of the rest of the flagellum. Unlike many kinds of bacteria, MC-1 has two sheathed bundles of flagella on one side of the cell body. Since each bundle of flagella is modeled by a single flexible filament, wherever we refer to a flagellum or flexible filament in our results, it should be interpreted as a sheathed flagellar bundle in MC-1.

In this chapter, we first compare the swimming styles of three model bacteria (pusher, pusher-pusher, puller-pusher) to shed light on the effects of the flagella type on the swimming properties of the bacteria. Next, the influences of various parameters including the flagellar stiffness, position, orientation, and the ratio of the two motors' torques on the swimming characteristics of the puller-pusher bacterium are studied and compared with the experimental measurements. We finally investigate the influences of an external magnetic field and its variation on the locomotion of the model bacteria with one and two pusher flagella.

4.2 Geometric model

The model bacterium consists of one rigid spherical cell body, one puller flagellum (dark slate gray), and one pusher flagellum (gray), as shown in Fig. 4.1. The cell body has centroid position denoted by $\vec{X}^{(B)}$ and orientation described by the basis $\left\{\vec{e}_1^{(B)}, \vec{e}_2^{(B)}, \vec{e}_3^{(B)}\right\}$. The pusher flagellum has position $\vec{X}^{(1)}$ and basis $\left\{\vec{e}_1^{(1)}, \vec{e}_2^{(1)}, \vec{e}_3^{(1)}\right\}$, and the puller flagellum has position $\vec{X}^{(2)}$ and basis $\left\{\vec{e}_1^{(2)}, \vec{e}_2^{(2)}, \vec{e}_3^{(2)}\right\}$. All of the aforementioned bases are right-handed and orthonormal. In this study, it is assumed that the two flagella have identical physical and elastic properties and their initial and rest configurations are right-handed helices with centerlines given by

$$\vec{\Lambda}^{(i)}(\xi) = \vec{X}^{(i)} + \xi\vec{e}_1^{(i)} + \Xi(\xi)\cos(2\pi\xi/p)\vec{e}_2^{(i)} + \Xi(\xi)\sin(2\pi\xi/p)\vec{e}_3^{(i)}, \tag{4.1}$$

where $i = 1, 2$ for the pusher and the puller flagella respectively; the variable ξ parameterizes the distance along the axis of the helix with $0 \leqslant \xi \leqslant L_F$, $\Xi(\xi) = a(1 - e^{-(k_E\xi)^2})$ is the helix amplitude function, and a, p, and k_E represent the maximum helix amplitude, the helix pitch, and the amplitude growth rate (the amplitude grows from zero to a over a region of length roughly $\frac{2}{k_E}$), respectively.

The position and orientation of the puller flagellum is specified by two angles α and β defined on the $\vec{e}_1^{(B)}$–$\vec{e}_3^{(B)}$ plane through the center of the cell body. The pusher flagellum is placed symmetrically on the other side of the cell body with the same acute angles as

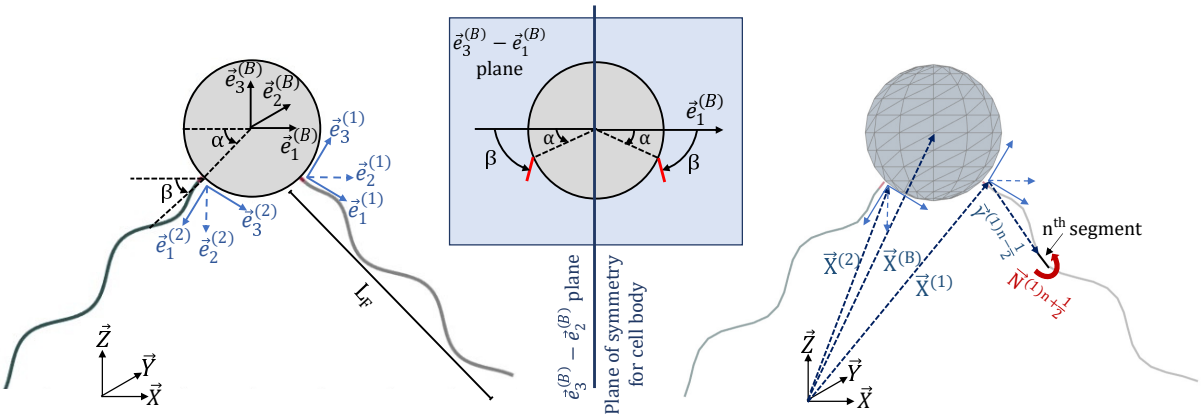

Figure 4.1: A schematic view of the model bacterium in which different bases and vectors are used to describe the position and orientation of the components. α and β angles represent the position and orientation of the rotors on the cell body and are defined with respect to $\vec{e}_1^{(B)}$. The internal moment between the nth and $(n+1)$st segments is denoted by $\vec{N}^{(i)n+\frac{1}{2}}$. Note that the thickness of the flagella in the figures does not reflect the actual thickness of the flagella in the model bacterium.

the puller flagellum (Fig. 4.1). In all simulations, except one set of simulations where we specifically study the influence of β angle, we assume that the flagella rotors are normal to the cell membrane (i.e. $\beta = \alpha$). In studying the influence of β, we fix the angle α, and $|\alpha - \beta|$ represents how much the rotors deviate from being normal to the cell membrane.

The experimental observations have shown that *M. marinus* cell body is approximately spherical [6, 119]. Based on the measurements for MC-1, the cell body diameter is $1.3 \pm 0.1\,\mu$m and the flagellum length is $3.3 \pm 0.4\,\mu$m [6]. We are unaware of any study that measures the flexibility of the flagella or flagellar bundles in MC-1. Recalling that a filament in our model represents multiple flagella in a bundle, we use values of the rigidity about 1.5-11 times that of a flagellum in *E. coli* ($3.5\,\text{pN}\,\mu\text{m}^2$ [29]). Other parameters in this study, such as the motors' torques, helical pitch and amplitude are chosen from the values given by [6, 74] and [106]. Here, these parameters are non-dimensionalized by the averaged cell body radius $0.65\,\mu$m [6], *M. marinus*'s motor torque which is roughly $12\,\text{pN}\,\mu$m [6] and the swimming fluid viscosity $\mu = 10^{-3}\,\text{Pa}\,\text{s}$. We characterize the flexibility of the flagella by a relative stiffness defined as

$$k_F = \frac{EI}{\overline{T}\,R}, \tag{4.2}$$

where E is Young's modulus of the material, I is the moment of inertia of the flagella cross

Table 4.1: Parameters defining the shape of the biflagellated model bacterium and simulation settings.

Description	Symbol	Dimensionless	Dimensional
Radius of cell body	R	1	0.65 µm
Flagella diameter	d	0.1	0.065 µm
Each filament total length	l	5	3.25 µm
Flagella rest/initial pitch	p	2	1.3 µm
Flagella rest/initial amplitude	a	0.2	0.13 µm
Amplitude growth factor	k_E	2	$4.73\,\mu m^{-1}$
Flagella relative stiffness	k_F	1	-
(Flexural rigidity)	(EI)	-	$(7.8\,pN\,\mu m^2)$
Number of segments on each flagellum	N_S	30	30
Number of triangular elements on the cell body	N_B	112	112
Pusher flagellum motor torque in $\vec{e}_1^{(1)}$ direction	T_1	-1	-12 pN µm
Puller flagellum motor torque in $\vec{e}_1^{(2)}$ direction	T_2	1	12 pN µm
Flagella rest/initial orientation (rotor orientation) with respect to $\vec{e}_1^{(B)}$	β	45°	45°
Motor position with respect to $\vec{e}_1^{(B)}$	α	45°	45°
Fine time step	Δt_{fine}	4×10^{-4}	9.2×10^{-9} s
Coarse time step	Δt_{coarse}	3.2×10^{-2}	7.36×10^{-7} s
Total swimming time	T_s	1000	0.023 s

section, $\overline{T} = \frac{T_1+T_2}{2}$ is the averaged motor torque, and R is the radius of the cell body. By Eq. 4.2, the dimensionless relative stiffness value $k_F = 1$ is achieved for the motor torque and the cell body radius stated above, and flexural rigidity $EI = 7.8\,pN\,\mu m^2$, which is 2.2 times the rigidity of an *E. coli* flagellum.

4.3 Swimming style

We first compare the swimming trajectories and speeds of three model bacteria with one pusher flagellum, two pusher, and puller-pusher flagella. In this regard, all physical parameters of the models are as listed in Tab. 4.1 and only the number of the flagella and the motors' rotation direction differ between the cases.

As shown in Fig. 4.2, when the model bacterium has one or two pusher flagella and the position and orientation of the flagella are symmetric, it approximately swims in a straight line. Closer inspection indicates a wiggling of the cell body about the swimming line. In fact, the trajectories are actually helical with very small amplitudes and pitches induced by the flagella rotations. In general, the rotating flagellum produces thrust that is not precisely aligned with its axis, and therefore the instantaneous swimming velocity is not perfectly parallel to the flagella axes. As presented in Tab. 4.2, comparing the averaged swimming speed ($\overline{U}$), calculated as the norm of the average of the instantaneous velocity vector over an integer number of periods of the trajectory, indicates that the pusher-pusher model bacterium swims about 60% faster than the pusher model bacterium. We note that this is less than the 85% speed increase reported in a previous numerical study [106], where the flagella were rigid and the motors were aligned with the swimming direction ($\beta = 0$). In our simulations, we use $\beta = 45°$, which means that the motor torques are not aligned with the swimming direction. More significantly, the flexibility of our flagella allows them to bend under viscous stresses, altering the propulsion efficiency. The flexibility is particularly consequential when the rest orientations of the two flagella are not symmetrical. In such a configuration, the bundling effect of two pusher flagella decreases the degree of asymmetry and helps the bacterium to move on a smooth trajectory. In particular, the bacterium exhibits a kind of double helical trajectory with small amplitude and long pitch

Unlike the swimming speed, the rotation rate of the cell (calculated as the norm of the average of the instantaneous angular velocity vector) does not differ significantly between the pusher cases. In other words, increasing the number of flagella from one pusher to two with $\beta = 45°$ and $\alpha = 45°$, the swimming speed increases whereas the rotation rate of the cell body is not significantly changed. Adding a flagellum increases the total torque on the cell body from the motors so one might expect the body rotation rate to increase. Placing the motors far apart, as in the present case, reduces the rotation rate necessary to balance the increased torque. A reduced body rotation rate could have a beneficial effect on the propulsive thrust because the cell body rotation diminishes the net rotation of the flagella with respect to the ambient fluid.

The puller-pusher bacterium has a qualitatively different swimming style from the pusher and pusher-pusher (Fig. 4.2). The difference in average swimming direction, compared with a pusher-pusher bacterium with the same initial configuration, is due to an inversion of the propulsion direction of the puller flagellum. The puller-pusher bacterium swims with the pulling flagellum in front and the pushing flagellum at the rear. The asymmetric distributions of propulsive forces and torques from the two flagella cause the model bacterium to move on a double helix trajectory. The helical form with a longer pitch and larger amplitude corresponds to the slow rotation of the cell body about the swimming

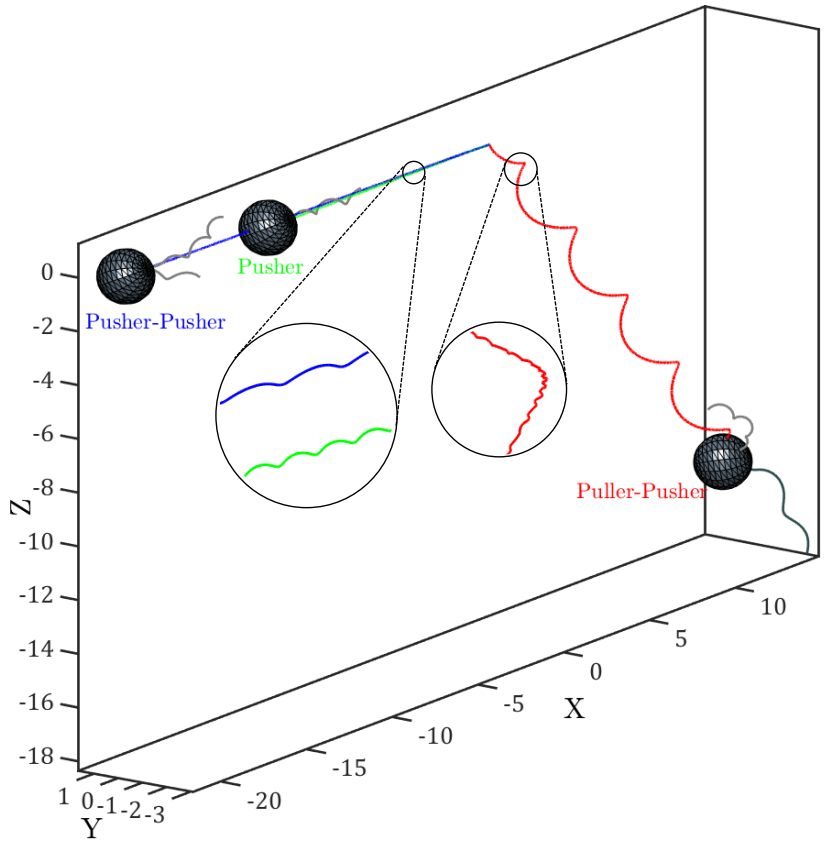

Figure 4.2: Swimming trajectories of three studying cases which differ in number and types of flagella. All physical parameters are chosen according to Supplementary Information table S1 and the initial conditions and orientations are set to be equal for three cases.

direction while the smaller pitch, smaller amplitude oscillations are due to the revolutions of the flagella. Moving on such a trajectory decreases the model bacterium displacement and leads to a smaller averaged translational speed than the pusher-pusher case.

As already stated, pusher-pusher configurations of two flagella may lead to double helical trajectories in addition to the puller-pusher configuration. Our simulations indicate that there is a correlation between the degree of the asymmetry (asymmetric cell body shape, flagella positions and orientations, the magnitude and orientations of the propulsive forces) and the properties of the large helices. In the studied puller-pusher model bacteria, the rest configurations are almost symmetrical but the differences in the magnitude and orientations of two propulsive forces (one for the pusher flagellum and one for the puller one) induce a torque on the cell body that leads to the rotation of the cell body in the

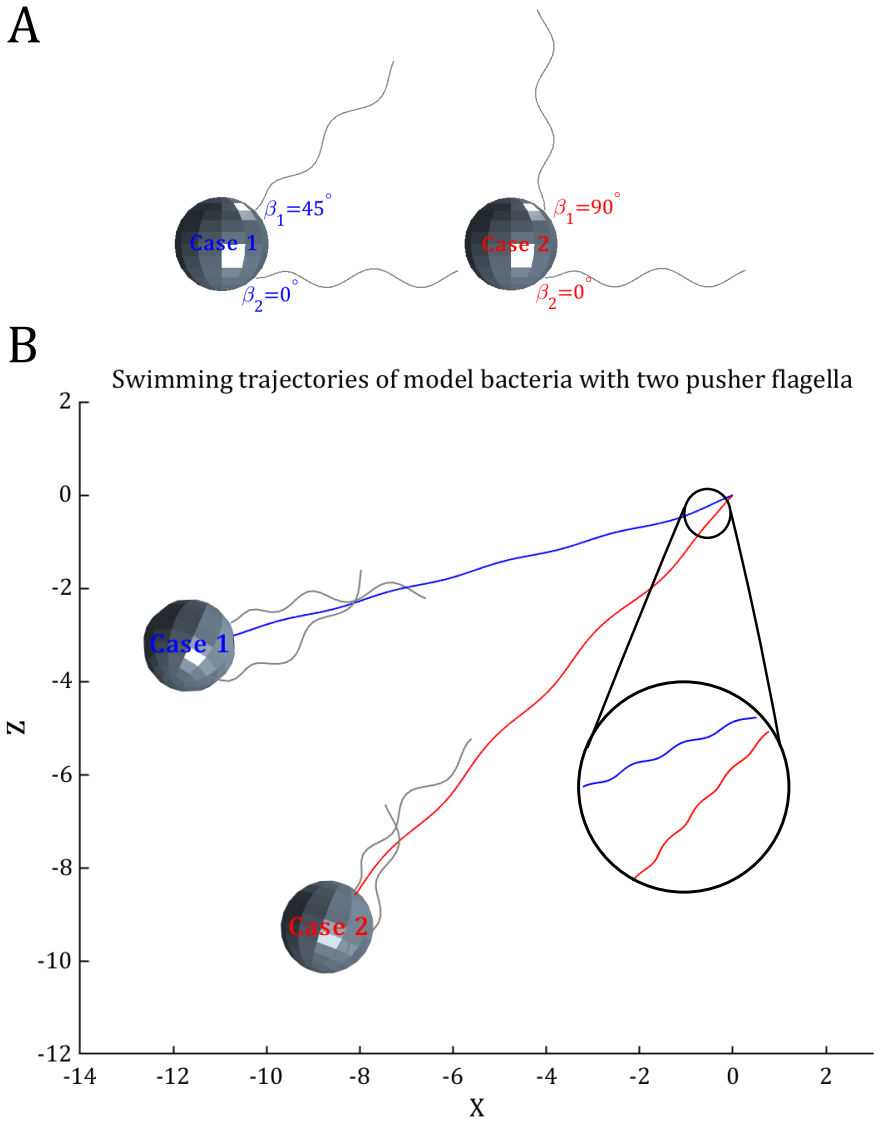

Figure 4.3: A) Model bacteria with two asymmetric pusher flagella. B) Trajectories of the model bacteria with two asymmetric pusher flagella

Table 4.2: Comparing the swimming features of three model bacteria which differ in terms of number and types of the flagella.

Case	$\overline{U} \times 10^3$	$\overline{\Omega} \times 10^3$
Pusher	14.2	36.15
Pusher-Pusher	23.1	36.19
Puller-Pusher	20.9	34.05

directions other than its spinning. In fact, this rotation is responsible for the appearance of the second (large) helix.

In a pusher-pusher model bacterium with a symmetrical configuration, the average effective torque induced by the propulsive forces on the cell body is near zero, and therefore the bacterium moves on a single helical trajectory, as shown in Fig. 4.2. The second (larger) helix appears in the trajectory of the pusher-pusher model bacterium as the rest configuration of the model bacterium is geometrically asymmetrical. To quantitatively compare the properties of the trajectories in puller-pusher and pusher-pusher model bacteria, we have plotted the trajectories of two pusher-pusher model bacteria with different degrees of asymmetry in Fig. 4.3. The properties of both model bacteria are as stated in Tab. 4.1 and only the orientation of the first flagellum distinguishes Case 1 from Case 2. As expected, the size of the large helix increases by the degree of asymmetry. Our measurements indicate that the pitch and diameter of the large helix in Case 1 (less-symmetrical) are 2.52 and 0.15, respectively, whereas they are 3.71 and 0.26, respectively, in Case 2. Comparing these values with the closest case in the puller-pusher configuration (pitch: 3.91 and diameter: 1.08) demonstrates that the amplitude of the large helix is several times smaller in the pusher-pusher configuration. This difference is likely due to the bundling effect of the two pusher flagella; flexible flagella have a tendency to bend towards each other, reducing the degree of the asymmetry in the pusher-pusher configuration and therefore causing the bacterium to swim smoothly on a smaller helix.

To characterize the locomotion of the bi-flagellated bacteria with puller-pusher flagella, we study the influences of different physical parameters, including the flagella stiffness (k_F), position (α angle), orientation (β angle) and the motor torque ratio (R_T), on the swimming characteristics of the model bacterium. In the presented trajectories, the initial orientation of the model bacterium is as shown in Fig. 4.1 and the physical parameters are according to Tab. 4.1 except a parameter studied specifically. One of the aims of this study is to compare the properties of the swimming trajectories with the experimental measurements to shed light on the morphology of MC-1. It is worth mentioning that we

do this comparison by assuming that the bacterium has puller-pusher flagella and the cell body is approximately spherical. The measurements of Bente et al. [6] have demonstrated that MC-1 cells move on a large helix with dimensionless pitch 8.1 ± 2, diameter 2.6 ± 0.3 and instantaneous speed $(3.5 - 17.6) \times 10^{-3}$. Since changing the flagella arrangements and motors torques mainly affect the size of the large helices, our focus is on comparing the size of the large helices in this study.

We characterize the orientations of the cell body, the puller, and pusher flagella with respect to the swimming direction (axis of the large helix) by introducing the acute angles η_{Cell}, η_{Puller} and η_{Pusher}. In this regard, η_{Cell} represents the time-averaged (over one complete turn on the large helix) angle between $-\vec{e}_1^{(B)}$ and the swimming direction. We also calculate η_{Puller} and η_{Pusher} by time-averaging the acute angle between the line connecting the driven ends of the flagella to their free ends and the swimming line. Variations of these angles with respect to the studied parameters are presented in Fig. 4.4. We will refer back to this figure in each of the following subsections.

4.4 Flagella stiffness

Forces and torques from hydrodynamic interactions and the flagellar motors deform the flagella out of their initial equilibrium configuration. These deformations are significant if the flagella have low relative stiffnesses and negligible if they have high stiffnesses. We varied the relative stiffness k_F from 0.7 to 5 as listed in Tab. 4.3, using the same stiffness for the puller and pusher flagella in each case. Our simulations demonstrate that the pusher flagellum reaches a stable overwhirling state [86] when its relative stiffness is $k_F = 0.75$ or lower; the rotation is stable twirling for all of the higher values of k_F. We observed stable twirling motion of the puller flagellum in all the studied cases. As shown in Fig. 4.5, the overwhirling motion of the pusher flagellum significantly affects the small helices of the trajectory and decreases the pitch of the large helix.

It is also evident that the axis of the twirling pusher flagellum is approximately aligned with the swimming direction whereas the overwhirling pusher flagellum is not aligned with the swimming direction. This is shown quantitatively in Fig. 4.4A, where we plot the orientation angles between the axes of the flagella and the average swimming direction. The pusher flagellum orientation angle changes from almost parallel to the swimming direction ($\eta_{\text{Pusher}} \approx 23^\circ$) for twirling motion at $k_F = 0.85$ to almost perpendicular ($\eta_{\text{Pusher}} \approx 77^\circ$) for overwhirling motion at $k_F = 0.7$. The overwhirling flagellum is therefore unable to effectively propel the cell body, leading to a significant drop in swimming speed at the onset of the overwhirling regime (see Tab. 4.3).

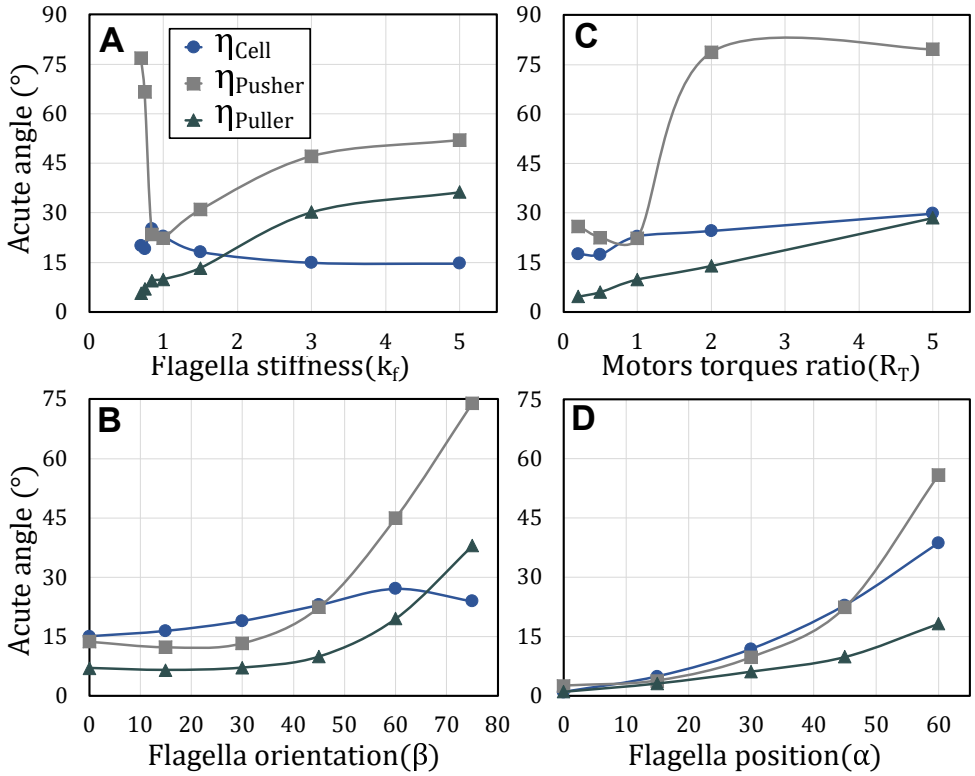

Figure 4.4: The time-averaged orientations of the cell body (η_{Cell}), the puller (η_{Puller}) and pusher (η_{Pusher}) flagella with respect to the time-averaged direction of the swimming. These plots are presented for A) Different flagella stiffnesses. B) Different flagella orientations. C) Different motors torques ratios. D) Different flagella positions.

Since we prescribe a rest orientation angle $\beta = 45°$ between the axes of the flagella and the $\vec{e}_1^{(B)}$ direction, the flagella are not well aligned with the swimming direction if the relative stiffness k_F is high. Therefore, the cell body moves on larger helices and exhibits larger oscillations (Fig. 4.6) that result in smaller averaged translational and rotational speeds. For lower relative stiffnesses, provided the flagellum remains in the twirling regime, the flagella bend more and align better with the swimming direction (as illustrated in Fig. 4.5). Thus, the model bacterium undergoes less wiggling and travels on helical trajectories with smaller pitches and diameters. The reported results in Tab. 4.3 indicate that the instantaneous speed changes much less than the average speed at the transition between the twirling and the overwhirling motion of the pusher flagellum. This suggests that the overwhirling flagellum still produces thrust but a large component of this thrust is in the

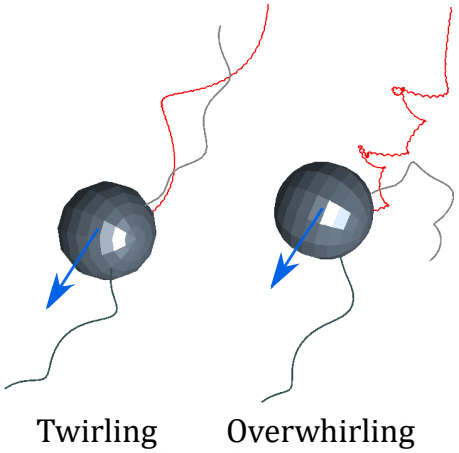

Figure 4.5: Influences of the pusher flagellum overwhirling motion on the swimming trajectory of the model bacterium. In this motion, the flagellum experiences large deformations and the free end of the flagellum is close to the driven end.

lateral direction. The maximum instantaneous speed is attained at intermediate values of relative stiffness, around $k_F = 1.5$. In this study, the instantaneous speed ($\hat{U}$) is calculated by dividing the arc length of one turn of the large helix by the time period for completing one turn. Comparing the obtained results with the experimental measurements (dimensionless pitch 8.1 ± 2.0, diameter 2.6 ± 0.3, speed $(3.5 - 17.6) \times 10^{-3}$) indicates that for high flagella stiffnesses ($k_F = 3, 5$) the diameters and the pitches of the swimming trajectories are within the range measured experimentally, whereas the simulated instantaneous speeds are about 40% higher than the high end of the experimental range. The obtained results,

Table 4.3: Comparing the swimming features of the puller-pusher model bacterium in different flagella stiffness

Stiffness	Pitch	Diameter	$\overline{U} \times 10^3$	$\overline{\Omega} \times 10^3$	$\hat{U} \times 10^3$
0.70	1.58	1.09	9.3	34.6	20.1
0.75	2.11	1.19	11.3	33.6	19.2
0.85	4.05	1.07	20.6	33.7	26.7
1.00	3.91	1.08	20.9	34.1	27.0
1.50	4.17	1.32	20.2	30.0	28.8
3.00	6.22	2.39	16.1	16.6	24.7
5.00	6.81	2.83	14.7	13.5	23.3

presented in Fig. 4.4A, indicate that the swimming direction is well aligned with the puller flagellum, but this tendency for the alignment slightly decreases at higher stiffnesses.

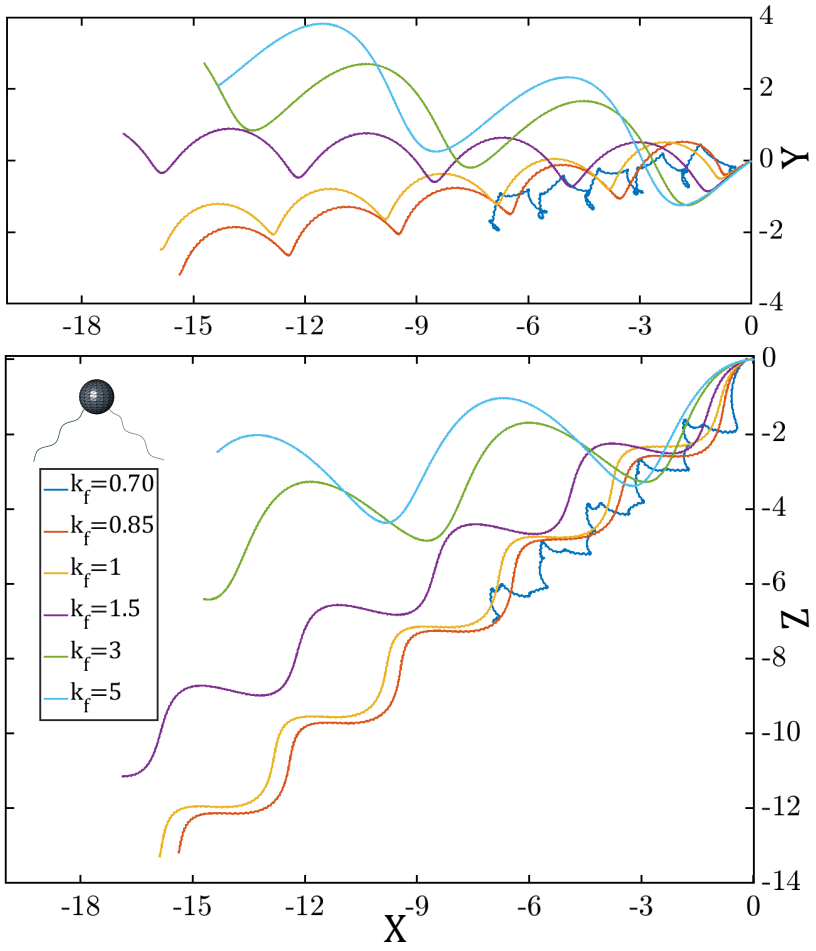

Figure 4.6: The swimming trajectory of the biflagellated model bacterium projected on XY and XZ planes in different flagella stiffnesses (k_F).

4.5 Flagella orientations

The orientation of the flagella relative to the cell body is an important aspect of the bacterial morphology but accurate experimental measurement of the orientations could be

Table 4.4: Comparing the swimming features of the puller-pusher model bacterium in different flagella orientations

β	Pitch	Diameter	$\overline{U} \times 10^3$	$\overline{\Omega} \times 10^3$	$\hat{U} \times 10^3$
0°	2.26	0.25	21.9	60.7	23.0
15°	2.63	0.47	22.1	54.4	26.4
30°	2.96	0.73	21.9	45.5	26.9
45°	3.91	1.08	20.9	34.1	27.0
60°	5.45	1.79	17.4	20.4	24.4
75°	5.86	3.37	8.9	9.7	17.6

quite challenging. We numerically investigate the sensitivity of swimming features to this parameter. By fixing $\alpha = 45°$ and varying β from 0° to 75°, we note that the pitches and diameters of the helical trajectories strictly increase with β, as shown in Fig. 4.7. Closer inspection indicates that the diameter grows faster than the pitch, so the helix angle (angle between axis direction and helix tangent) increases by β. Consequently, the projection of the bacterium displacement on the helical axis decreases; this explains the inverse correlation between β and the averaged translational speed. Investigation of the flagella orientations with respect to the swimming direction (Fig. 4.4B) can also justify the smaller swimming speeds for larger β ($\beta > 45°$) in which both puller and pusher flagella do not effectively propel the cell body in the swimming direction. Moreover, the reported results in Fig. 4.4B demonstrate that η_{Pusher} and η_{Puller} are insensitive to β when $\beta < 45°$ and hence the averaged swimming speed is expected to remain constant in this range. This sensitivity analysis shows that population variability and errors in measurement of β should not significantly affect predictions of swimming speeds of bi-flagellated bacteria as long as β is within the given range. As reported in Tab. 4.4, the simulations show that the instantaneous swimming speed $\hat{U}$ becomes maximum when the flagella are perpendicular to the cell body (i.e. $\beta = 45°$).

Since the cell body rotates to balance the vector sum of the two motor torques, changes in the motor torque directions can directly affect the cell body's rotation speed. Larger β leads to smaller magnitudes of the total torque from the puller and pusher motors; therefore, an inverse correlation is seen between the rotational speed of the cell body and β. Our results indicate that the angle between the swimming direction and the cell body orientation indicator (η_{Cell}) becomes maximum when β is about 60°.

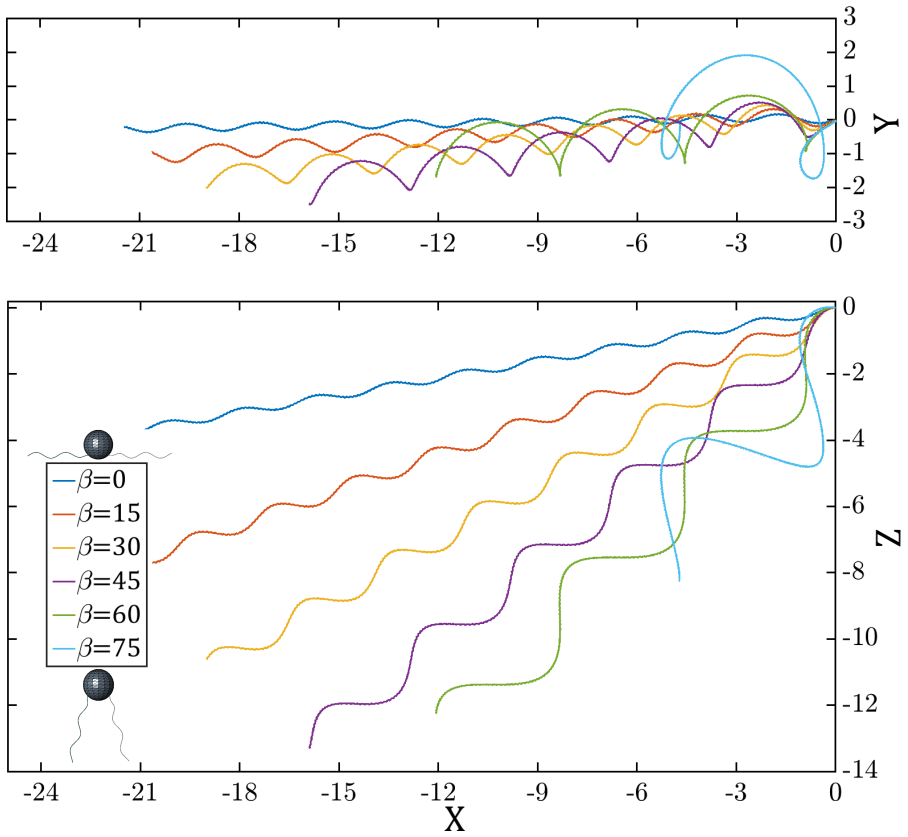

Figure 4.7: The swimming trajectory of the biflagellated model bacterium projected on XY and XZ planes as a function of the flagella orientations (β).

4.6 Flagella position

Hydrodynamic behaviors of multi-flagellated bacteria are mainly determined by the number, type, and distribution of flagella on the cell body. In the case of *M. marinus*, we are unaware of any precise experimental characterization of the relative positions of the flagella bundles on the cell body. Therefore, different possibilities for the flagella position on *M. marinus* are considered by varying α and keeping the flagella perpendicular to the cell body. We found that both pitch and diameter of the helical trajectories increase as the two flagella are placed closer together. For $\alpha = 0°$, the two flagella extend from opposite poles of the cell body and share a common axis, resulting in a relatively straight trajectory, as shown in Fig. 4.8. In this state, the instantaneous and the averaged velocities are almost

aligned and the averaged speed reaches its maximum. In contrast, the maximum instantaneous speed is achieved by the model bacterium when there is a small angle, $\alpha = 15°$, between the flagella and the cell body axis (see Tab. 4.5). The averaged cell body rotation rate reaches its maximum at $\alpha = 0°$, which is the configuration that maximizes the magnitude of the vector sum of the two motor torques. As shown in Fig. 4.4, the position of the flagella strongly affects the averaged swimming direction as well; particularly, the angle between $-\vec{e}_1^{(B)}$ and the average swimming direction increases by placing the flagella close together.

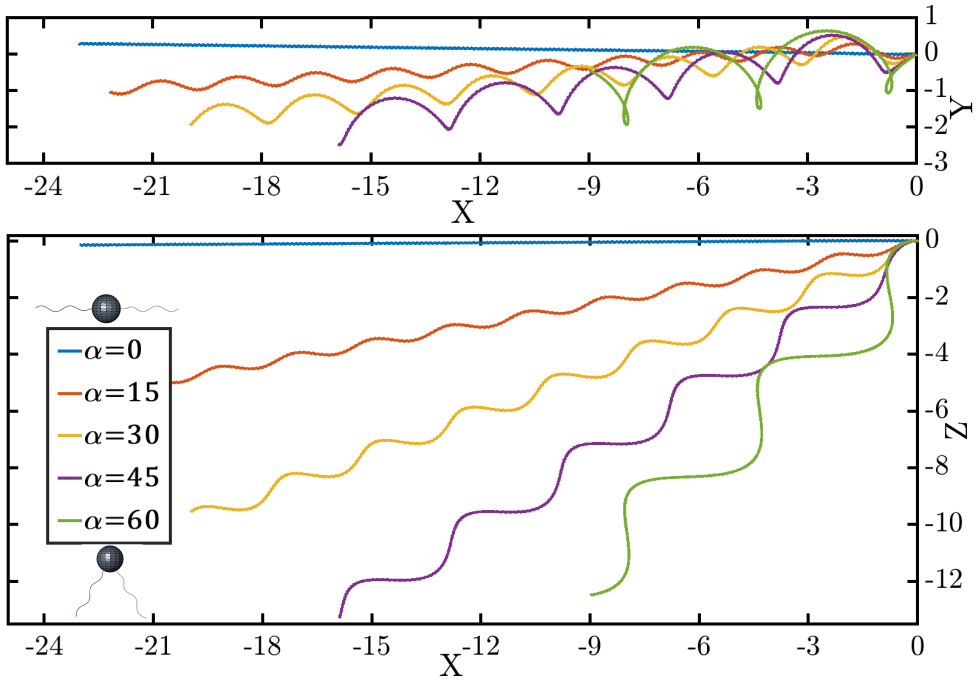

Figure 4.8: The swimming trajectory of the biflagellated model bacterium projected on XY and XZ planes by changing the flagella placed on the cell body (α).

Comparing the experimental measurements with the obtained results in Tab. 4.4 and Tab. 4.5, we see that the pitches and diameters of the large helices are almost all smaller than the experimental ranges (8.1 ± 2.0 and 2.6 ± 0.3, respectively, in dimensionless units). Recall that in section 4.4, we showed that the pitch and diameter of the large helix are closest to experimental values if the flagellar stiffness is about $k_F = 3$. Simulations for varying α and β were carried out with the lower stiffness of $k_F = 1$, which is roughly the value used in the simulations of Bente et al. [6]. We expect that closer matching to experiments could be achieved by simultaneously varying all three parameters, k_F, α, β.

Table 4.5: Comparing the swimming features of the puller-pusher model bacterium in different flagella positions.

α	Pitch	Diameter	$\overline{U} \times 10^3$	$\overline{\Omega} \times 10^3$	$\hat{U} \times 10^3$
0°	NA	NA	23.0	71.7	23.0
15°	2.25	0.34	22.9	66.1	28.0
30°	2.77	0.67	22.5	51.6	26.8
45°	3.91	1.08	20.9	34.1	27.0
60°	5.47	1.90	15.4	17.3	22.1

Nevertheless, our results demonstrate the sensitivity to the configuration of puller and pusher flagella; we obtain pitches varying by more than a factor of 2.5 and helical diameters varying by more than a factor of 13 as α and β are varied (excluding $\alpha = \beta = 0°$).

4.7 Motor torques

Depending on the external load and environmental stimuli like nutrient concentration, pH, etc., the flagella motors can generate different torques in both directions (CW/CCW) in many kinds of flagella-driven bacteria [78, 116]. In all simulations thus far, it is assumed that the puller and pusher flagella motors generate equal torques; however, some experimental observations have shown that bacterial flagellar motors are not necessarily symmetric [131]. To study the effects of the motor torques on the hydrodynamic behavior, we fix the sum $|T_1| + |T_2| = 2$ of absolute values for the two dimensionless torques about their respective axes and distribute the torques between the two motors with the ratio $R_T = |T_1|/|T_2|$. When less or equal torque is applied to the pusher flagellum ($R_T \leqslant 1$), our results indicate that both flagella exhibit stable twirling rotations, and the cell body moves normally on a double helical trajectory; see Fig. 4.9. A quantitative comparison of these cases in Tab. 4.6 indicates that the swimming characteristics are relatively insensitive to the motor torque ratio as it varies from 0.2 to 1. Increasing R_T to 2 causes the pusher flagellum to transition to the overwhirling state as the pusher motor torque exceeds a critical value. In this state, the flagellum is oriented almost perpendicular to the direction of swimming (Fig. 4.4), which means that rather than contributing propulsive thrust, it acts as a brake. Further increase of the torque ratio decreases the total propulsion and leads to a smaller average translational speed. Moreover, the pusher flagellum rotation frequency increases and so it completes each cycle of the overwhirling rotation in a shorter time period. This results in a higher number of small loops in the trajectory for $R_T = 5$

in comparison with the case $R_T = 2$ (see Fig. 4.9).

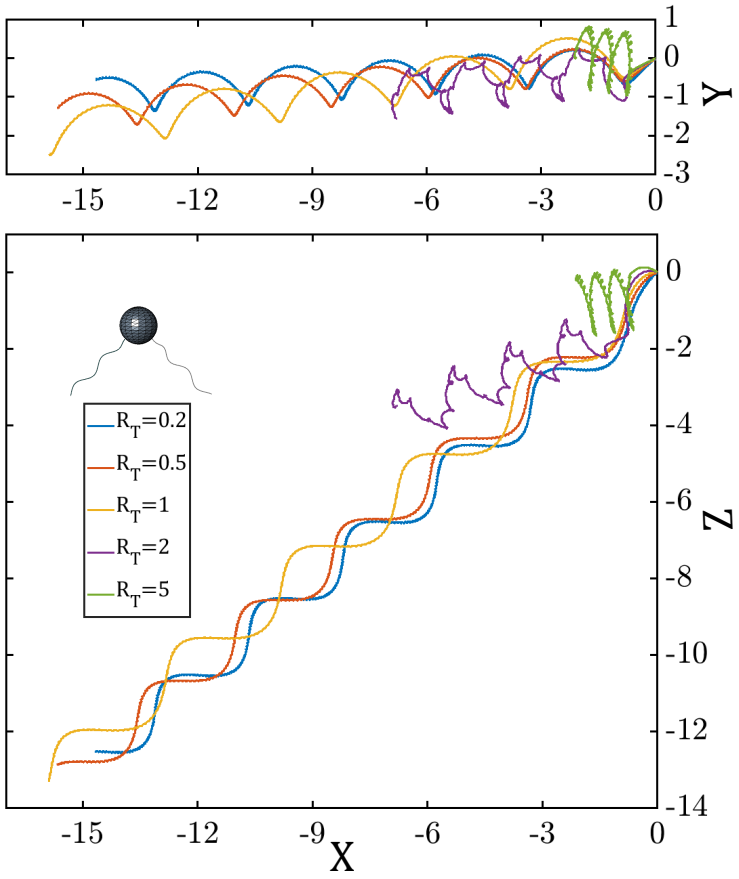

Figure 4.9: The swimming trajectory of the model bacterium projected on XY and XZ planes as a function of motor torque ratio R_T.

4.8 External magnetic field

Intracellular magnetosomes enable MTB to change their swimming direction in response to external magnetic fields. In particular, the external magnetic field applies torque to the magnetosome chain inside the cell body to align the magnetic moment with its direction. It means that the magnetic torque is continuously applied to the cell body as long as the magnetic moment is not perfectly aligned with the magnetic field. This feature of MTB enables us to guide them along the desired path. Assume that a magnetotactic bacterium

Table 4.6: Comparing the swimming features of the puller-pusher model bacterium in different motors torques ratio.

R_T	Pitch	Diameter	$\overline{U} \times 10^3$	$\overline{\Omega} \times 10^3$	$\hat{U} \times 10^3$
0.2	3.19	0.95	19.1	38.7	25.7
0.5	3.34	0.95	20.3	38.7	28.2
1.0	3.91	1.08	20.9	34.1	27.0
2.0	1.59	1.26	6.67	27.2	35.9
5.0	0.49	1.64	1.56	20.7	40.2

steadily swims under the effect of a magnetic field. If the direction of the magnetic field is suddenly reversed, the cell body experiences a large magnetic torque which tends to realign the magnetic torque with the new direction of the magnetic field. If the external magnetic field is strong enough, the cell body and so the swimming direction change in response to this external stimulus. Depending on the bacterium configuration and the orientation of the magnetic moment inside the cell body, the swimming directions might change 180°, and the bacterium performs a U-turn. The diameter of the U-turn strongly depends on the strength of the magnetic field and the bacteria's magnetic moment. This technique is practically used to measure the strength of the magnetic moments in the magnetotactic bacteria [76]. In this study, we assume that the magnetosomes are placed linearly in the direction of the propulsion axis ($\vec{e}_1^{(B)}$) in both pusher and pusher-pusher model bacteria. The bacteria are initially located at the origin and toward $-\vec{X}$ direction. By starting the simulation the external magnetic field is applied in $-\vec{X}$ direction for the first 1000 units of the time and then it is reversed. As expected, the cell body starts to turn after switching the field direction; depending on strength of the magnetic field, the time and the diameters of the U-turns differ in the studied cases.

As shown in Fig. 4.10 and Fig. 4.11, for strong magnetic fields, the model bacteria exhibit sharp turns which are not perfectly U-shaped, and there are some extra turns which are direct results of the flagella deformations. In fact, since the flagella are flexible, there is a time gap between the cell body reorientation and full reorientation of the flagella. Consequently, the complexity in the trajectories is due to the gradual changing of the propulsive force direction during the time gap.

Here, the diameters of the U-turns are obtained by measuring the perpendicular distances between two parallel arms of U trajectories. Our results show that the number of flagella is one of the main factors which impacts the U-turn diameter, especially under a weak magnetic field. Comparing the diameter of U-turns in uni- and biflagellated bacteria with almost symmetrical configurations (Fig. 4.12A) indicates that the diameter could

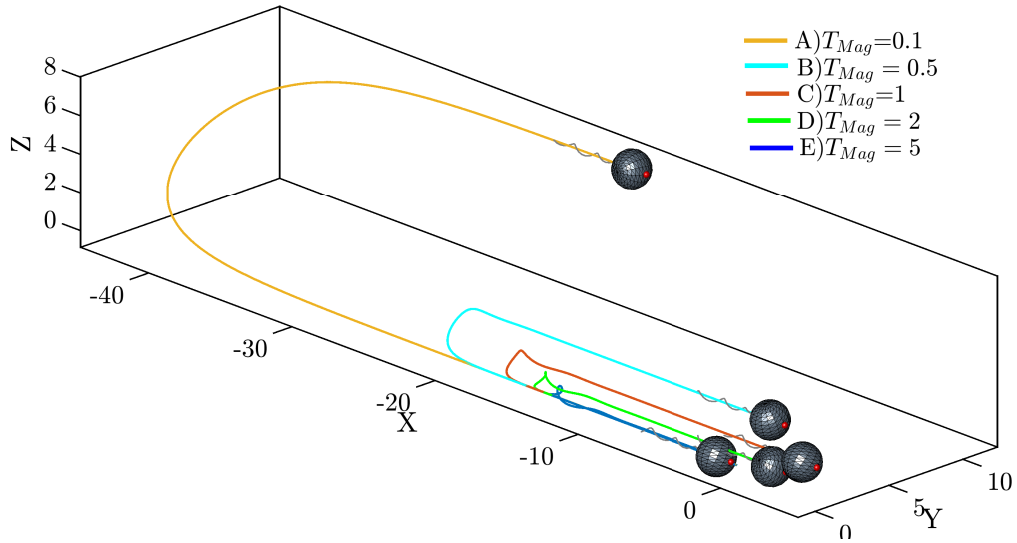

Figure 4.10: Uniflagellated model bacteria undergo U-turns in response to the reversal of external magnetic field. The magnetic moment direction which is fixed inside the cell body is marked by a red bubble. Initially, the red bubble and the external magnetic field are in $-\vec{X}$ direction. All other physical and geometrical parameters are stated in Tab. 4.1. The magnetic field is reversed at $T_s = 1000$. A)$T_{\text{Mag}} = 0.1$,$T_s = 6000$. B)$T_{\text{Mag}} = 0.5$,$T_s = 3500$. C)$T_{\text{Mag}} = 1$,$T_s = 3000$. D)$T_{\text{Mag}} = 2$,$T_s = 2500$. E)$T_{\text{Mag}} = 5$,$T_s = 2000$.

be twice larger in the pusher-pusher model bacterium. Under strong magnetic fields, the magnetic torque is dominant within the torques acting on the cell body, and therefore the bacteria swimming orientation and its variations are mainly dictated by the magnetic torque. As a result, the quick reversals of the stronger magnetic fields cause smaller U-turn diameters. In the pusher-pusher model bacterium, the hydrodynamic torque acting on the cell body and the total motors torques are both larger than the uniflagellated one, thus the magnetic torque is less dominant and reorientation of the swimmer takes longer time and leads onto a larger U-turn.

As we look at the relationships between the magnetic torque and the diameter of the U-turns in the log-log scale (Fig. 4.12B), we note a kind of power-law relationship between these parameters. In fact, the power of -1 relationship between these parameters is expected if we simplify the problem into the turning of a spherical particle in response to the reversal of a constant magnetic field. However, the complexity of the geometries and the deformations of the flagella slightly change the relationship. To visualize those changes, two lines representing the power of -1 relationships are sketched in Fig. 4.12. We

have sketched two distinct lines because the differences in the translational speed of the model bacteria with Pusher and Pusher-Pusher flagella modify the constant proportionality in the power-law relationships.

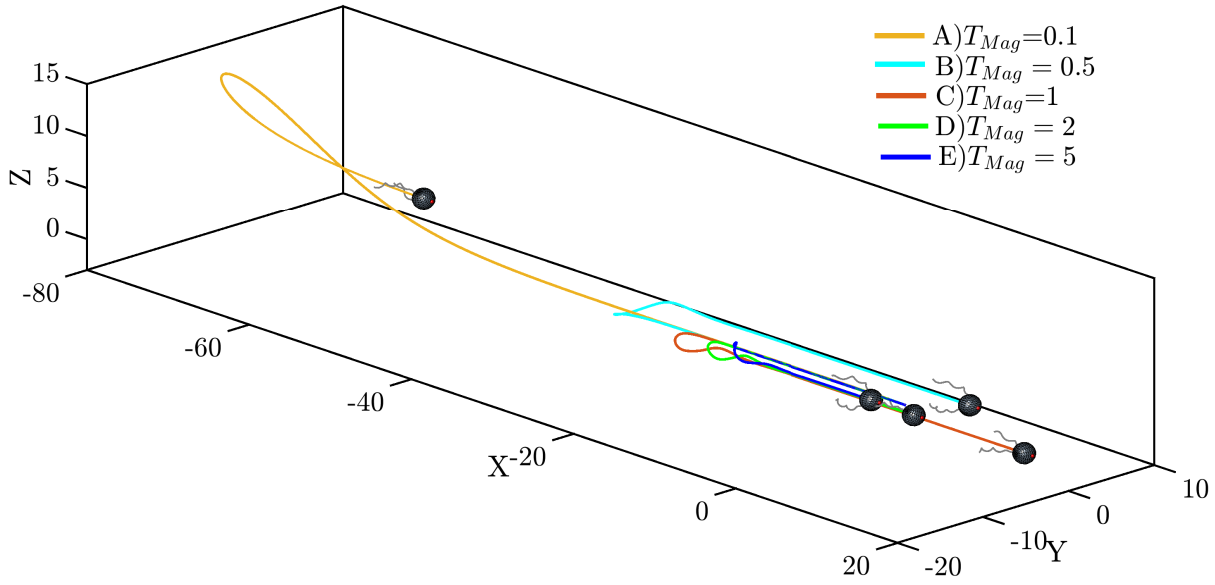

Figure 4.11: Pusher-pusher model bacteria undergo U-turns in response to the reversal of external magnetic field. The magnetic moment direction which is fixed inside the cell body is marked by a red bubble. Initially, the red bubble and the external magnetic field are in $-\vec{X}$ direction and all other physical and geometrical parameters are chosen from Tab. 4.1. The magnetic field is reversed at $T_s = 1000$. A)$T_{\text{Mag}} = 0.1$,$T_s = 6000$. B)$T_{\text{Mag}} = 0.5$,$T_s = 4000$. C)$T_{\text{Mag}} = 1$,$T_s = 3500$. D)$T_{\text{Mag}} = 2$,$T_s = 2500$. E)$T_{\text{Mag}} = 5$,$T_s = 2000$.

4.9 Summary and conclusion

The aim of this chapter is to model and analyze the motion of a bacterium with two flagella or flagellar bundles. Experimental observation of *M. marinus* locomotion and its double helical trajectory in unbounded fluid inspired us to focus on different aspects of such a motion, including a comparison between propulsion by two pusher flagella and by a pusher-puller combination. The results presented can be interpreted to understand the morphology of *M. marinus* as MTB and to design microrobots with specific characteristics.

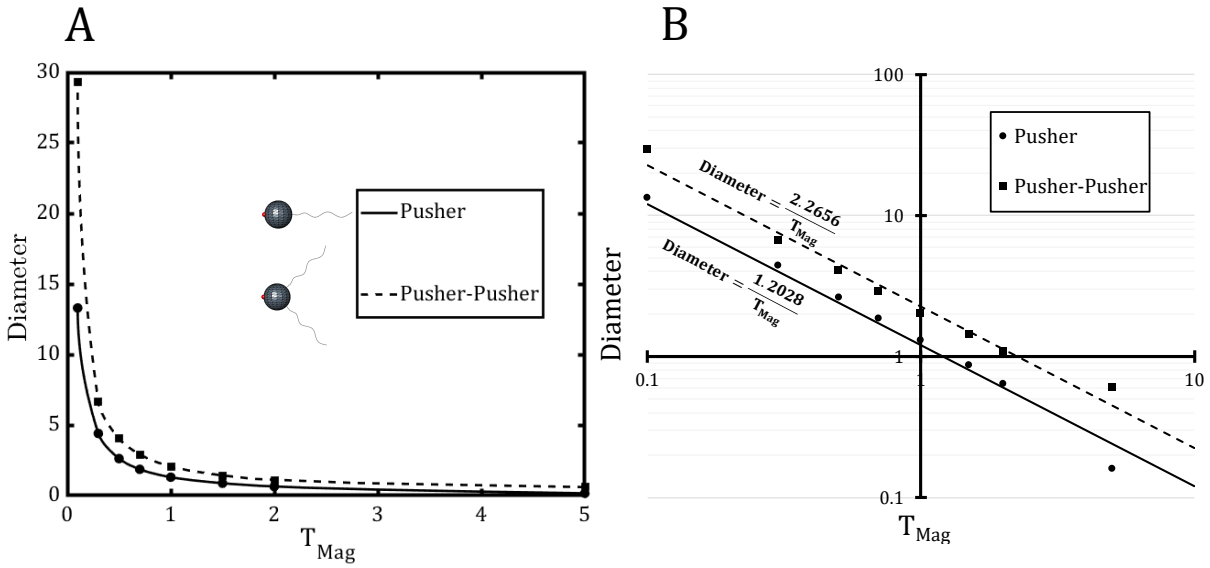

Figure 4.12: A) Diameter of U-turns that the pusher and pusher-pusher model bacteria undergo in response to the reversal of the external magnetic field. $T_{\text{Mag}} = ||\vec{B}|| \cdot ||\vec{M}_{\text{Mag}}||$ denotes the dimensionless maximum magnetic torque applied to the cell body in this plot. B) The relationship between the diameter of the U-turns and the maximum magnetic torque is shown in the log-log scale. The solid and dashed lines show the power of -1 relationships for comparison.

Furthermore, the presented scheme can be used to model the motion of other kinds of microorganisms in a viscous fluid.

We confirm that the model bacterium with one puller and one pusher flagella moves on a double helical trajectory in which the small helices are due to the revolutions of the flagella and the large helices are the result of the cell body rotation. The amplitudes and pitches of the small helices are smaller in our results than in those reported by Bente et al. [6]. The difference is likely due to the choice of flagellum shape, which we did not vary in our study. In practice, the size of the small helices changes if a different pitch, amplitude, and length are chosen for the flagellum. Apart from this, some quantitative discrepancy with experiments can be expected as we make simplifying assumptions about the morphology and swimming mechanisms of *M. marinus* in our model.

We have focused on reporting the diameter and pitch of the larger helix as well as the averaged translational and rotational speed, the instantaneous speed, and the swimming orientation. These swimming features are strongly dependent on the flagella position, ori-

entations and stiffness and are less sensitive to the ratio of motor torques. The motor torque ratio becomes important when it causes the pusher flagellum to enter the overwhirling state. In this state, the pusher flagellum exhibits large deformations and does not effectively propel the cell body. The result is lower translational speed and some sharp turns in the swimming trajectory. Decreasing the pusher flagellum stiffness below a critical value (in our study $k_F \leq 0.75$) can also put the pusher flagellum in the overwhirling state.

We note that the diameters and pitches of the helical trajectories increase with the parameters k_F, α, and β, whereas the averaged translational and rotational speeds vary inversely with these parameters.

In all the studied cases, the puller flagellum has better alignment with the swimming direction (Fig. 4.4) than the pusher flagellum and exhibits twirling rotation. One interpretation is that the generated thrust by the puller flagellum is more effectively used to propel the bacterium in the swimming direction. These results reveal the importance of the puller flagella in propelling the cell body and stabilizing the microorganism's locomotion.

In our simulations, the pitch and diameter of the large helices are closest to experimentally observed values when the flagella are stiff ($k_F \geq 3$) and the angles α and/or β are large specific ranges. We expect greater sensitivity to the β parameter when the stiffness is higher because, for low stiffnesses, the flagella tend to align with the swimming direction rather than maintaining the orientation defined by β. We note that $k_F = 3$ corresponds to a flexural rigidity approximately seven times as high as that of a single *E. coli* flagellum, which is reasonable given that the flagellar bundle of *M. marinus* contains seven flagella. Interestingly, the average swimming speed is maximized by having low stiffness (while still avoiding overwhirling) and small α, β, which are the opposite requirements from matching the observed large helical trajectories. This suggests that the locomotion of *M. marinus* is not optimized purely for average speed; the large amplitude helical motion could serve other purposes.

Experimental observations of helically swimming organisms indicate that they mainly orient the axis of the helical trajectory with the direction of the stimulus [38, 28]. It is hypothesized that moving on a helical trajectory could be a sampling strategy for some microorganisms. In particular, if there is a gradient in a background stimulus field, then this motion modulates the stimulus intensity encountered by the microswimmer and allows the microorganism to respond to the gradient. Investigation of the sampling mechanism in phototactic and chemotactic free-swimming microorganisms has shown that the properties of helical trajectory including its radius, pitch angle, etc., play an important role in detecting the chemical concentration gradient and the light direction [28].

Our results demonstrate that the properties of the helix are determined not only by

static geometric and material parameters but also by the motor torques, which can be adjusted dynamically to give time-dependent trajectory characteristics. Specifically, for lower motor torques [equivalent to higher relative stiffnesses of the flagella], the flagella do not deform enough to become aligned with the swimming direction, leading to helical motion with a larger radius. At higher motor torques, the flagella are better aligned and the trajectory becomes more linear. We note that this torque-dependent alignment is due to the arrangement of the puller and pusher flagella on the same side of the cell body ($\alpha, \beta \approx 45°$). Axisymmetric configurations ($\alpha, \beta \approx 0°$) would give rise to approximately linear trajectories and be less sensitive to changes in motor torque.

It would be interesting to determine experimentally whether *M. marinus* or similar bacteria exhibit helical trajectories that vary consistently with our simulations and whether these bacteria modulate their motor torques under different conditions. As an application to microrobotic swimmers, the simulation results suggest that the swimmer can switch between a fast, linear mode for ballistic motion and a slower, helical mode for sensing gradients.

Chapter 5

Locomotion of Multiflagellated Bacteria

5.1 Introduction

The peritrichous bacteria such as *Escherichia coli* and *Bacillus subtilis* induce locomotion through the use of multiple flagella anchored at random locations around the cell body. Similar to the uniflagellated and biflagellated bacteria, very flexible short hooks connect the flagella to the independent rotary motors. When all the flagellar motors rotate in a same direction, the observations have shown that the flagella tend to gather to form a single helix [7, 122]. This phenomenon, known as bundling of flagella, leads to the forward swimming of the bacteria. Any change in the rotation direction of at least one motor causes the bundle to unravel, and therefore the cell body starts to move in random directions. In fact, the peritrichous bacteria employ this movement, known as tumbling, between the forward movements, called "run" state, to stochastically change the swimming direction toward a more favorable environment [8].

Several studies have numerically investigated the flagellar bundling progress and discovered that the hydrodynamic interactions between the flexible helical flagella might induce the flagella to form a bundle. In previous studies, the specific roles of the hooks and the cell body in the flagellar bundling are neglected [37] or it is assumed that the flagellar filaments are rigid and only bending of the hooks leads to the flagellar bundling [124, 52, 92, 68]. Nguyen and Graham [80] investigated the possibility of the bundling formation in different ranges of flexibility for the hook and filament, and they did not examine the locomotion of the bacteria. One of the most comprehensive numerical studies exploring multiflagellated

bacteria behavior was conducted by Lee et al. [60]. They studied the impacts of the number and distribution of the flagella on the swimming properties of the multiflagellated bacteria in free space. Moreover, they mainly focused on the polymorphic transformations of the flagella and their effects on the tumbling behavior of multiflagellated bacteria.

In this chapter, we use our model to numerically study the locomotion of a multiflagellated bacterium in bounded and unbounded spaces. We examine how the physical parameters such as the flagella arrangement, rigidity, torsion, and curvature change the swimming properties of the bacteria. Moreover, we study the behavior of the bacteria near a planar surface to clarify which features of the bacteria are affected by the presence of the boundary. We compare these results with the experimental measurements to validate the obtained results and provide evidence to improve our understanding of the peritrichous bacteria morphology and behavior.

5.2 Geometric model and mechanical properties

Our model bacterium in this chapter is comprised of a spherocylindrical cell body and three flexible flagella distributed on the cell body surface. Since the physical properties of *E. coli* are well studied, our peritrichous model bacterium is described based on *E. coli*'s properties. Even though *E. coli* usually have 5-10 flagella we describe the model bacterium with only three flagella to reduce the computational cost. We assume that each flagellum complex includes a stiff pure helical filament and a very flexible short straight hook connecting the filament to a constant-torque motor. Like the uni- and biflagellated model bacteria, a global frame, a body-fixed frame, and three flagella-fixed frames are used to describe the configuration of the model bacterium, as displayed in Fig. 5.1. All flagella have identical physical and elastic properties and their initial and rest configurations are right-handed helices with centerlines given by

$$\vec{\Lambda}^{(\mathrm{i})}(\xi) = \vec{X}^{(\mathrm{i})} + (0.02l + \xi)\vec{e}_1^{(\mathrm{i})} + a\cos(\lambda\xi)\vec{e}_2^{(\mathrm{i})} + a\sin(\lambda\xi)\vec{e}_3^{(\mathrm{i})}, \tag{5.1}$$

where $i = 1, 2, 3$ is the index of the flagellum; $\lambda = 2\pi/p$ is the wavenumber; a, p are the helix amplitude and pitch, respectively.

The experimental measurements have shown that the cell body in *E. coli* is roughly spherocylindrical with a diameter 0.88 µm and a length 2.5 µm [30]. In this study, the radius of an equivalent sphere $\overline{R} = 0.68$ µm, which has the same volume as the cell body, is used to non-dimensionalize the lengths. In addition to the average radius, the stable motor torque in *E. coli* $T_{\mathrm{avg}} = 0.8\,\mathrm{pN\,\mu m}$ and the viscosity of pure water $\mu = 10^{-3}\,\mathrm{Pa\,s}$ are employed

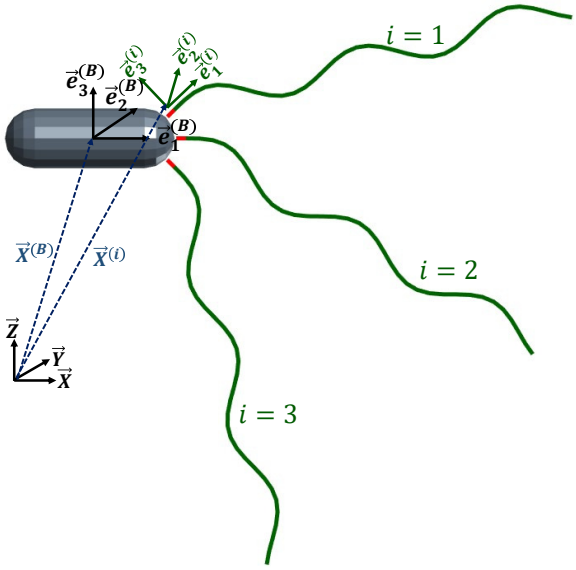

Figure 5.1: Schematic view of a model bacterium with three flagella. Several position vectors and local frames are used to define the configuration of the bacterium.

here to non-dimensionalize the other mechanical properties like the flagella/hook rigidity (Eq. 3.2), etc. The dimensionless physical and mechanical parameters used to describe the model bacterium in this chapter are specified in Tab. 5.1.

5.3 Flagella arrangement

It is traditionally assumed that the distribution of the flagella on the cell body surface is random in peritrichous bacteria. On the other hand, identifying the anchoring points and the arrangements of the flagella on the cell membrane is experimentally difficult [21]. For this reason, the role of the flagella arrangement on the flagella bundling and the swimming properties of the peritrichous bacteria is not experimentally well understood.

In order to elucidate the impacts of the flagella arrangement on the behavior of peritrichous bacteria, we compare the swimming properties of the model bacteria in three different arrangements named Star, Lateral, and Linear in this section. As displayed in Fig. 5.2, in Linear arrangement, all flagella perpendicularly protrude from one hemispherical end of the cell body. In Star arrangement, the flagella are radially connected to the end of the cylindrical part of the cell body. Furthermore, the angle between the anchoring points

Table 5.1: Physical and mechanical properties of the multiflagellated model bacterium.

Description	Symbol	Dimensionless	Dimensional
Cell body short radii	R_2, R_3	0.65	0.44 µm
Cell body long radius	R_1	$2.84R_2$	1.25 µm
Flagella/Hook diameter	d	0.15	0.10 µm
Flagella total length	l	10.4	7.07 µm
Flagella rest/initial pitch	p	3.33	2.26 µm
Flagella rest/initial amplitude	a	0.31	0.21 µm
Hook length	l_H	$0.02l$	0.14 µm
Flagellum relative stiffness	k_F	3	-
(Flexural rigidity)	$(EI)_F$	-	$(1.63\,\text{pN}\,\mu\text{m}^2)$
Hook relative stiffness	k_H	0.12	-
(Flexural rigidity)	$(EI)_H$	-	$(0.065\,\text{pN}\,\mu\text{m}^2)$
Motors Torques	T_1, T_2, T_3	1	0.8 pN µm
Repulsion strength of Lennard-Jones potential	F_s	0.1	0.12 pN
Cut-off distance of Lennard-Jones potential between the flagella	$2^{1/6}\sigma_F$	0.18	0.2 µm
Cut-off distance of Lennard-Jones potential between the wall and the cell body components	$2^{1/6}\sigma_W$	0.3	0.34 µm
Cut-off distance of Lennard-Jones potential between the cell body and the flagella	$2^{1/6}\sigma_H$	0.2	0.22 µm
Number of segments on filament	N_S	36	-
Number of segments on hook	N_H	2	-
Number of triangular elements on the cell body	N_B	264	-
Regularization parameter	ϵ_F	0.5d	0.05 µm
Fluid viscosity	μ	1	$0.001\,\text{Nsm}^{-2}$
Fine time step	Δt_fine	9×10^{-4}	3.58×10^{-7} s
Coarse time step	Δt_coarse	7.2×10^{-2}	2.86×10^{-5} s

(120°) in the Star arrangement is chosen in a way such that the vector sum of the motors' torques on the cell body is zero. Motivated by some observations in which the flagella in *E. coli* protrude from middle of the cell body [121], Lateral arrangement is taken into account. In this arrangement, a flagellum is radially connected to the middle of the cell body and two others are still on the hemispherical end.

By applying identical and unidirectional constant torque to the flagellar motors, the flagella start to rotate in a same direction. They eventually synchronize their rotation and finally form a flagellar bundle. As shown in Fig. 5.3, in the studied arrangements, all flagella get entangled in a single bundle behind the cell body. Typically, the flagellar

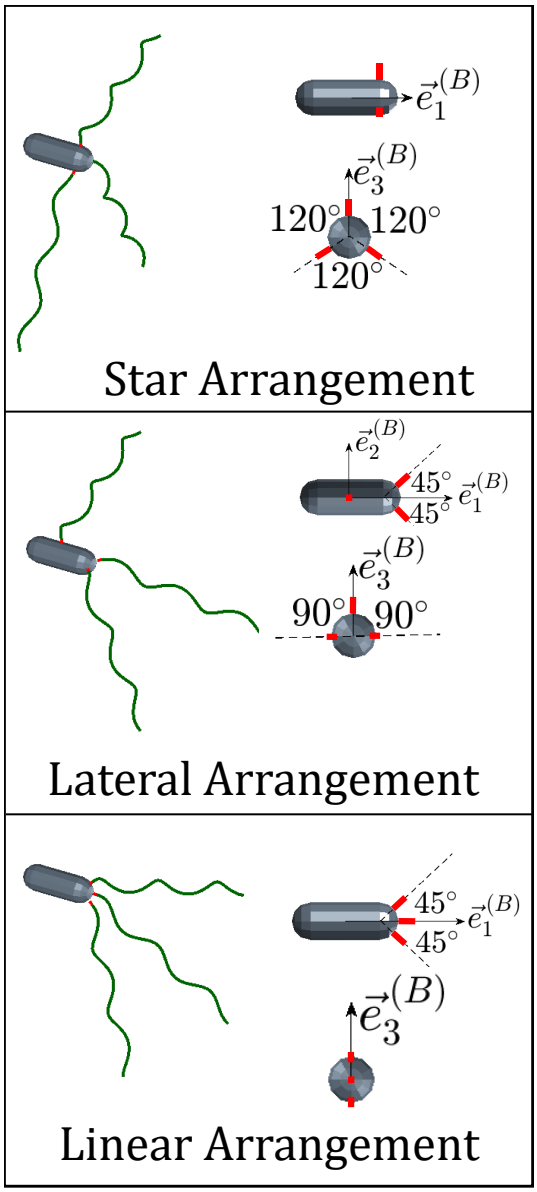

Figure 5.2: Three different arrangements of the flagella on the cell body are taken into account in this chapter to investigate their effects on the swimming properties of the peritrichous model bacteria. The anchoring points of the hooks on the cell body are displayed in two different views. In the top-right picture, the cell body is viewed from the side, and in the bottom-right picture, the cell body is viewed from the hemispherical end such that the direction $\vec{e}_1^{(B)}$ points toward the observer.

bundles align with the cell body's long axis, and the propulsion induced by the bundle is mainly applied in the direction of the cell body cylinder axis, similar to what we see in the Star and Lateral arrangements. However, if the stresses along the hooks surpass the buckling threshold, the hooks become unstable, and therefore the bundle forms a large angle ($> 90°$) with respect to the cell body cylinder axis. This kind of instability is observed in the Linear arrangement when the relative stiffness of the hooks is small, $k_H = 0.12$. For the larger stiffness of the hooks, the bundle is like in the other configurations (i.e. Star and Lateral).

In Fig. 5.4, the swimming trajectory of the bacteria in different flagellar arrangements and hooks' relative stiffness are compared. In the Linear arrangement with more flexible hooks, i.e. $k_H = 0.12$, the instability of the hooks causes the model bacterium to move on a double helical trajectory. In this state, the flagella bundle bends toward the cell body, and the steady angle between the bundle axis and the cell body's long axis becomes $\approx 100°$, as shown in the last row of Fig. 5.3. In the stiffer hooks, i.e. $k_H = 0.15$, the hooks remain stable and the bacterium swims on a relatively straight trajectory with the bundle trailing behind the cell body.

In Star arrangement, the model bacterium travels on a relatively straight trajectory, because the propulsion induced by the flagella is almost axisymmetric and the flagellar bundle effectively thrusts the cell body in the direction of the long axis. In the Lateral arrangement where one of the flagella protrudes from the side of the cell body cylinder, the propulsion is not perfectly in the direction of the cell body's major axis, hence the precession of the cell body's long axis around the swimming direction is observed. By changing the hooks' stiffness, no significant differences are observed in the trajectories of the bacteria with the Star and Lateral arrangements.

The swimming properties of the bacteria are quantitatively compared in Tab. 5.2. In this table, the average swimming speed ($\overline{U}$) and rotation speed ($\overline{\Omega}$) represent the norm of the average of the instantaneous translational and rotational velocity of the cell body over one complete cycle of the cell body rotation, respectively. In order to express the degree of bundling completion quantitatively, we define a bundling index as:

$$I_{\text{bundle}} = \frac{1}{3}\sum_{i=1}^{N_{\text{P}_\text{F}}} \min_j \left\{\left\|\vec{r}^{\,i(1)} - \vec{r}^{\,j(2)}\right\|\right\} + \min_j \left\{\left\|\vec{r}^{\,i(1)} - \vec{r}^{\,j(3)}\right\|\right\} + \min_j \left\{\left\|\vec{r}^{\,i(2)} - \vec{r}^{\,j(3)}\right\|\right\}, \quad (5.2)$$

where $\vec{r}^{\,i(m)}$ denotes the position vector of the ith evaluation point on the mth flagellum and each of the minima are over $j \in \{1, 2, ..., N_{\text{P}_\text{F}}\}$. In fact, the bundling index represents the average of the minimum pairwise distances between the evaluation points on the flagella. Based on this definition, the progress of the flagella bundling is complete as the

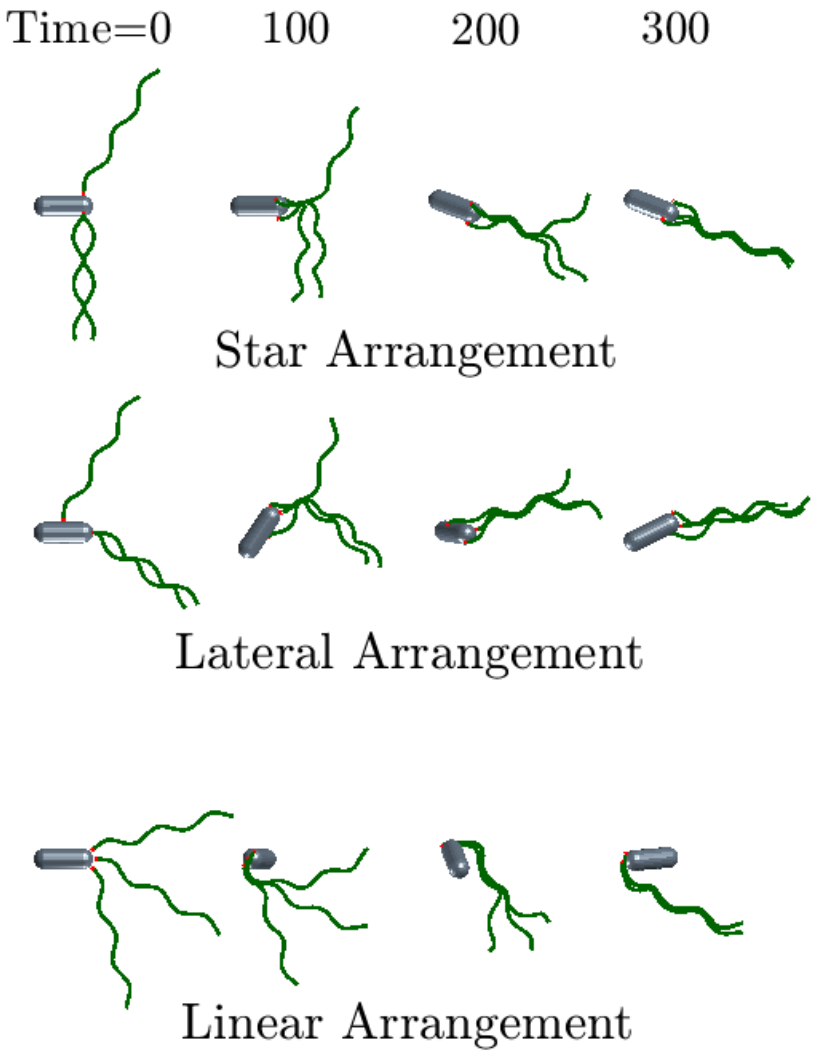

Figure 5.3: Bundle formation for cells with different flagellar arrangements. The propulsion induced by the flagella in the different directions causes the cell body to reorient at the beginning of the swimming. In the Star and the Lateral arrangements, a single bundle is formed at the rear whereas, in the Linear arrangement, the bundle bends around the cell body (due to the instability of the hooks) so that the base of the bundle is at the front of the body. The properties of the bacteria in these simulations are as stated in Tab. 5.1.

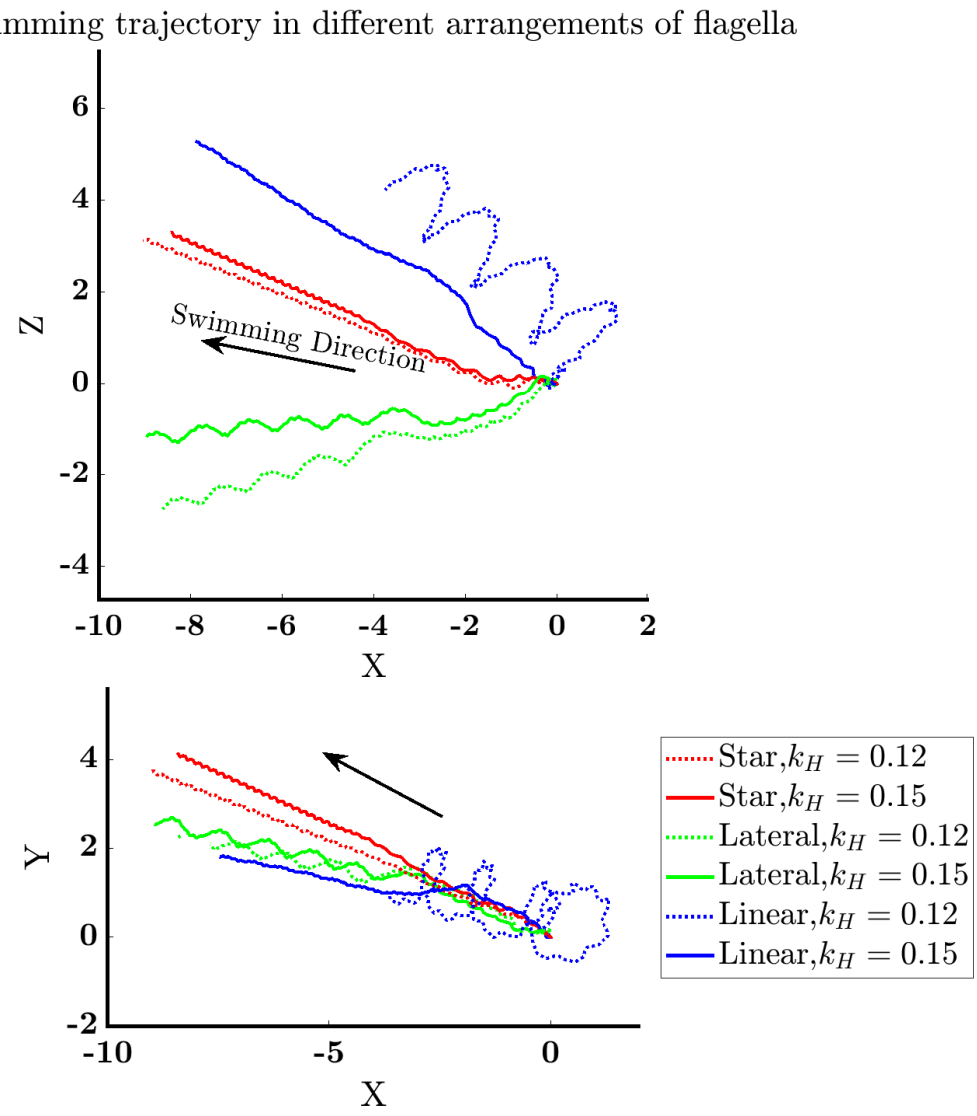

Figure 5.4: Swimming trajectories of the model bacteria with different flagellar arrangements and hook stiffnesses. The instability of the hook in the Linear arrangement and the lower stiffness of the hook causes the bacterium to move on a double helical trajectory. The physical properties of the model bacteria are described at Tab. 5.1. Dimensionless swimming time is $T_s = 700$ in these simulations.

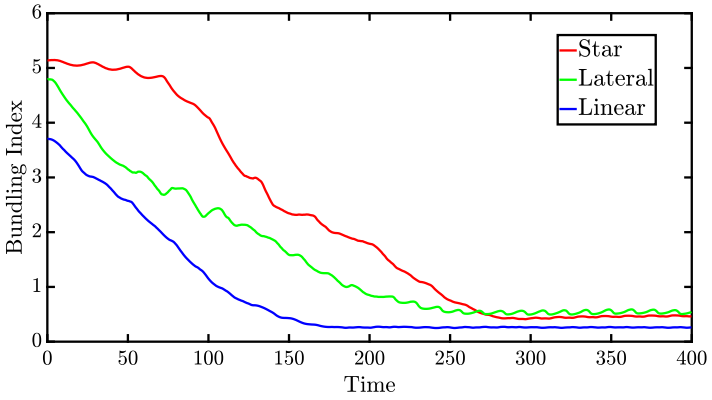

Figure 5.5: Variation of bundling index with respect to time in three different flagellar arrangements. During the flagellar bundling process, the average pairwise distances between the evaluation points on the flagella (named bundling index) decrease so that it reaches its minimum steady value as the single bundle forms.

bundling index reaches its minimum steady value. In this regard, the flagella bundling time (T_{Bundling}), denotes the dimensionless time from starting the rotation of the flagella until the bundling index becomes steady. As shown in Fig. 5.5, the bundling indices in all the studied arrangements are initially large and their values eventually decrease as the flagella get closer. Since the initial distances between the flagella are not identical in the studied arrangements (initial configurations are like Fig. 5.2), the bundling indices have different values at the beginning.

Disregarding the case in which the hooks become unstable (Linear arrangement with $k_H = 0.12$), our results indicate that the flagellar arrangements and the hooks' stiffness do not significantly affect the average swimming speeds of the bacteria. Unlike the swimming speed, the average rotation speed of the cell body is slightly affected by the flagellar arrangements, such that our results show that the cell body in the Linear arrangement rotates 40% faster than in the Lateral arrangement. Due to the fact that the cell body rotates in response to the motor torques, the position and orientation of the motors strongly affect the rotation speed of the cell body by changing the vector sum of the effective torques on the cell body. Since the motors in Linear arrangement point to a same side, the reactant torque on the cell body is higher than the other arrangements, and hence the cell body spins faster. Interestingly, despite the fact that the reactant torque on the cell body is initially zero in the Star arrangement, the cell body rotation rate in this arrangement is still comparable with the other cases. This means that the flagella deformations and their

entanglement in the bundle are responsible for the rotation of the cell body. As expected, the flagella bend together more easily in the lower stiffness of the hooks ($k_H = 0.12$), thus it takes a shorter time to form a single bundle. Comparing the bundling time for different hook stiffnesses in Tab. 5.2 sheds light on the importance of the hooks' stiffness in the bundling time.

Experimental measurements demonstrate that the average swimming speed of wild-type *E. coli* in a bulk fluid is about 14.1±8.0 µm/s (dimensionless value is 8.2±4.7) [75]. The obtained swimming speeds for all the studied cases in this chapter are within the measured range for *E. coli*. In this respect, Qu et al. measurements [92] show that the bundling time of the flagella in wild-type *E. coli* and in a Newtonian liquid with viscosity 0.001 Pa.s is about 0.09 -0.12 s (dimensionless value is 226-301). Our results, especially in the Star and Lateral arrangements, are in good agreement with these measurements.

Table 5.2: The steady-state swimming properties of the multiflagellated model bacteria in different flagellar arrangements.

Arrangement	k_H	$\overline{U} \times 10^3$	$\overline{\Omega} \times 10^3$	T_{Bundling}
Star	0.12	11.5	83.5	254
Star	0.15	11.3	76.2	288
Lateral	0.12	11.8	68.2	251
Lateral	0.15	11.8	68.7	260
Linear	0.12	9.2	29.8	312
Linear	0.15	12.7	107.3	173

5.4 Hook instability

In the previous section, we note that the flagellar hooks become unstable when their relative stiffness is $k_H = 0.12$ and the flagella have Linear arrangement. Interestingly, this instability is only observed in the Linear arrangement of the flagella. Motivated by this observation, we investigate the impacts of a single flagellum anchoring point on the stability of the hook. To achieve this aim, four different points are chosen on the spherocylindrical cell body to attach the flagellum. These points and the flagellum orientation are inspired by the multiflagellated model bacteria. We describe the flagellum in Positions A and B according to the positions and orientations of the two flagella in the Linear arrangement. The anchoring points in Position C and D are according to the position of one of the flagella in the Star and Lateral arrangements, respectively. By fixing the filament relative stiffness

at $k_F = 3$ and varying the hook relative stiffness from $k_H = 0.1, \cdots, 0.25$ with a step size of 0.01, the threshold for the instability of the hook is roughly obtained. The cell body and the flagellum sizes and also the motor torque on each flagellum are consistent with the multiflagellated model bacteria. In this section, the critical thresholds are obtained as the hook is discretized into two straight segments. Our investigations indicate that the thresholds well depend on discretization. As we refine the discretization of the hook, the critical threshold decreasingly converges to a specific stiffness. The decision about hook stability is made by looking into the variation of the filament bending angle. As shown in Fig. 5.7, the filament bending angle represents the angle between the rotor axis and a line that connects the two ends of the filament (flagellum excluding the hook). When the hook stiffness is below the buckling threshold, the bending angle of the filament eventually increases over time so that the filament gets into the steric repulsive distance from the cell body's surface. In this swimming mode, the model bacterium migrates on a double helical trajectory. In contrast, the bending angle of the filament gradually converges to a steady value (which is typically a small value because the filament tends to be aligned with the rotor axis) when the hook's stiffness is above the buckling threshold. The variation of the bending angle for Position A is displayed in Fig. 5.7, for example. Based on this graph, the hook is unstable at $k_H = 0.23$ and is stable at $k_H = 0.24$, and therefore the relative stiffness threshold is within $k_H \in (0.23, 0.24)$. Similarly, these intervals are obtained for Positions B, C, and D and reported in Tab. 5.3. Interestingly, these results show that the buckling threshold of the hook varies significantly with the flagellum anchoring point. In particular, the hook becomes unstable easier as it is placed closer to the cell body's end. It is worth mentioning that we do these simulations for the different initial phases of the flagellum motor and notice that the critical stiffness of the hook remains in an identical interval but the transition time from the beginning of the simulation until the flagellum touches the cell body surface is considerably different.

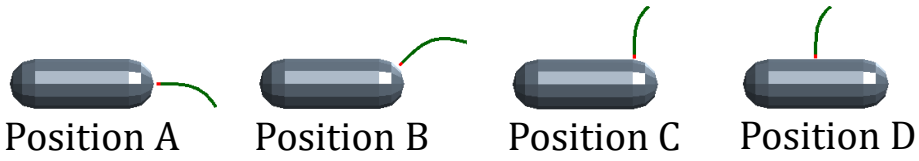

Figure 5.6: Four different anchoring points are chosen on the cell body surface to attach the single flagellum. These positions and the flagellum orientations are inspired by the flagella arrangement in the multiflagellated bacteria (i.e. Fig. 5.2). The cell body and the flagellum sizes are consistent with the multiflagellated model bacteria.

Comparing the critical values of the hook's stiffnesses in the uni- and multiflagellated

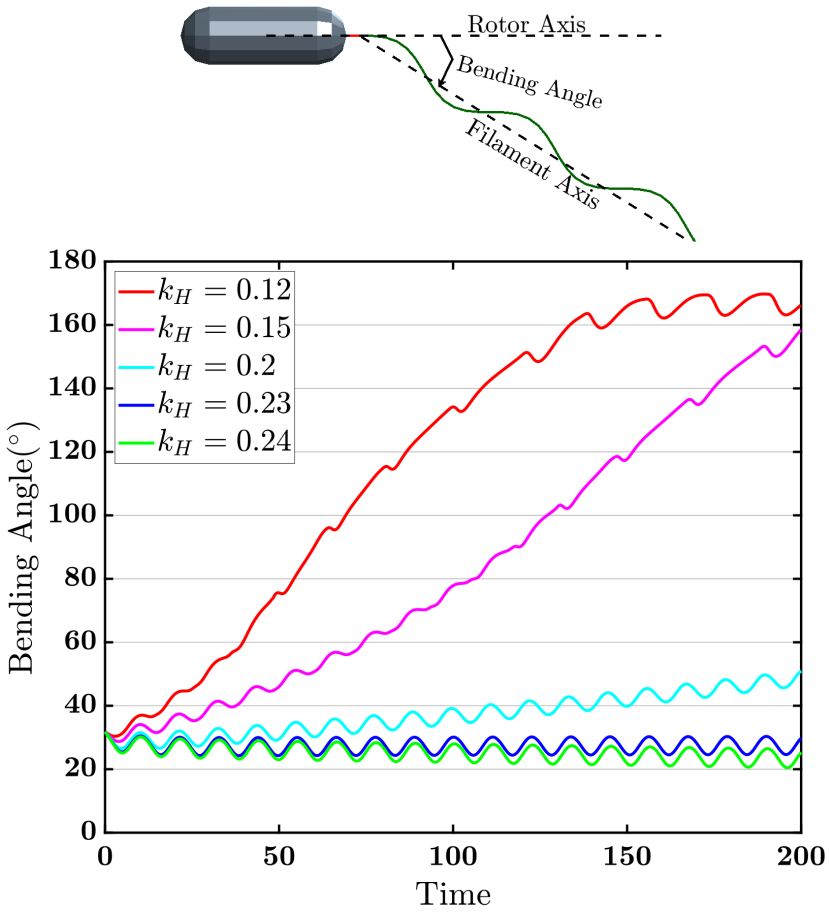

Figure 5.7: The variation of the bending angle of the filament in Position A. The bending angle of the filament represents the angle between the rotor axis and the line which connects the two ends of the filament. When the hook's relative stiffness is below the buckling threshold, the bending angle gradually increases. Decreasing of the bending angle means that the hook is stable in that specific relative stiffness.

bacteria demonstrate remarkable differences. For instance, the hook's critical stiffness in the Linear arrangement of the multiflagellated bacterium is within $k_H \in (0.14, 0.15)$ whereas it is within $k_H \in (0.23, 0.24)$ or $k_H \in (0.22, 0.23)$ in Positions A or B, respectively. Similar differences are observed between the Star arrangement and Position C and also between the Lateral arrangement and Position D. One interpretation is that the bundling effect in the multiflagellated bacteria directs the flagella toward a specific orientation and avoids the hooks bending more and getting a large angle with respect to the cell body's

main axis. For this reason, stable locomotion in the multiflagellated bacteria is achievable in the lower rigidity of the hook in comparison with the uniflagellated bacteria. This conclusion likely explains why the hooks' rigidity in the multiflagellated bacteria is mainly smaller than in the uniflagellated bacteria.

In the model bacterium with the Linear arrangement and $k_H = 0.12$, the hooks' relative stiffnesses in all the anchoring points are sufficiently small in comparison with the buckling threshold and therefore the flagella bundle bends toward a direction that is roughly perpendicular to the plane passing through the three anchoring points.

Table 5.3: The hook's buckling thresholds in four different anchoring points of the flagellum on the cell body. The hook is unstable in the lower bound of each interval and is stable in the upper bound.

Position	A	B	C	D
$k_{\text{H,critical}} \in$	(0.23,0.24)	(0.22,0.23)	(0.15,0.16)	(0.15,0.16)

5.5 Flagellar filament curvature and torsion

During the bundling process, the rotating helical flagella come close and synchronize due to the hydrodynamic interactions. For this reason, it is expected that the properties of the flagellar filaments in peritrichous bacteria affect the flagellar bundling process by changing the flow regime around the bacteria, and also the rotation rate of the cell body. The cell body rotation rate plays an important role in this respect because its counter-rotation speeds up the bundle formation. In this section, the influences of the flagellar filament's curvature (κ_F) and torsion (τ_F) on the bundling time, and the swimming properties of a multiflagellated model bacterium with the Star arrangement are investigated.

By fixing τ_F=0.3 and varying κ_F from 0.01 to 0.08, we note that the average swimming speed of the model bacterium becomes maximum as $\kappa_F \approx$0.02, disregarding the fact that the flagella in this curvature rotate slower than κ_F=0.01 (see Figs. 5.8A, C). Comparing the rotation rate of the flagella in Fig. 5.8C indicates that the flagella rotation rate strictly decreases with increasing κ_F. Even though it is expected that the bundling time of the flagella becomes longer in lower rotation rates of the cell body, the obtained results do not show an inverse correlation between the cell body rotation rate and the bundling time in the different curvatures. This means that the role of the flagellum curvature in the bundling time is more significant than the cell body's rotation rate (compare Figs. 5.8B, D).

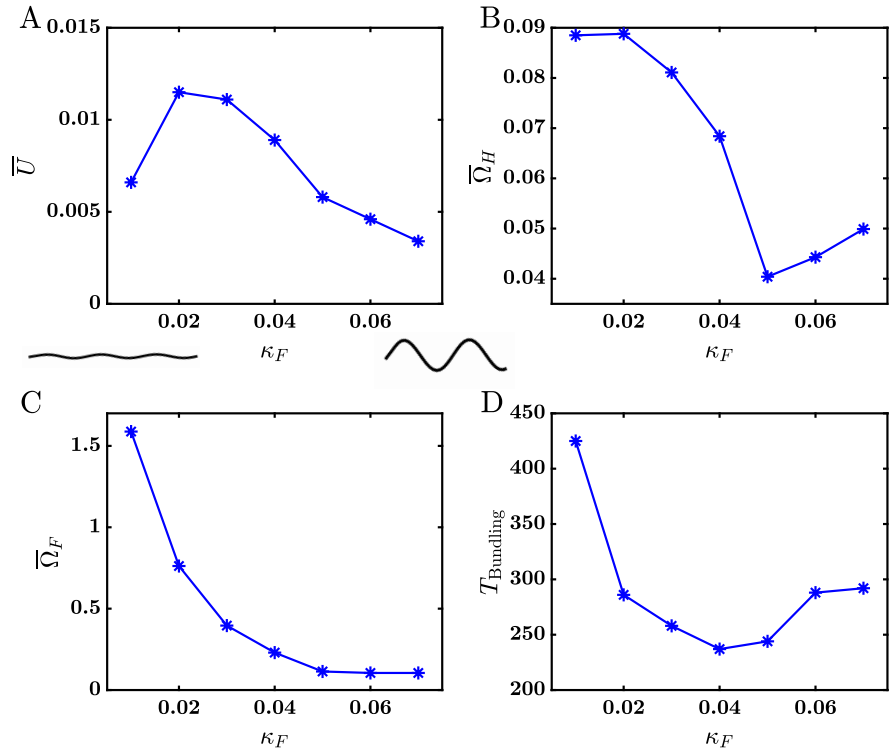

Figure 5.8: The steady-state swimming properties of the multiflagellated model bacteria with Star arrangement and different curvatures of the flagella helix (κ_F) and a constant torsion τ_F=0.3. The other parameters are as stated in Tab. 5.1.

We investigate the effects of the filament torsion on the model bacterium behavior in free space by fixing κ_F=0.03 and varying the torsion from 0.15 to 0.45. Like the curvature effect, there is an optimum value, τ_F=0.35, for the filament torsion to maximize the swimming speed. As presented in Figs. 5.9 C, D, the flagella rotation rate and the bundling time strictly decrease with the filaments torsion. In this respect, the angular speed of the cell body, which rotates to balance the motors' torques, becomes minimum when the torsion is about 0.25.

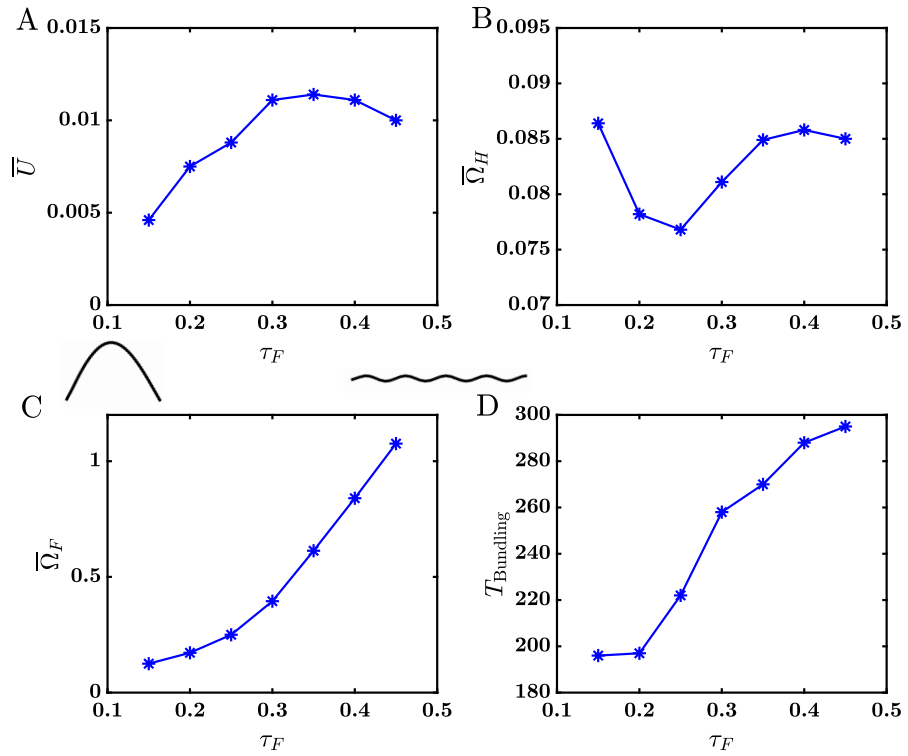

Figure 5.9: The steady-state swimming properties of the multiflagellated model bacteria with the Star arrangement and different torsion of the flagella helix (τ_F) and constant curvature κ_F=0.03. The other parameters are as stated in Tab. 5.1.

5.6 Flagella and hooks stiffnesses

In our original model bacteria, we assume that the flagellar filaments and the loaded hooks' stiffnesses are $k_F = 3$ and $k_H = 0.12$, respectively. In this section, we specifically study the effects of these stiffnesses on the swimming features of multiflagellated bacteria. To achieve this aim, we fix the hooks' stiffness at $k_H = 0.12$ and vary the filaments' stiffnesses from 2 to 5 in the Star arrangement of the flagella. Interestingly, our results show that the average swimming speed of the model bacterium slightly increases with the stiffness of the filaments (Fig. 5.10A), in the uniflagellated model bacterium we see that the swimming speed is almost insensitive to the filament's stiffness as a constant torque is applied by the motor (see Fig. 3.2). This difference between the uni- and multiflagellated bacteria is

probably related to the bundle structure and relatively larger deformations of the filaments in the multiflagellated bacteria. Our results demonstrate that in the small relative stiffness of the filaments, i.e. k_F=2, the rotation speeds of the cell body and the flagellar bundle are minimum. The longer bundling time in this stiffness is likely due to the low rotation speed of the cell body.

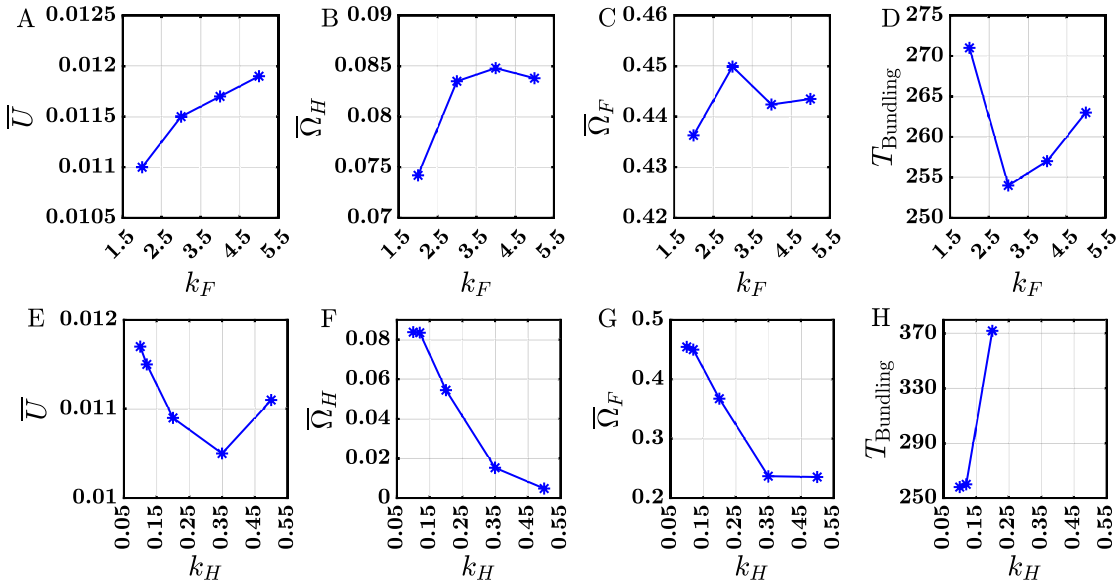

Figure 5.10: The steady-state swimming properties of the multiflagellated model bacteria with the Star arrangement in the different stiffnesses of the flagellar filaments and hooks. The physical parameters excluding the stiffnesses are described at Tab. 5.1.

Fixing the filaments' stiffness at $k_F = 3$ and varying the hooks' stiffness from 0.1 to 0.5, significantly change the swimming features. The obtained results indicate that the bacterium swims faster as the hook is more flexible and stable. The average rotation speeds of the cell body and the flagella bundle strictly decrease with the hooks' stiffness. By increasing the stiffness, the hooks resist bending which is induced by the bundling effects of the flagella, and hence the bundling time rises sharply. In higher stiffnesses $k_H \geq$0.35, the hooks resistance prevents the flagella to get closer and form a single bundle. For this reason, the bundling time is not reported for the higher stiffnesses of the hooks in Fig. 5.10H.

5.7 Reversal of a motor

Recalling that reversing the rotation direction of at least one motor causes the flagella bundle to unravel, we numerically explore its impact on the locomotion of multiflagellated bacteria. Even though several experimental observations have shown that the reversed flagellum executes polymorphic transformation and its rest configuration changes to semi-coiled [124, 57, 35] during the tumbling event, we disregard such a transformation in this section. In particular, we assume that the flagellum rest configuration remains a right-handed helix during the motor reversals. As shown in Fig. 5.11, during the bundling progress and the "run" state $t \in [0\ 400]$, the flagella bundle together and propel the cell body forward. At t=400, one flagellar motor switches the direction and applies an identical torque, but in the opposite direction, to the flagellum marked with the purple color. The viscous forces normal to the axes of the flagellum push it to move apart and unravel. Sudden variation in the torque associated with this process reorients the cell. The bundling index, which represents the average distances between the flagella, increases after the reversal of the motor (see Fig. 5.11C). The motor applies the opposite constant torque to the flagellum for 60 units of time and then comes back to its original direction at t=460. The flagella get closer again and rebuild the single bundle. Interestingly, the bundle forms on the other side of the cell body after the reversal of the motor when the bacterium has the Star arrangement of the flagella. In this mode, called the second mode, the flagella wrap around the spherocylindrical cell body and the base of the bundle is at the front of the body. Unlike the first mode in which the bundle axis is roughly aligned with the cell body's long axis, these axes are not aligned in the second mode. Since the stable configuration of the model bacterium in the second mode is no longer axisymmetric, the swimming trajectory is double helical. The swimming trajectories of the model bacteria during the "bundle-run-reversal-run" states are displayed in Fig. 5.11B.

Our interpretation is that more than one stable swimming mode is possible in multiflagellated bacteria with a spherocylindrical cell body when most of the flagella perpendicularly protrude from the cylindrical part of the cell body. In such an arrangement, since the rest configuration of the flagella is not biased toward one end of the cell body, the bundle may form in any orientation with respect to the cell body. In fact, the initial positions and orientations of the flagella dictate the stable orientation of the flagellar bundle with respect to the cell body.

Comparing the bundling index before and after the reversal of the motor in the Star arrangement indicates that the steady gap between the flagella is slightly larger in the second mode. Furthermore, a quantitative comparison of the swimming properties reveals that the average translational and rotational speed of the bacterium and the rotation

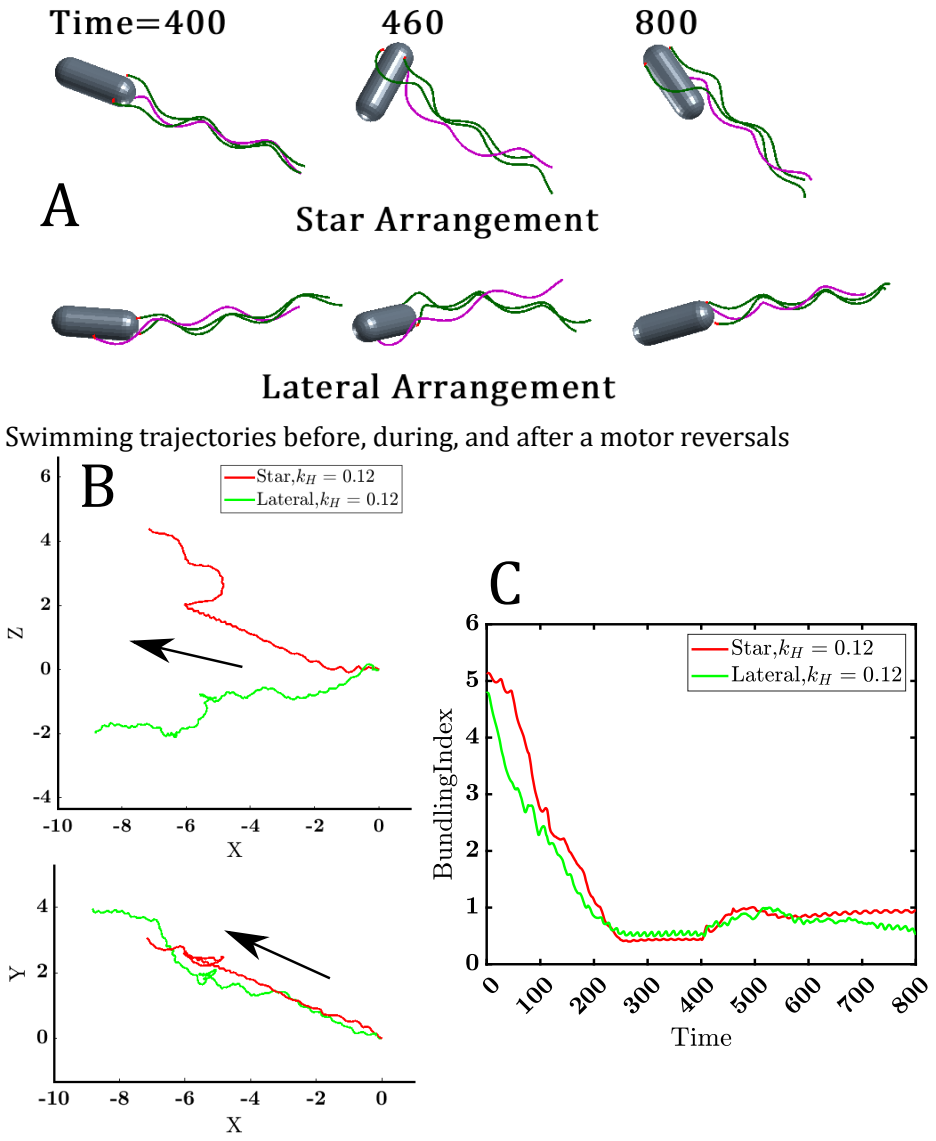

Figure 5.11: A) The flagellar bundle unravels after switching the rotation direction of one flagellum (marked with purple color) to $\vec{e}_1^{(1)}$ direction for 60 units of time starting from t =400. The single bundle forms again, after all the flagella rotate in the same direction [i.e. $-\vec{e}_1^{(i)}$] starting at t =460. B) Swimming trajectories of the model bacteria with the Star and Lateral arrangements on XZ and XY planes before, during, and after the motor reversals. C) Bundling index of the flagella during the bundling, before and after the motor reversals.

Table 5.4: Swimming properties of multiflagellated model bacterium with Star arrangement before and after the reversal of one of the three motors. The physical properties of the model bacterium are described in Tab. 5.1.

Status	$\overline{U} \times 10^3$	$\overline{\Omega}_H \times 10^3$	$\overline{\Omega}_F \times 10^3$
First mode (before reversal)	11.5	83.5	450
Second mode (after reversal)	10.2	40.7	320

speed of the flagellar bundle all are lower in the second mode, as reported in Tab. 5.4. Our simulation in the higher stiffness of the hook, i.e. $k_H = 0.15$, shows that the model bacterium with Star arrangement is still transformed from the first mode to the second one after the motor reversals. The major difference appears in the orientation of the flagellar bundle in the second mode. In particular, the angle between the bundle axis and the long axis of the cell body is smaller in the higher stiffness and the bacterium configuration is more axisymmetric than k_H=0.12.

In the lateral arrangement, the configuration of the model bacterium is identical before and after the reversal of the motor. Comparing the swimming trajectory and the bundling index in Fig. 5.11, confirm that the configuration is identical. However, the obtained results show that the forward swimming orientation of the model bacterium slightly changes after the reversal of the motor.

5.8 Flagella bundling near a wall

Experimental measurements indicate that peritrichous bacteria exhibit slightly different behavior near the surfaces and inside confined channels in terms of the tumbling probability, duration of forward swimming, swimming speed [75] etc. Motivated by these observations, we look into the bundle formation of the flagella when the model bacterium escapes from or swims toward a planar wall in this section. As shown in Fig. 5.12, two different arrangements of flagella (Star/Lateral) are chosen for the model bacteria to compare the behavior. The model bacteria are initially placed at a medium distance from the surface to avoid any collisions between the bacteria components and the surface. For this reason, it is expected that the effects of the boundary on the swimming properties of the bacteria are small. By comparing the bundling indices (Fig. 5.12E, F), we note that the bundling progress near the surfaces is almost similar to the free space. However, the results show that the bundling time is slightly longer near the surfaces. In fact, viscous torque due to the presence of a no-slip boundary causes the cell body to spin slower, and therefore

the advantage of the cell body counter rotation in bundle formation is less effective near the surfaces. As displayed in Fig. 5.12F, the bundling index slightly increases after the formation of the bundle as the bacterium approaches the surface. This variation is due to the tilting of the cell body in contact with the surface. In particular, the titling of the cell body causes the Lateral flagellum (protruding from the middle of the cylindrical part) gets away from the main bundle, and hence it increases the average distance between the filaments.

5.9 Swimming properties near a wall

Previous experimental measurements have shown that the swimming speed of *E. coli* near a surface is 9% higher than its speed in a bulk fluid [75]. The increase in the swimming speed is likely due to the variation of the shear forces near the surfaces. The presence of a no-slip boundary increases the drag forces and torques on the cell body; on the other hand, it improves the propulsion generated by the flagella. For these reasons, it is expected that the physical properties of the bacteria such as cell body size, flagella length, flagella arrangement, etc. have consequential effects on the forward swimming and rotational speeds of the bacteria near the surfaces. In this section, we aim to explore the effect of the flagella arrangement on the variation of the forward swimming and rotational speeds of the bacteria as they swim at different distances from a surface. As displayed in Fig. 5.13A, the model bacteria with Star and Lateral arrangements are initially placed parallel to the surface such that the distance between the cell body's long axis and the surface is H_0. We are interested to obtain the swimming properties in "run" state, so we use the steady configurations of the bacteria in the bulk fluid as the initial condition.

Fig. 5.13B represents the variation of the average swimming speed in $\vec{X}$ direction ($\overline{U}_X$) with respect to the initial distance from the surface H_0. $\overline{U}_X$ is calculated as the average of x component of the instantaneous velocity vector over one complete rotation of the cell body. After a short transition period, we calculate the properties before having a significant change in the distance from the surface. Like the free space, the model bacterium with Lateral arrangement swims faster than Star one as it is close to the surface ($H_0 \leq 4$), and its maximum speed in $\vec{X}$ direction is up by 7% than its speed in the bulk fluid. The results indicate that the swimming speed of the model bacterium with Lateral arrangement strictly decreases with the distance from the surface. One interpretation is that improvement in the propulsion generated by the flagella is more than the increment in the drag forces on the cell body near the surface. Since the cell body in the Lateral arrangement continuously tilts up and down, the variation in the hydrodynamic forces is not as straightforward as the

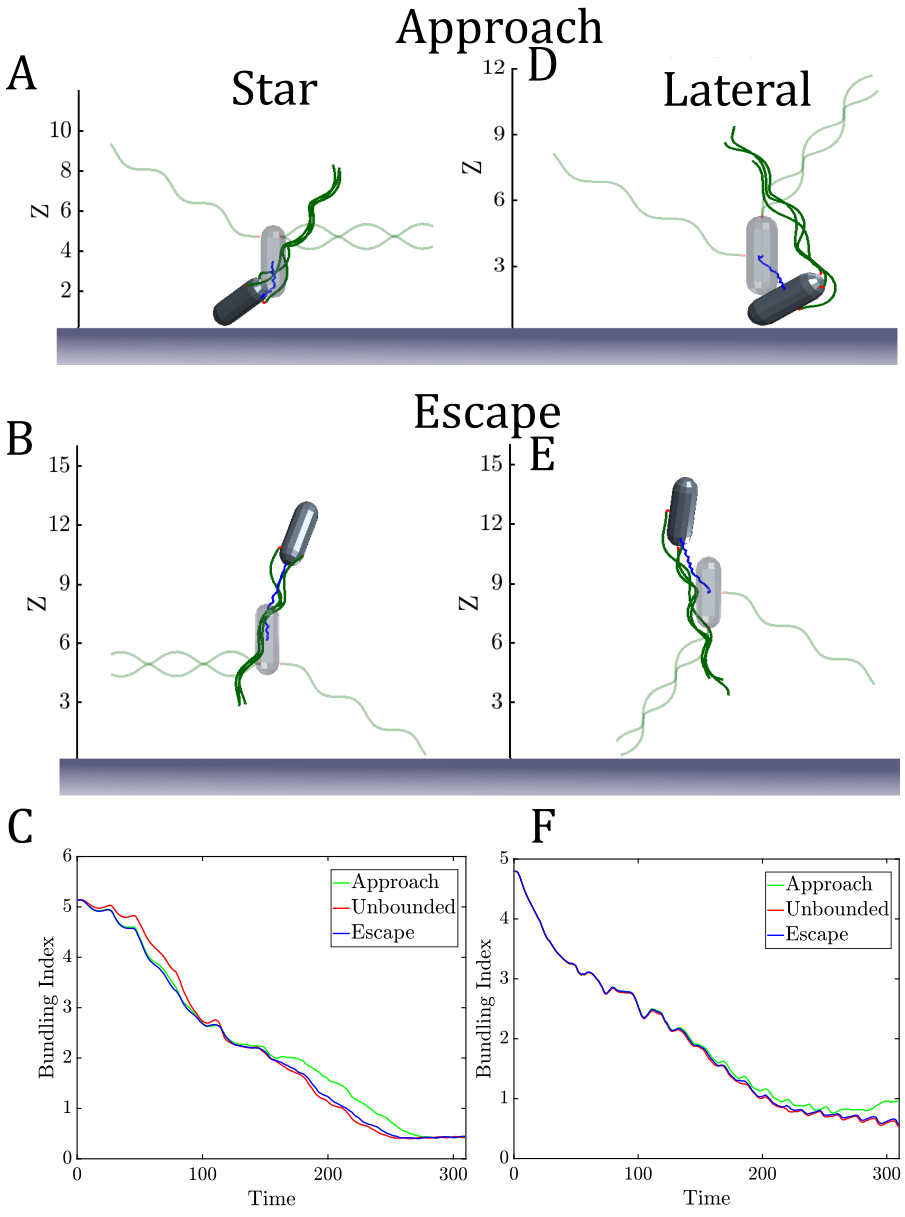

Figure 5.12: Bundling of flagella as the model bacterium vertically escapes or approaches to the wall. The results in the left and right columns are respectively for the Star and Lateral arrangements. The transparent model bacterium displays the initial position and configuration. The physical properties of the model bacteria are stated in Tab. 5.1.

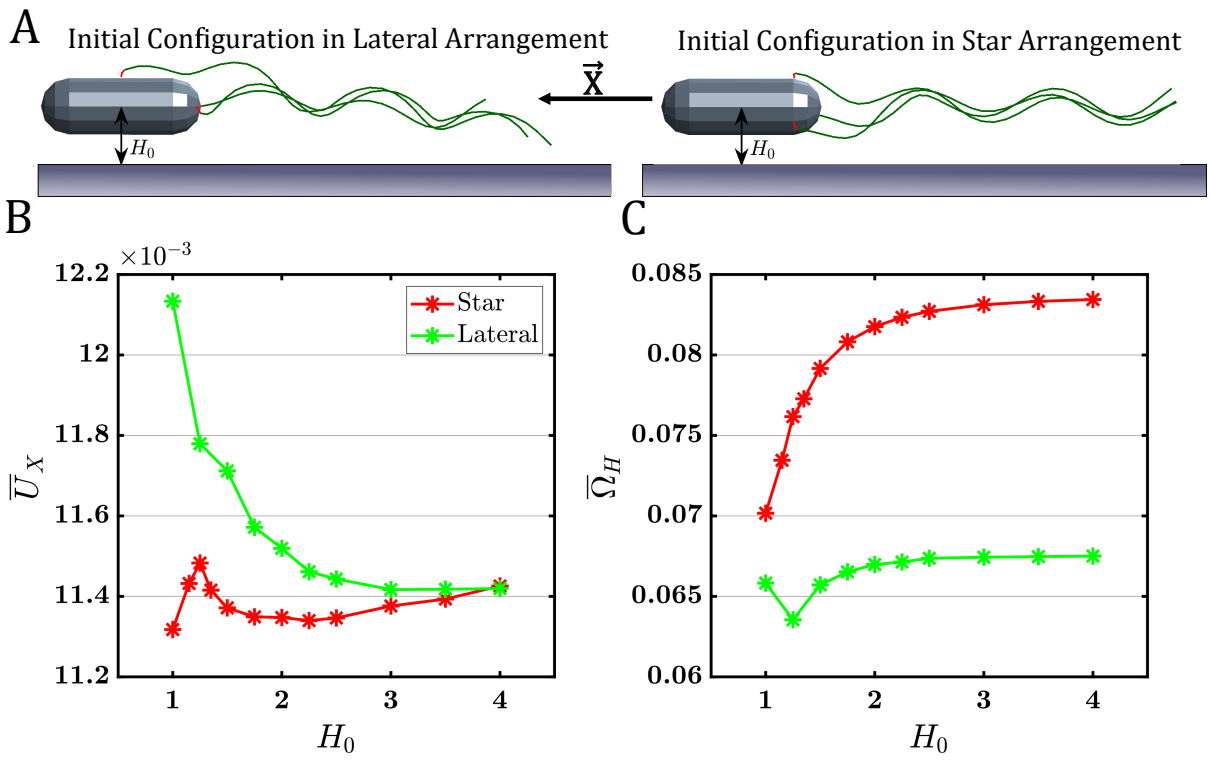

Figure 5.13: A) Initial configurations of the model bacteria with the Star and Lateral arrangements. Other simulation and physical parameters are chosen according to Tab. 5.1. B) Variation of the average swimming speed in $\vec{X}$ direction with respect to the initial distance from the surface. C) Variation of the average rotational speed of the cell body with respect to the initial distance from the surface.

bacteria with a simpler swimming pattern. In the Star arrangement, the variation in the swimming speed is not as large as in the Lateral arrangement. However, high drag forces on the cell body cause the bacterium to reach its minimum swimming speed as H_0=1. A slight increase in the distance from the surface (from H_0=1 to H_0=1.25) results in a considerable enhancement in the swimming speed.

The average rotational speed of the cell body $\overline{\Omega}_H$ denotes the norm of the average of the instantaneous angular velocity vector over one complete rotation of the cell body. The increase in the rotational speed with the distance from the surface nicely represents the decrease in the viscous shear torque applied to the cell body (Fig. 5.13). Since the motors apply constant torque to the cell body, the total torque on the cell body is almost constant, if we ignore the elastic bending moments transmitted from the flagella to the body. For

this reason, such a smooth increase in the rotational speed of the cell body is obtained. A relatively large rotational speed in the Lateral arrangement at H_0=1 is likely the result of the elastic bending moments. In both arrangements, the rotational speeds approach to their values in the bulk fluid, reported in Tab. 5.2.

5.10 Swimming trajectories near a wall

It has experimentally verified that some kinds of multiflagellated bacteria such as *E. coli* exhibit circular trajectories in interaction with the planar surfaces. Unlike the uniflagellated bacteria, the tendency of the multiflagellated bacteria to swim close to the surfaces is not well examined. As shown in Fig. 5.14, the model bacteria with Star and lateral arrangements migrate on circular arcs as they interact with the wall. Our results show that all the studied model bacteria have a strong tendency to remain close to the surfaces. The obtained trajectories in this study are not long enough to conclude whether the bacteria are fully entrapped by the surface or not, but according to the maximum escaping angle which is $\alpha_e < 1°$, the chance of entrapment in all the cases is evaluated very high. The results show the radii of the circular arcs in the model bacteria with the Star arrangement are slightly smaller than the Lateral arrangement. Since the model bacterium with the star arrangement has smaller translational and larger rotational speeds than the Lateral arrangement (see Fig. 5.13), it turns more at a unit length of the swimming path. Recall the discussion in section 3.4.3, the bacteria with more flexible hooks exhibit smaller circular trajectories. Whereas experimental observations of *E. coli* locomotion along the surfaces have shown that the cell body slightly points toward the surface (nose down) [2, 10, 11], numerical simulations of uniflagellated bacterial locomotion with a rigid flagellum have indicated that the cell body tilts toward the bulk fluid (nose up) to balance the torques on the cell body [109]. One of the aims of this chapter is to look into this inconsistency that exists between the numerical and experimental results. To do this, we quantify the orientation of the cell body with respect to the planar surface by calculating the angle $\alpha_{\text{Orientation}} = 90° - \langle \vec{e}_1^{(B)}, \vec{e}_Z \rangle$. The variation of this angle is shown in Fig. 5.15 when the model bacteria swim near a wall. In this graph, the positive value for $\alpha_{\text{Orientation}}$ means that the cell body points up (toward the bulk fluid) and the negative value corresponds to the cell body which points down. In the Lateral arrangement, the cell body continuously tilts toward the bulk fluid and the wall; for this reason, $\alpha_{\text{Orientation}}$ oscillates between the negative and positive values. However, the time averaging of the angles in all the studied cases (Lateral/Star) is positive; it means that the model bacteria with flexible hook and flagella, and either Star or Lateral flagellar arrangement generally point toward the bulk

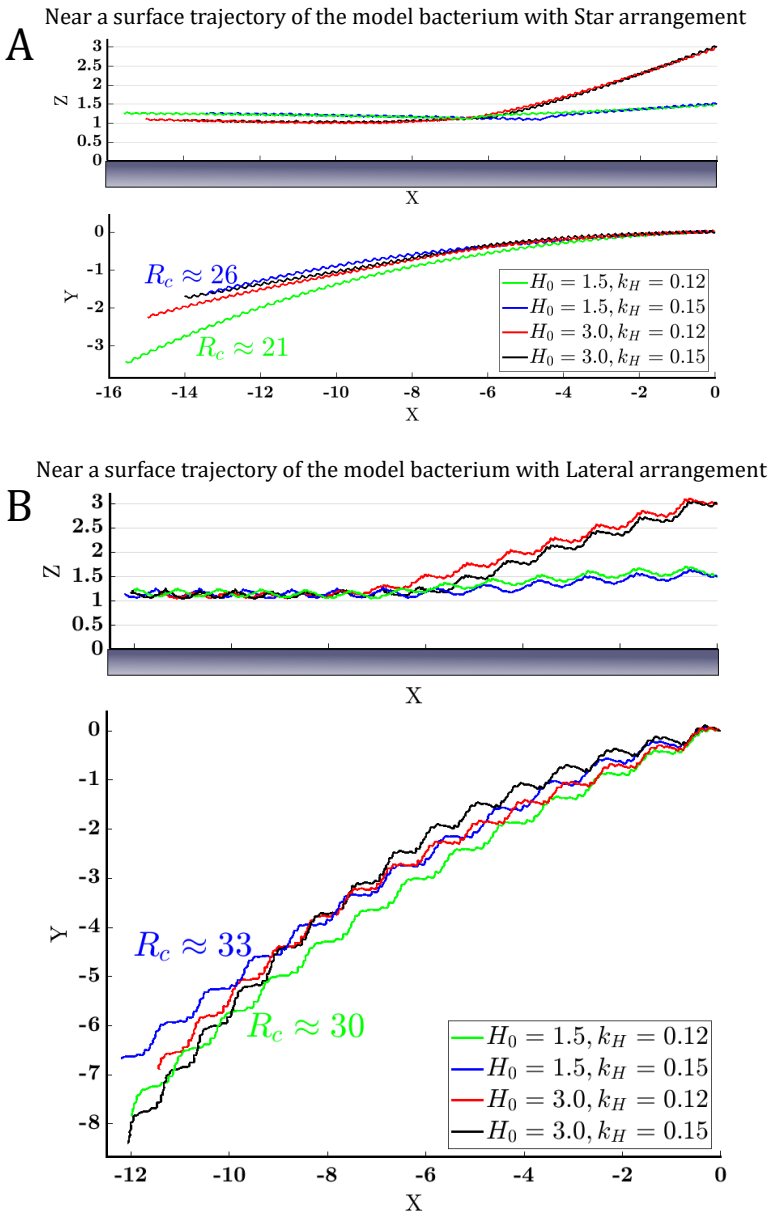

Figure 5.14: Swimming trajectories of the model bacteria with Star (A) and Lateral (B) flagella arrangement near a planar surface. The trajectories are shown for different initial conditions and hooks' stiffnesses. The attack angle for the black and red trajectories is $\alpha_0 = 18°$ and for the green and blue trajectories is $\alpha_0 = 0°$. The physical parameters of the model bacteria are stated at Tab. 5.1.

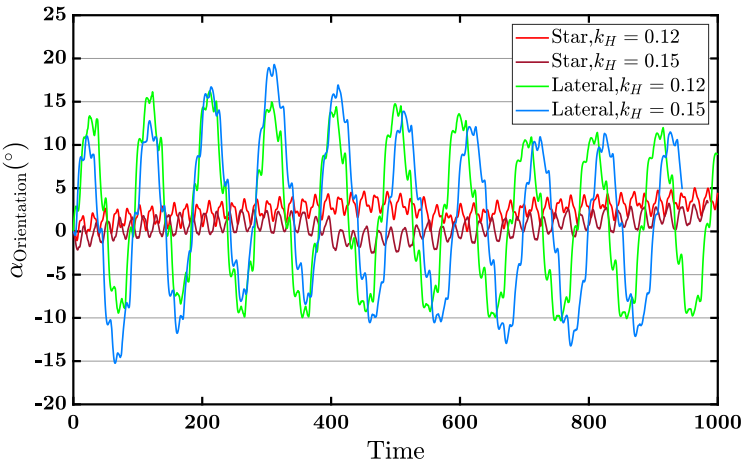

Figure 5.15: Angle between the long axis of the cell body and the planar surface over time, as the model bacteria with the Star and Lateral arrangements, swim near the wall. The results in this graph correspond to the presented trajectories in Fig. 5.14.

fluid. We conclude that if the average orientation of the cell body in the experimental measurements is positive, the bacteria have likely some specific swimming modes which are not considered in this section, or there is another explanation rather than the hydrodynamic interactions for this inconsistency.

5.11 Swimming properties inside a rectangular channel

Motivated by some experimental observations in which the locomotion of uni- and multi-flagellated bacteria inside a confined channel are monitored [119, 67, 12], we investigate the swimming properties of a model bacterium with Star arrangement inside a confined rectangular channel. To do this, we choose channels to be aligned with the $\vec{X}$ vector in the global frame, and the model bacterium is facing the $\vec{X}$ direction. To shorten the transition period and skip the flagella bundling progress, the steady configuration of the model bacterium in the bulk fluid is chosen as the initial condition, as displayed in Fig. 5.16. It is worth mentioning that the rest configuration of the model bacterium is as shown in Fig. 5.2. The model bacterium is initially placed at the middle of the channel such that $\vec{e}_1^{(B)}$ is aligned with the centerline of the channel, and two ends of the bacterium

have identical distances from two ends of the channel. This position guarantees that the closest grids of the walls to the bacterium's surface have a fine mesh size. We choose channels with identical dimensionless length $L_{\text{Channel}} = 30$, a dimensionless radius of fillet $R_{\text{Fillet}} = 0.1$, and varying dimensionless widths $W_{\text{Channel}} = 3.5, \cdots, 10$ to investigate the impacts of the channel's width on the swimming properties. We choose this length for the channels to approximate the infinite long channel by relying on previous numerical analysis by Shum [105]. In this analysis, it is shown that a channel with a length 2-3 times the combined body and flagellum length (i.e. $L_{\text{Channel}} \in [2 \times 14, 3 \times 14]$) is sufficient to mimic the role of an infinite-length channel. In this regard, the channel surfaces are covered with 1760 flat triangular elements generated by 3568 evaluation points ($N_{\text{PW}} = 3568$), recalling section 2.4.5 and Fig. 2.6.

Our results indicate that the significantly high shear forces/torques on the cell body and flagella notably reduce the rotational speeds of the flagella bundle and the cell body in the narrowest channel (i.e. $W_{\text{Channel}} = 3.5$). The small rotation rate of the bundle in addition to the large drag forces on the cell body lead to a relatively small forward swimming speed for the model bacterium in this channel, as displayed in Fig. 5.16. A slight increase in the channel's width increases the rotation frequency of the flagellar bundle and weakens the drag forces on the cell body; the result is a considerable increase in the swimming speed. Similar to what we see for the variation of the swimming speed near a planar surface (i.e. Fig. 5.13B), a local maximum is also observed for the swimming speed as the bacterium is inside a relatively narrow channel. Interestingly, such a sharp variation in the mean swimming speed of *E. coli* is already observed by Biondi et al. [12]. In this study, it is shown that *E. coli*'s mean speeds inside the channels with widths 3µm and 2µm are 10% higher and 25% lower than its speed in the bulk fluid, respectively.

By increasing the channel's width, the drag forces on the cell body and the flagellar bundle smoothly decrease, and hence the rotational and translational speeds of the model bacterium rise accordingly. As expected, the indices of the swimming properties gradually converge to the obtained results in the free space.

5.12 Summary and conclusion

In this chapter we reproduce the behavior of peritrichous bacteria such as flagellar bundling, reversal of motor, and run motion in free and half spaces to shed light on the different aspects of their behavior and qualitatively elucidate the influences of the several physical parameters on their swimming properties and style.

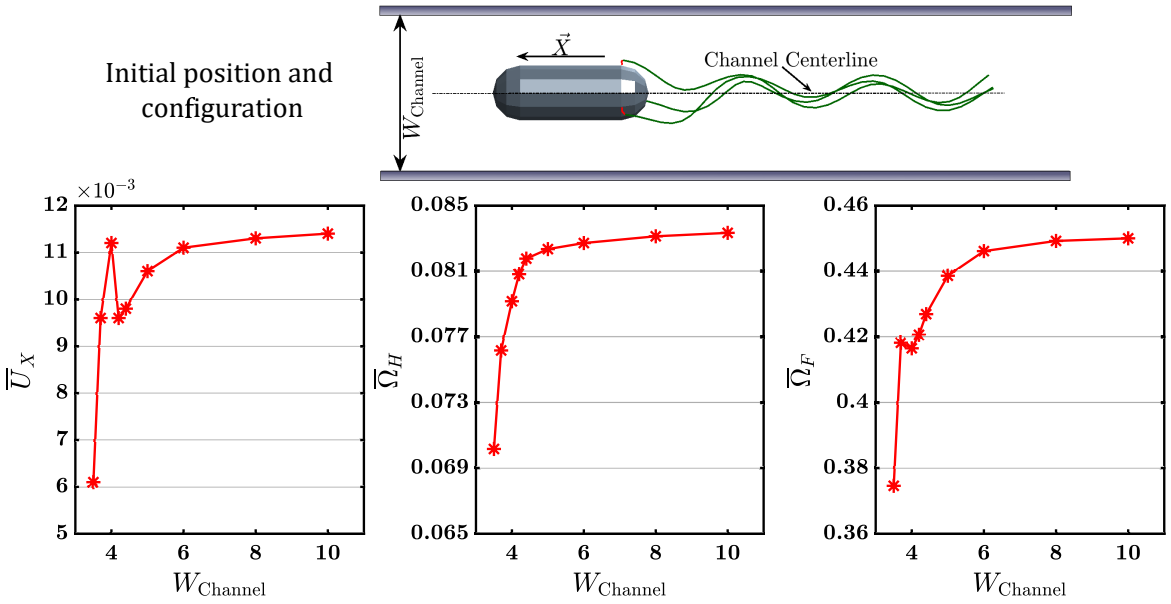

Figure 5.16: Swimming properties of multiflagellated model bacterium with Star arrangement inside a rectangular channel with curved edges. The physical properties of the model bacterium are described in Tab. 5.1.

We find that the feasible interval for the hook's rigidity to result in stable locomotion is altered not only by the number of the flagella (as studied by Nguyen and Graham [80]) but also by the flagellar arrangement. Our simulations indicate that whereas the model bacteria with the Star or Lateral arrangements at $k_H = 0.12$ execute stable forward locomotion, the hooks' instability in the Linear arrangement causes the flagella bundle to touch the cell body which results in a double helical trajectory. In particular, the minimum relative stiffnesses of hooks required for stable forward locomotion in the Star, Lateral, and Linear arrangements are in the ranges $k_{\mathrm{H,critical}} \in [0.09, 0.10]$, $k_{\mathrm{H,critical}} \in [0.11, 0.12]$ and $k_{\mathrm{H,critical}} \in [0.14, 0.15]$, respectively. By comparing the buckling thresholds in the uni- and multiflagellated bacteria, we note that the bundling effect between the flagella helps the hooks remain stable in the lower rigidity of the hooks. This comparison provides an explanation for why the hooks' stiffness in the multiflagellated bacteria is mainly lower than in the uniflagellated bacteria according to the experimental measurements. Moreover, we show that the hook's stiffness threshold is low for the flagellum that protrudes perpendicularly from the cylindrical part of the cell body and is highest for the flagellum that protrudes from the cell body's hemispherical ends.

In the studied flagellar arrangements (i.e. Star, Lateral, Linear), there are no notable differences in the average swimming speed of the model bacteria as long as the hooks are stable. However, the bundling time of the flagella and the average rotational speed of the cell body vary between the model bacteria with different arrangements. Our results show that the bacteria with non-axisymmetric flagellar arrangement likely swim on a double helical trajectory because the vector sum of the motor torques on the cell body is not aligned with the swimming orientation. This explains why the model bacterium with the Lateral arrangement moves on the double helical trajectory. A double helical trajectory can be observed in the bacteria with axisymmetric rest configurations as well because the vector sum of bending moments transmitted from the hook to the cell body does not align with the swimming orientation. The double helical trajectory observed in the second swimming mode of the model bacterium with the Star arrangement is due to the bending moments, for example. From an evolutionary point of view, the locomotion of multiflagellated bacteria on double helical trajectories does not provide any advantages in terms of the swimming speed; therefore, such locomotion could serve other purposes such as sampling strategy, etc.

The helical flagella curvature and torsion can significantly change the swimming properties of the multiflagellated bacteria. Our results show that the correlation between the flagella curvature/torsion and the rotation rate of the flagella bundle is monotonic. However, the correlation is non-monotonic for the average translational and rotational speeds of the bacteria. In this respect, the curvature and torsion can be chosen in a way that

maximizes the average swimming speed and/or minimizes the rotational speed of the cell body and/or minimize the bundling time. Interestingly, our results reveal that the curvature and torsion of the flagella in *E. coli* are optimal for the swimming speed. Even though it is expected that a higher rotation speed of the cell body decreases the bundling time in the multiflagellated bacteria, our results demonstrate the influences of the flagellum curvature and torsion in the bundling time are more important than the cell body's rotation speed. We make this conclusion because higher body rotation does not necessarily lead to a smaller bundling time as we vary the curvature and/or torsion of the flagella. This conclusion can not be generalized for a wider range of the hook and the flagella rigidity. It is fair to expect that the role of the cell body rotation on the bundling is more significant in the bacteria with more flexible hooks and filaments because the flagella deform easily and are entangled together due to the cell body rotation.

The swimming speed in the model bacterium with the Star arrangement is maximized when the hook has the lowest stiffness and the filament has the highest stiffness within the studied intervals. Considering the real hook and filament stiffnesses in the multiflagellated bacteria, it seems that the flagella structure in these bacteria is optimized for the average swimming speed. The obtained results in this chapter show that the most flexible hook yields the shortest bundling time, but this is not true for filaments. In particular, the bundling time is minimum in a bacterium with flagellar filaments of intermediate stiffness.

We note that the multiflagellated bacteria may have more than one swimming stable mode. Our interpretation is that the flagella arrangement on the cell body and their orientations at rest are two main factors that determine the number of stable swimming modes in the bacteria. Combining these modes with the modes due to the existence of several flagellar bundles [21], may lead to many stable swimming modes in some peritrichous bacteria. Our simulations disclose that the swimming properties and the trajectory of the multiflagellated bacteria may notably change in the different swimming modes. They can swim fast on a straight trajectory in the first mode, and move slowly on a double helical trajectory in the second mode, for example. The tumbling event, any pause in the flagellar motors, collision with surfaces, etc. can result in a switch to another mode.

Our studies show that the bundling time of the flagella in the peritrichous bacteria slightly increases near the surfaces. This is due to the smaller rotation rate of the cell body near the no-slip boundaries. Depending on the flagella arrangement, the variation of the swimming properties near the surfaces is different. Whereas the average swimming speed of the model bacterium with Lateral arrangement reduces strictly with the distance from the surface, it varies non-monotonically in the Star arrangement. Remarkably, the average swimming speed of the model bacterium with Lateral arrangement is about 7% more than the Star arrangement when both bacteria swim close (i.e. $H_0 = 1$) to the surface.

Such a difference in the swimming speeds could be helpful in designing some microdevices to sort the multiflagellated bacteria according to their flagella arrangement.

Chapter 6

Summary and Conclusion

In this thesis, we develop a comprehensive elastohydrodynamic model to simulate the locomotion of the flagellated micro-organisms, specifically bacteria, in a bounded and unbounded viscous fluid. The model bacteria consist of a spherical or a spherocylindrical cell body, flexible filament(s), very flexible hook(s), and flagellar motor(s). In our model, Boundary Integral Equations (BIE), relating the fluid velocity and stress distributions over the cell body and flagella, are solved to calculate the hydrodynamic interactions between the bacterium components and the surrounding fluid. For this purpose, the cell body surface is discretized into a finite number of curved triangular elements and the Gauss-Legendre quadrature method is used to evaluate the integrals over each triangle. The hook and flagellar filaments are discretized into a finite number of rigid straight segments that are joined end to end but allowed to rotate with respect to each other. The one-dimensional Gauss-Legendre method is used to approximate the line integral of regularized Stokeslets and rotlets along the flagella. The main aim of employing these methods is to represent the translational and angular velocities of the evaluation points in terms of the force and torque densities which are distributed on the boundary.

The hydrodynamic forces exerted on the flagellar filaments deform the flagella out of their static equilibrium configurations. Discretization of the standard Kirchhoff rod model enables us to represent the internal moments at the joints connecting the flagella segments in terms of the segments' orientations. These internal moments are used to write the torque balance equations about each joint on the flagella. It is worth mentioning that a sub-iterative method is employed in our numerical scheme to estimate the internal moment at the joint connecting the rotor to the first segment of the hook, to satisfy the Kirchhoff rod equation and the motor torque constraint.

In our model, steric repulsive forces are applied between the components of the bacterium, and between the bacterium and the boundaries to avoid collisions and instabilities of the numerical scheme due to practical limitations on time step sizes. All the introduced forces and torques come together to satisfy the total force and torque balance equations on the model bacterium. At the end, the kinematic equations in which the translational and angular velocities of each evaluation point on the swimmer are represented in terms of the angular velocities of the segments, the cell body's translational and angular velocities, are added to the hydrodynamic and force/torque balance equations to construct a system of linear equations. The system is solved for the force/torque densities and the velocities. Then, the configuration of the model bacterium is updated according to our ODE integration scheme.

Our results indicate that the steady motor torque and the swimming speed are different in the puller and pusher modes of uniflagellated model bacteria. In particular, a slight difference in the amplitude of the helical flexible filament in puller and pusher modes causes the swimming properties to be different. Moreover, our simulations demonstrate that the tendency of the uniflagellated model bacteria to swim close to surfaces changes with the concentration of NaCl in the swimming fluid. Since the model bacteria swim faster in the higher concentrations of ions, the cell body and flagellum are exposed to larger hydrodynamic forces due to no-slip boundary drag. These forces apply a larger bending moment to the hook and induce a larger bending angle. Therefore, the angle between the cell body's long axis and the surface gradually increases and the cell body escapes from the surface more easily. This conclusion is consistent with the experimental observation of *V. alginolyticus* locomotion near the surfaces as it is in the pusher mode. In the puller mode, changing the concentrations does not change the tendency of the model bacteria to swim near the surfaces and the bacteria always accumulate near the surfaces. Boundary accumulating behavior in the puller mode has already been observed in *Caulobacter crescentus* which has a similar shape to the studied uniflagellated model bacterium in this thesis. Based on our modeling assumptions in this thesis, changing the concentrations of the ions is effectively equivalent to changing the flagella stiffness as the important quantity is the ratio of the motor torque to flexural rigidity. Therefore, a similar correlation exists between the flagella stiffness and the bacteria's behavior near surfaces. In addition, we note the cell body aspect ratio is one of the key parameters in the tendency of the uniflagellated bacteria for the boundary accumulating. Remarkably, our results show that if a model bacterium with a rigid flagellum is attracted to the surfaces it does not guarantee that it is still entrapped by the surface when the flagellum is flexible. Our simulations reveal that if the loaded hook stiffness in the uniflagellated bacteria is close to the buckling threshold, the high shear forces due to a no-slip boundary may make the hook

unstable. In some cases, this instability may cause the bacteria to be locally entrapped near the surfaces.

A biflagellated model bacterium with a spherical cell body, one puller, and one pusher flagellum moves on a double helical trajectory except when $\alpha = \beta = 0^\circ$ in Fig. 4.1. Our results show that the size of the large helices in the swimming trajectory varies according to the degree of the asymmetry, the flagella's position, orientation, and stiffness. Comparing the properties of the trajectories obtained numerically with the trajectories of *M. marinus* measured experimentally, discloses that this bacterium has likely one puller and one pusher flagella, and the flagella are relatively stiff in comparison with the other species. Moreover, our simulations indicate that the puller flagellum has better alignment with the swimming direction. One interpretation is that the generated thrust by the puller flagellum is more effectively used to propel the bacterium in the swimming direction. We note that the pusher flagellum may exhibit overwhirling stable rotation as either the torque applied to the flagellar filament surpasses a critical value and/or the flagellum rigidity is below a critical value.

Studying the locomotion of multiflagellated bacteria with three flagella and spherocylindrical cell body (inspiration from *E. coli*) shows that a single flagellar bundle forms behind the cell body as the helical flagella start to rotate in a same direction. The simulations demonstrate that the flagellar bundle unravels and the cell body reorients when at least one motor switches the rotation direction. We note that depending on the degree of the axisymmetry in the rest configuration of the bacteria, they likely move on relatively straight trajectories or double helical trajectories. By comparing the swimming properties in the different flagellar arrangements, we find that the average swimming speed is less affected by the flagellar arrangements as long as the flagella rotations are stable. Our investigations disclose that there is an optimum value for the flagella curvature and torsion to maximize the averaged swimming speed and/or minimize the bundling time in the multiflagellated bacteria. Interestingly, the flagella curvature and torsion in *E. coli* are close to those optimums. Remarkably, our results show that the multiflagellated bacteria may possess several swimming modes with unique properties at each mode. For this reason, a variety of speeds and trajectories are expected to be observed in one specific kind of bacteria or in an individual cell. One interpretation is that each swimming mode is optimized for a particular purpose. For example, the bacterium switches to a mode with a small swimming speed and a large double-helical trajectory in the "sampling" state, and to a mode with a large swimming speed and a relatively straight trajectory in the "run" state.

Depending on the flagella arrangement, the response of the multiflagellated bacteria to the surfaces may be different. For instance, the angular speed of the bacteria with the Lateral arrangement is less affected by the surfaces in comparison with the bacteria with

the Star arrangement. Conversely, the variation in forward swimming is more notable in the Lateral arrangement. These differences in the responses cause the bacteria to move on circular arcs with different radiuses as they swim near a surface. The bacteria with the Star arrangement move on smaller circles because they have smaller translational and larger rotational speeds in comparison with the Lateral arrangement.

6.1 Recommendations for future works

The following topics are recommended for future works in studying bacterial locomotion:

Reduce the computational time: The major issue we were faced with in the present thesis was the small time step required to model the deformations of the flexible filaments in a viscous fluid. Employing the multirate time integration scheme reduced the computational time by 50%. Furthermore, several programming languages including *Fortran* and *Python*, and different numerical methods were tested in terms of computational speeds. In addition, the prepared code in *Matlab* was optimized in different aspects, but the computational time still prevents us from studying much more complicated phenomena. Therefore, employing other numerical techniques like the Fast Multipole Method and using GPU computing will be beneficial in future works.

Bacterial locomotion in Non-Newtonian fluid: Throughout the current study, it is assumed that the bacteria swim in a Newtonian fluid, such as fresh water. However, many kinds of bacteria naturally live in biological fluids, such as mucus, which are mainly non-Newtonian. The locomotion of flagellated bacteria in non-Newtonian media is largely unexplored and some more investigations are still required to elucidate the different aspects of their behavior in their natural habitat. Furthermore, designing some bacterial mimicking microrobots with biomedical applications is not possible without a deep understanding of the role of non-Newtonian fluids on the dynamics of the microswimmers. If the boundary integral equations employed here are adjusted to be used for non-Newtonian fluids, then the presented scheme can be applied to this purpose. Otherwise, some other numerical methods like Immersed Boundary Method can be used to model the hydrodynamic interactions between the non-Newtonian fluids and the bacteria components.

Inhibit biofilm formation: The results obtained in chapter 3 indicated that increasing the NaCl concentration in the swimming medium could keep the pusher-mode bacteria away from the surfaces, and therefore reduces the chance of biofilm formation. A relatively similar correlation between the ions' concentration and boundary accumulating behavior is likely expected for other species as well. It is concluded that changing the ions concentration near the susceptible surfaces might decelerate the process of biofilm formation.

In addition, an analysis by Sipos et al. [112] has demonstrated that the tendency of the bacteria to swim near convex surfaces changes with the convexity radius. Bacteria swim away from surfaces with a convexity radius smaller than some critical value (R^{**}) that depends on the bacterium length and the stable angle of the bacterium with the wall when the bacterium is entrapped near a flat wall. This critical radius is about $R^{**} = 57\,\mu m$ for *E. coli*. Since this analysis is conducted by assuming that the convexity radius is much larger than the cell body size, the feasibility range of radius for repelling the bacteria is limited. This preliminary analysis indicates that the chance of biofilm formation is likely low on a wavy surface in which the curvature of any point on the surface is slightly larger than $\frac{1}{R^{**}}$. However, a comprehensive study is required to investigate the interaction between the swimming bacteria and such a wavy surface to conclude about reducing biofilm formation through changing the surface topology.

Variable hook stiffness: Experimental measurements have illustrated that hook stiffness in bacteria dynamically changes by the load. Such a strain-stiffening mechanism allows the hook to be flexible when either the flagellar bundle forms or the bacterium tends to flick and be stiffer under high hydrodynamic loads [81, 115]. In the present work, we assumed that the hook stiffness is always constant and equal to its stiffness in the loaded state. Based on this assumption, we were unable to mimic the flagellum flicking in *V. alginolyticus*. It seems that the dynamic stiffing of the hook plays a key role in the flicking of the flagellum. However, some more simulations with this assumption are required to discover different aspects of this and some other special phenomena in bacteria.

Wrapping of the puller flagellum: In chapter 4, we showed that if the torque applied to a pusher flagellum surpasses a threshold, it enters an overwhirling state in which the flagellum experiences large deformations and the free end of the flagellum gets close to the driven end. Our preliminary simulations indicated that if the torque applied to a puller flagellum surpasses a threshold, which is different from the threshold that exists for the pusher flagellum, the puller flagellum bends toward the cell body and tends to wrap around it. Similar behavior was recently reported by Park et al. [85], where it is shown that the puller flagellum's wrapping mode can help the bacteria to escape from the surfaces. Different aspects of this model and how it affects the behavior of uni- and multiflagellated bacteria are not well understood yet and there are still several unanswered questions in this respect to be answered. For instance, is the wrapping mode only observed in uniflagellated bacteria? Is the wrapping of the flagellum possible under the effect of the rotation of the other flagella in multiflagellated bacteria? What is the role of the cell body shape in the wrapping of the flagellum?

Polymorphic transformations of the flagellum during tumbling event: In this study, we simply showed that if at least one flagellum switches its rotation direction

in a bundle, the bundle unravels, the corresponding flagellum leaves the bundle and the cell body is reoriented. However, several experimental observations have shown that the corresponding flagellum executes polymorphic transformation and its shape changes to semi-coiled [124, 57, 35] during the tumbling event. Consequently and in order to better understand the tumbling behavior in multiflagellated bacteria and see how the bacteria exploit it to randomly change their orientation toward the desirable environments, it is necessary that this transformation is considered in upcoming studies.

U-turn inside a confined channel: Experimental observations of bacteria motility inside straight narrow channels (their width are in the order of the cell body sizes) have illustrated that bacteria (uni- or multiflagellated) sometimes execute U-turns inside the channel. According to these observations, the size, shape, and length of the cell bodies and the flagella are some key factors that determine the fraction of the bacteria which exhibit U-turns [119]. Some numerical simulations to reproduce the bacteria motility inside the channels could shed light on different aspects of this interesting behavior. Our results in this thesis indicated the translational and angular velocities of the bacterium vary sharply with position inside the channel. It would be interesting to explain the reasons behind these sharp variations. It is recommended that fine grids are used to cover the walls and the cell body surface to yield better numerical accuracy in the narrow channels. However, some optimization in terms of computational time and memory usage are also required in the presented scheme to do such simulations in a reasonable time period.

Unique structure of the flagella in *M. marinus*: As described in chapter 4, the flagella structure in *M. Marinus* is different from other kinds of bacteria. Each bundle in *M. marinus* is composed of seven flagellar filaments and many fibrils enveloped in a sheath. We are unaware of any numerical or experimental studies to provide data about the overall stiffness of the flagella filament and hook in this kind of bacteria, Moreover, the role of such a structure in the swimming and behavior of the bacteria is still unclear. Therefore, some experimental and numerical studies could improve our knowledge about the morphology of this bacterium, especially because its biomedical applications for drug delivery have already been proven.

References

[1] Tapan Chandra Adhyapak and Holger Stark. Zipping and entanglement in flagellar bundle of e. coli: Role of motile cell body. *Physical Review E*, 92(5):052701, 2015.

[2] Adib Ahmadzadegan, Shiyan Wang, Pavlos P Vlachos, and Arezoo M Ardekani. Hydrodynamic attraction of bacteria to gas and liquid interfaces. *Physical Review E*, 100(6):062605, 2019.

[3] Josephine Ainley, Sandra Durkin, Rafael Embid, Priya Boindala, and Ricardo Cortez. The method of images for regularized stokeslets. *Journal of Computational Physics*, 227(9):4600–4616, 2008.

[4] Mukrime Birgul Akolpoglu, Yunus Alapan, Nihal Olcay Dogan, Saadet Fatma Baltaci, Oncay Yasa, Gulsen Aybar Tural, and Metin Sitti. Magnetically steerable bacterial microrobots moving in 3d biological matrices for stimuli-responsive cargo delivery. *Science Advances*, 8(28):eabo6163, 2022.

[5] Nolle Amarger. Genetically modified bacteria in agriculture. *Biochimie*, 84(11):1061–1072, 2002.

[6] Klaas Bente, Sarah Mohammadinejad, Mohammad Avalin Charsooghi, Felix Bachmann, Agnese Codutti, Christopher T Lefèvre, Stefan Klumpp, and Damien Faivre. High-speed motility originates from cooperatively pushing and pulling flagella bundles in bilophotrichous bacteria. *Elife*, 9:e47551, 2020.

[7] Howard C Berg. *E. coli in Motion*. Springer, 2004.

[8] Howard C Berg and Linda Turner. Chemotaxis of bacteria in glass capillary arrays. Escherichia coli, motility, microchannel plate, and light scattering. *Biophysical Journal*, 58(4):919–930, 1990.

[9] Allison P Berke, Linda Turner, Howard C Berg, and Eric Lauga. Hydrodynamic attraction of swimming microorganisms by surfaces. *Physical Review Letters*, 101(3):038102, 2008.

[10] Silvio Bianchi, Filippo Saglimbeni, and Roberto Di Leonardo. Holographic imaging reveals the mechanism of wall entrapment in swimming bacteria. *Physical Review X*, 7(1):011010, 2017.

[11] Silvio Bianchi, Filippo Saglimbeni, Giacomo Frangipane, Dario Dell'Arciprete, and Roberto Di Leonardo. 3d dynamics of bacteria wall entrapment at a water–air interface. *Soft Matter*, 15(16):3397–3406, 2019.

[12] Sherri A Biondi, John A Quinn, and Howard Goldfine. Random motility of swimming bacteria in restricted geometries. *AIChE Journal*, 44(8):1923–1929, 1998.

[13] John R Blake. A note on the image system for a stokeslet in a no-slip boundary. In *Mathematical Proceedings of the Cambridge Philosophical Society*, volume 70, pages 303–310. Cambridge University Press, 1971.

[14] Elizabeth L Bouzarth and Michael L Minion. A multirate time integrator for regularized stokeslets. *Journal of Computational Physics*, 229(11):4208–4224, 2010.

[15] MR BROWN and Paul Williams. The influence of evironment on envelope properties affecting survival of bacteria in infections. *Annual Review of Microbiology*, 39:527–556, 1985.

[16] Johannes Martinus Burgers. On the motion of small particles of elongated form suspended in a viscous liquid. *Kon. Ned. Akad. Wet. Verhand.(Eerste Sectie)*, 16:113–184, 1938.

[17] Xiaobing Chen and Howard C Berg. Solvent-isotope and pH effects on flagellar rotation in *Escherichia coli*. *Biophysical Journal*, 78(5):2280–2284, 2000.

[18] Xiaobing Chen and Howard C Berg. Torque-speed relationship of the flagellar rotary motor of Escherichia coli. *Biophysical Journal*, 78(2):1036–1041, 2000.

[19] Nadia Chouaïeb. *Kirchhoff's problem of helical solutions of uniform rods and their stability properties*. PhD thesis, Verlag nicht ermittelbar, 2003.

[20] AT Chwang and Th Y Wu. A note on the helical movement of micro-organisms. *Proceedings of the Royal Society of London. Series B. Biological Sciences*, 178(1052):327–346, 1971.

[21] Judit Clopés and Roland G Winkler. Flagellar arrangements in elongated peritrichous bacteria: bundle formation and swimming properties. *The European Physical Journal E*, 44(2):1–12, 2021.

[22] Jacinta C Conrad. Physics of bacterial near-surface motility using flagella and type iv pili: implications for biofilm formation. *Research in Microbiology*, 163(9-10):619–629, 2012.

[23] Maira A Constantino, Mehdi Jabbarzadeh, Henry C Fu, Zeli Shen, James G Fox, Freddy Haesebrouck, Sara K Linden, and Rama Bansil. Bipolar lophotrichous helicobacter suis combine extended and wrapped flagella bundles to exhibit multiple modes of motility. *Scientific Reports*, 8(1):1–15, 2018.

[24] Ricardo Cortez, Lisa Fauci, and Alexei Medovikov. The method of regularized stokeslets in three dimensions: analysis, validation, and application to helical swimming. *Physics of Fluids*, 17(3):031504, 2005.

[25] Ricardo Cortez and Douglas Varela. A general system of images for regularized stokeslets and other elements near a plane wall. *Journal of Computational Physics*, 285:41–54, 2015.

[26] John William Costerton, RT Irvin, and KJ Cheng. The bacterial glycocalyx in nature and disease. *Annual Reviews of Microbiology*, 35(1):299–324, 1981.

[27] RG Cox. The motion of long slender bodies in a viscous fluid part 1. General theory. *Journal of Fluid Mechanics*, 44(4):791–810, 1970.

[28] Hugh C Crenshaw. Orientation by helical motion - iii. microorganisms can orient to stimuli by changing the direction of their rotational velocity. *Bulletin of Mathematical Biology*, 55(1):231–255, 1993.

[29] Nicholas C Darnton and Howard C Berg. Force-extension measurements on bacterial flagella: triggering polymorphic transformations. *Biophysical Journal*, 92(6):2230–2236, 2007.

[30] Nicholas C Darnton, Linda Turner, Svetlana Rojevsky, and Howard C Berg. On torque and tumbling in swimming Escherichia coli. *Journal of Bacteriology*, 189(5):1756–1764, 2007.

[31] Philip Davis and Philip Rabinowitz. Abscissas and weights for gaussian quadratures of high order. *Journal of Research of the National Bureau of Standards - B*, 56(1):35–37, 1956.

[32] J E Duddridge, CA Kent, and JF Laws. Effect of surface shear stress on the attachment of *Pseudomonas fluorescens* to stainless steel under defined flow conditions. *Biotechnology and Bioengineering*, 24(1):153–164, 1982.

[33] DA Dunavant. High degree efficient symmetrical gaussian quadrature rules for the triangle. *International Journal for Numerical Methods in Engineering*, 21(6):1129–1148, 1985.

[34] David B Dusenbery. Minimum size limit for useful locomotion by free-swimming microbes. *Proceedings of the National Academy of Sciences*, 94(20):10949–10954, 1997.

[35] Mariia Dvoriashyna and Eric Lauga. Hydrodynamics and direction change of tumbling bacteria. *Plos One*, 16(7):e0254551, 2021.

[36] Ouajdi Felfoul, Mahmood Mohammadi, Samira Taherkhani, Dominic De Lanauze, Yong Zhong Xu, Dumitru Loghin, Sherief Essa, Sylwia Jancik, Daniel Houle, Michel Lafleur, et al. Magneto-aerotactic bacteria deliver drug-containing nanoliposomes to tumour hypoxic regions. *Nature Nanotechnology*, 11(11):941–947, 2016.

[37] Heather Flores, Edgar Lobaton, Stefan Méndez-Diez, Svetlana Tlupova, and Ricardo Cortez. A study of bacterial flagellar bundling. *Bulletin of Mathematical Biology*, 67(1):137–168, 2005.

[38] KW Foster and RD Smyth. Light antennas in phototactic algae. *Microbiological Reviews*, 44(4):572–630, 1980.

[39] Paul D Frymier, Roseanne M Ford, Howard C Berg, and Peter T Cummings. Three-dimensional tracking of motile bacteria near a solid planar surface. *Proceedings of the National Academy of Sciences*, 92(13):6195–6199, 1995.

[40] Tatsuya Fujita and Tatsuo Kawai. Optimum shape of a flagellated microorganism. *JSME International Journal Series C Mechanical Systems, Machine Elements and Manufacturing*, 44(4):952–957, 2001.

[41] Peter Galajda, Juan Keymer, Paul Chaikin, and Robert Austin. A wall of funnels concentrates swimming bacteria. *Journal of Bacteriology*, 189(23):8704–8707, 2007.

[42] Alain Goriely and Michael Tabor. Nonlinear dynamics of filaments. iii. instabilities of helical rods. *Proceedings of the Royal Society of London. Series A: Mathematical, Physical and Engineering Sciences*, 453(1967):2583–2601, 1997.

[43] James Gray and GJ Hancock. The propulsion of sea-urchin spermatozoa. *Journal of Experimental Biology*, 32(4):802–814, 1955.

[44] GJ Hancock. The self-propulsion of microscopic organisms through liquids. *Proceedings of the Royal Society of London. Series A. Mathematical and Physical Sciences*, 217(1128):96–121, 1953.

[45] Jonathan JL Higdon. A hydrodynamic analysis of flagellar propulsion. *Journal of Fluid Mechanics*, 90(4):685711, 1979.

[46] Jonathan JL Higdon. The hydrodynamics of flagellar propulsion: helical waves. *Journal of Fluid Mechanics*, 94(2):331–351, 1979.

[47] Jane Hill, Ozge Kalkanci, Jonathan L McMurry, and Hur Koser. Hydrodynamic surface interactions enable Escherichia coli to seek efficient routes to swim upstream. *Physical Review Letters*, 98(6):068101, 2007.

[48] Berthold KP Horn. Closed-form solution of absolute orientation using unit quaternions. *Journal of the Optical Society of America A*, 4(4):629–642, 1987.

[49] Weicheng Huang and M Khalid Jawed. Numerical simulation of bundling of helical elastic rods in a viscous fluid. *Computers & Fluids*, 228:105038, 2021.

[50] Elizabeth Hulme S, Willow R DiLuzio, Sergey S Shevkoplyas, Linda Turner, Michael Mayer, Howard C Berg, and George M Whitesides. Using ratchets and sorters to fractionate motile cells of *Escherichia coli* by length. *Lab on a Chip*, 8(11):1888–1895, 2008.

[51] Christine Josenhans and Sebastian Suerbaum. The role of motility as a virulence factor in bacteria. *International Journal of Medical Microbiology*, 291(8):605–614, 2002.

[52] Philipp Kanehl and Takuji Ishikawa. Fluid mechanics of swimming bacteria with multiple flagella. *Physical Review E*, 89(4):042704, 2014.

[53] David F Katz, John R Blake, and SL Paveri-Fontana. On the movement of slender bodies near plane boundaries at low reynolds number. *Journal of Fluid Mechanics*, 72(3):529–540, 1975.

[54] Tolga Kaya and Hur Koser. Direct upstream motility in Escherichia coli. *Biophysical Journal*, 102(7):1514–1523, 2012.

[55] Joseph B Keller and SI Rubinow. Swimming of flagellated microorganisms. *Biophysical Journal*, 16(2):151–170, 1976.

[56] MunJu Kim and Thomas R Powers. Hydrodynamic interactions between rotating helices. *Physical Review E*, 69(6):061910, 2004.

[57] Marco J Kühn, Felix K Schmidt, Bruno Eckhardt, and Kai M Thormann. Bacteria exploit a polymorphic instability of the flagellar filament to escape from traps. *Proceedings of the National Academy of Sciences*, 114(24):6340–6345, 2017.

[58] Eric Lauga, Willow R DiLuzio, George M Whitesides, and Howard A Stone. Swimming in circles: motion of bacteria near solid boundaries. *Biophysical Journal*, 90(2):400–412, 2006.

[59] Eric Lauga and Thomas R Powers. The hydrodynamics of swimming microorganisms. *Reports on Progress in Physics*, 72(9):096601, 2009.

[60] Wanho Lee, Yongsam Kim, Charles S Peskin, and Sookkyung Lim. A novel computational approach to simulate microswimmers propelled by bacterial flagella. *Physics of Fluids*, 33(11):111903, 2021.

[61] Laurence Lemelle, Jean-François Palierne, Elodie Chatre, Cedric Vaillant, and Christophe Place. Curvature reversal of the circular motion of swimming bacteria probes for slip at solid/liquid interfaces. *Soft Matter*, 9(41):9759–9762, 2013.

[62] Guanglai Li, James Bensson, Liana Nisimova, Daniel Munger, Panrapee Mahautmr, Jay X Tang, Martin R Maxey, and Yves V Brun. Accumulation of swimming bacteria near a solid surface. *Physical Review E*, 84(4):041932, 2011.

[63] Guanglai Li, Lick-Kong Tam, and Jay X Tang. Amplified effect of brownian motion in bacterial near-surface swimming. *Proceedings of the National Academy of Sciences*, 105(47):18355–18359, 2008.

[64] Jinxing Li, Berta Esteban-Fernández de Ávila, Wei Gao, Liangfang Zhang, and Joseph Wang. Micro/nanorobots for biomedicine: Delivery, surgery, sensing, and detoxification. *Science Robotics*, 2017.

[65] James Lighthill. Flagellar hydrodynamics. *SIAM Review*, 18(2):161–230, 1976.

[66] Sookkyung Lim, Anca Ferent, X Sheldon Wang, and Charles S Peskin. Dynamics of a closed rod with twist and bend in fluid. *SIAM Journal on Scientific Computing*, 31(1):273–302, 2008.

[67] Hsin-Yu Lin. *Motility and intelligence of microorganisms in microconfined networks*. McGill University (Canada), 2017.

[68] Guangzhe Liu, Zhaorong Liu, Lailai Zhu, Rongjing Zhang, and Junhua Yuan. Upcoming flow promotes the bundle formation of bacterial flagella. *Biophysical Journal*, 120(20):4391–4398, 2021.

[69] MA Lock, RR Wallace, John William Costerton, RM Ventullo, and SE Charlton. River epilithon: toward a structural-functional model. *Oikos*, pages 10–22, 1984.

[70] Dan L Longo, J Larry Jameson, and Dennis Kaspe. *Harrison's Principles of Internal Medicine: Volume 2*. Macgraw-Hill, 2011.

[71] Diego Lopez and Eric Lauga. Dynamics of swimming bacteria at complex interfaces. *Physics of Fluids*, 26(7):400–412, 2014.

[72] Michael T Madigan, John M Martinko, Jack Parker, et al. *Brock biology of microorganisms*. Prentice hall Upper Saddle River, NJ, 1997.

[73] Tohru Minamino, Yasuo Imae, Fumio Oosawa, Yuji Kobayashi, and Kenji Oosawa. Effect of intracellular pH on rotational speed of bacterial flagellar motors. *Journal of Bacteriology*, 185(4):1190–1194, 2003.

[74] Sarah Mohammadinejad, Damien Faivre, and Stefan Klumpp. Stokesian dynamics simulations of a magnetotactic bacterium. *The European Physical Journal E*, 44(3):1–12, 2021.

[75] Mehdi Molaei, Michael Barry, Roman Stocker, and Jian Sheng. Failed escape: solid surfaces prevent tumbling of Escherichia coli. *Physical Review Letters*, 113(6):068103, 2014.

[76] Rohan Nadkarni, Solomon Barkley, and Cécile Fradin. A comparison of methods to measure the magnetic moment of magnetotactic bacteria through analysis of their trajectories in external magnetic fields. *PloS one*, 8(12):e82064, 2013.

[77] Shuichi Nakamura, Nobunori Kami-ike, P Yokota Jun-ichi, Seishi Kudo, Tohru Minamino, and Keiichi Namba. Effect of intracellular pH on the torque–speed relationship of bacterial proton-driven flagellar motor. *Journal of Molecular Biology*, 386(2):332–338, 2009.

[78] Shuichi Nakamura and Tohru Minamino. Flagella-driven motility of bacteria. *Biomolecules*, 9(7):279, 2019.

[79] Bradley J Nelson, Ioannis K Kaliakatsos, and Jake J Abbott. Microrobots for minimally invasive medicine. *Annual Review of Biomedical Engineering*, 12:55–85, 2010.

[80] Frank TM Nguyen and Michael D Graham. Impacts of multiflagellarity on stability and speed of bacterial locomotion. *Physical Review E*, 98(4):042419, 2018.

[81] Ashley L Nord, Anaïs Biquet-Bisquert, Manouk Abkarian, Théo Pigaglio, Farida Seduk, Axel Magalon, and Francesco Pedaci. Dynamic stiffening of the flagellar hook. *Nature Communications*, 13(1):1–9, 2022.

[82] Sarah D Olson, Sookkyung Lim, and Ricardo Cortez. Modeling the dynamics of an elastic rod with intrinsic curvature and twist using a regularized stokes formulation. *Journal of Computational Physics*, 238:169–187, 2013.

[83] George O'Toole, Heidi B Kaplan, and Roberto Kolter. Biofilm formation as microbial development. *Annual Review of Microbiology*, 54:49, 2000.

[84] Byung-Wook Park, Jiang Zhuang, Oncay Yasa, and Metin Sitti. Multifunctional bacteria-driven microswimmers for targeted active drug delivery. *ACS Nano*, 11(9):8910–8923, 2017.

[85] Jeungeun Park, Yongsam Kim, Wanho Lee, and Sookkyung Lim. Modeling of lophotrichous bacteria reveals key factors for swimming reorientation. *Scientific Reports*, 12(1):1–12, 2022.

[86] Yunyoung Park, Yongsam Kim, William Ko, and Sookkyung Lim. Instabilities of a rotating helical rod in a viscous fluid. *Physical Review E*, 95(2):022410, 2017.

[87] Yunyoung Park, Yongsam Kim, and Sookkyung Lim. Flagellated bacteria swim in circles near a rigid wall. *Physical Review E*, 100(6):063112, 2019.

[88] Yunyoung Park, Yongsam Kim, and Sookkyung Lim. Locomotion of a single-flagellated bacterium. *Journal of Fluid Mechanics*, 859:586–612, 2019.

[89] N Phan-Thien, T Tran-Cong, and M Ramia. A boundary-element analysis of flagellar propulsion. *Journal of Fluid Mechanics*, 184:533–549, 1987.

[90] Constantine Pozrikidis. *A practical guide to boundary element methods with the software library BEMLIB*. CRC Press, 2002.

[91] Famin Qiu, Rami Mhanna, Li Zhang, Yun Ding, Satoshi Fujita, and Bradley J Nelson. Artificial bacterial flagella functionalized with temperature-sensitive liposomes for controlled release. *Sensors and Actuators B: Chemical*, 196:676–681, 2014.

[92] Zijie Qu, Fatma Zeynep Temel, Rene Henderikx, and Kenneth S Breuer. Changes in the flagellar bundling time account for variations in swimming behavior of flagellated bacteria in viscous media. *Proceedings of the National Academy of Sciences*, 115(8):1707–1712, 2018.

[93] M Ramia, DL Tullock, and N Phan-Thien. The role of hydrodynamic interaction in the locomotion of microorganisms. *Biophysical Journal*, 65(2):755–778, 1993.

[94] Michael Reichert and Holger Stark. Synchronization of rotating helices by hydrodynamic interactions. *The European Physical Journal E*, 17(4):493–500, 2005.

[95] Shang Yik Reigh, Roland G Winkler, and Gerhard Gompper. Synchronization and bundling of anchored bacterial flagella. *Soft Matter*, 8(16):4363–4372, 2012.

[96] Shang Yik Reigh, Roland G Winkler, and Gerhard Gompper. Synchronization, slippage, and unbundling of driven helical flagella. *PloS One*, 8(8):e70868, 2013.

[97] GD Reilly, CA Reilly, EG Smith, and C Baker-Austin. Vibrio alginolyticus-associated wound infection acquired in british waters, guernsey, july 2011. *Eurosurveillance*, 16(42):19994, 2011.

[98] AJ Reynolds. The swimming of minute organisms. *Journal of Fluid Mechanics*, 23(2):241–260, 1965.

[99] Soheil Sarabandi and Federico Thomas. Accurate computation of quaternions from rotation matrices. In *Advances in Robot Kinematics 2018*, pages 39–46. Springer, 2018.

[100] JM Schierholz and J Beuth. Implant infections: a haven for opportunistic bacteria. *Journal of Hospital Infection*, 49(2):87–93, 2001.

[101] Ilkin Yucel Sengun and Seniz Karabiyikli. Importance of acetic acid bacteria in food industry. *Food Control*, 22(5):647–656, 2011.

[102] Ania Servant, Famin Qiu, Mariarosa Mazza, Kostas Kostarelos, and Bradley J Nelson. Controlled in vivo swimming of a swarm of bacteria-like microrobotic flagella. *Advanced Materials*, 27(19):2981–2988, 2015.

[103] Tanvir R Shaikh, Dennis R Thomas, James Z Chen, Fadel A Samatey, Hideyuki Matsunami, Katsumi Imada, Keiichi Namba, and David J DeRosier. A partial atomic structure for the flagellar hook of salmonella typhimurium. *Proceedings of the National Academy of Sciences*, 102(4):1023–1028, 2005.

[104] Stanley W Shepperd. Quaternion from rotation matrix. *Journal of Guidance and Control*, 1(3):223–224, 1978.

[105] Henry Shum. *Simulations and modelling of bacterial flagellar propulsion*. PhD thesis, University of Oxford, 2011.

[106] Henry Shum. Microswimmer propulsion by two steadily rotating helical flagella. *Micromachines*, 10(1):65, 2019.

[107] Henry Shum and Eamonn A Gaffney. The effects of flagellar hook compliance on motility of monotrichous bacteria: A modeling study. *Physics of Fluids*, 24(6):061901, 2012.

[108] Henry Shum and Eamonn A Gaffney. Hydrodynamic analysis of flagellated bacteria swimming in corners of rectangular channels. *Physical Review E*, 92(6):063016, 2015.

[109] Henry Shum and Eamonn A Gaffney. Hydrodynamic analysis of flagellated bacteria swimming near one and between two no-slip plane boundaries. *Physical Review E*, 91(3):033012, 2015.

[110] Henry Shum, Eamonn A Gaffney, and David J Smith. Modelling bacterial behaviour close to a no-slip plane boundary: the influence of bacterial geometry. *Proceedings of the Royal Society A: Mathematical, Physical and Engineering Sciences*, 466(2118):1725–1748, 2010.

[111] Manuel Simões, Lúcia C Simões, and Maria J Vieira. A review of current and emergent biofilm control strategies. *LWT-Food Science and Technology*, 43(4):573–583, 2010.

[112] O Sipos, K Nagy, R Di Leonardo, and P Galajda. Hydrodynamic trapping of swimming bacteria by convex walls. *Physical Review Letters*, 114(25):258104, 2015.

[113] Peter M Slovak, George H Wadhams, and Judith P Armitage. Localization of MreB in *Rhodobacter sphaeroides* under conditions causing changes in cell shape and membrane structure, 2005.

[114] David J Smith and John R Blake. Surface accumulation of spermatozoa: a fluid dynamic phenomenon. *arXiv preprint arXiv:1007.2153*, 2010.

[115] Kwangmin Son, Jeffrey S Guasto, and Roman Stocker. Bacteria can exploit a flagellar buckling instability to change direction. *Nature Physics*, 9(8):494–498, 2013.

[116] Yoshiyuki Sowa, Hiroyuki Hotta, Michio Homma, and Akihiko Ishijima. Torque–speed relationship of the Na^{+-}driven flagellar motor of vibrio alginolyticus. *Journal of Molecular Biology*, 327(5):1043–1051, 2003.

[117] Geoffrey Ingram Taylor. Analysis of the swimming of microscopic organisms. *Proceedings of the Royal Society of London. Series A. Mathematical and Physical Sciences*, 209(1099):447–461, 1951.

[118] Geoffrey Ingram Taylor. The action of waving cylindrical tails in propelling microscopic organisms. *Proceedings of the Royal Society of London. Series A. Mathematical and Physical Sciences*, 211(1105):225–239, 1952.

[119] Viola Tokárová, Ayyappasamy Sudalaiyadum Perumal, Monalisha Nayak, Henry Shum, Ondřej Kašpar, Kavya Rajendran, Mahmood Mohammadi, Charles Tremblay, Eamonn A Gaffney, Sylvain Martel, et al. Patterns of bacterial motility in microfluidics-confining environments. *Proceedings of the National Academy of Sciences*, 118(17), 2021.

[120] Linda Turner, Liam Ping, Marianna Neubauer, and Howard C Berg. Visualizing flagella while tracking bacteria. *Biophysical Journal*, 111(3):630–639, 2016.

[121] Linda Turner, William S Ryu, and Howard C Berg. Real-time imaging of fluorescent flagellar filaments. *Journal of Bacteriology*, 182(10):2793–2801, 2000.

[122] Linda Turner, Rongjing Zhang, Nicholas C Darnton, and Howard C Berg. Visualization of flagella during bacterial swarming. *Journal of Bacteriology*, 192(13):3259–3267, 2010.

[123] Margot A-S Vigeant, Roseanne M Ford, Michael Wagner, and Lukas K Tamm. Reversible and irreversible adhesion of motile Escherichia coli cells analyzed by total internal reflection aqueous fluorescence microscopy. *Applied and Environmental Microbiology*, 68(6):2794–2801, 2002.

[124] Nobuhiko Watari and Ronald G Larson. The hydrodynamics of a run-and-tumble bacterium propelled by polymorphic helical flagella. *Biophysical Journal*, 98(1):12–17, 2010.

[125] David White et al. *Physiology and biochemistry of prokaryotes*. Oxford University Press, 2000.

[126] Kuan-Ting Wu, Yi-Teng Hsiao, and Wei-Yen Woon. Entrapment of pusher and puller bacteria near a solid surface. *Physical Review E*, 98(5):052407, 2018.

[127] Li Xie, Tuba Altindal, Suddhashil Chattopadhyay, and Xiao-Lun Wu. Bacterial flagellum as a propeller and as a rudder for efficient chemotaxis. *Proceedings of the National Academy of Sciences*, 108(6):2246–2251, 2011.

[128] Xianghua Xu and Ali Nadim. Deformation and orientation of an elastic slender body sedimenting in a viscous liquid. *Physics of Fluids*, 6(9):2889–2893, 1994.

[129] Tomoko Yamaguchi, Fumiaki Makino, Tomoko Miyata, Tohru Minamino, Takayuki Kato, and Keiichi Namba. Structure of the molecular bushing of the bacterial flagellar motor. *Nature Communications*, 12(1):1–12, 2021.

[130] Cenyu Yang, Chuanfang Chen, Qiufeng Ma, Longfei Wu, and Tao Song. Dynamic model and motion mechanism of magnetotactic bacteria with two lateral flagellar bundles. *Journal of Bionic Engineering*, 9(2):200–210, 2012.

[131] Junhua Yuan, Karen A Fahrner, Linda Turner, and Howard C Berg. Asymmetry in the clockwise and counterclockwise rotation of the bacterial flagellar motor. *Proceedings of the National Academy of Sciences*, 107(29):12846–12849, 2010.

APPENDICES

Appendix A

Model bacterium with rigid flagella

A.1 Governing equations

In some sections of the thesis, the swimming behavior of the model bacteria with the flexible flagellum is compared with the rigid model. In this section, we briefly simplify our framework for the model bacteria in which the flagella are rigid.

Like the flexible model, we discretize the flagella into a finite number of straight segments. However, the segments are assumed to be fixed with respect to each other in the rigid model. Therefore, the Kirchhoff rod model which is employed to estimate the internal moments between the flagella joints is removed from the system of equations. Moreover, the complexity of the kinematic equations reduces because the angular and translational velocity of each point on the model bacterium surface can be represented in terms of three unknowns $\vec{U}^{(B)}$, $\vec{\Omega}^{(B)}$ and $\vec{\omega}_r^{(i)}$. As a result, Eq. 2.58 is rewritten as:

$$\vec{U}(\vec{X}^E) = \begin{cases} \vec{U}^{(B)} + \vec{\Omega}^{(B)} \times \left(\vec{X}^E - \vec{X}^{(B)}\right), & \vec{X}^E \text{ on cell body,} \\ \vec{U}^{(B)} + \vec{\Omega}^{(B)} \times \left(\vec{X}^E - \vec{X}^{(B)}\right) + \vec{\omega}_r^{(i)} \times \vec{X}_{\text{rel}}^{(i)}, & \vec{X}^E \text{ on } i\text{th flagellum,} \end{cases} \tag{A.1}$$

where

$$\vec{X}_{\text{rel}}^{(i)} = \vec{X}^E - \vec{X}^{(i)} \quad , \tag{A.2}$$

and $\vec{\omega}_r^{(i)}$ is the rotational velocity of the ith flagellar rotor.

Similarly, Eq. 2.60 is revised as:

$$\vec{\omega}(\vec{X}^E) = \vec{\Omega}^{(B)} + \vec{\omega}_r^{(i)}, \qquad \vec{X}^E \text{ on } i\text{th flagellum.} \tag{A.3}$$

Accordingly, Eq. 2.61 changes to:

$$\begin{bmatrix} \vec{u}_1 \\ \vdots \\ \vec{u}_{N_{\mathrm{PB}}+N_{\mathrm{F}}\cdot N_{\mathrm{PF}}} \end{bmatrix} = A'_3 \begin{bmatrix} \vec{U}^{(B)} \\ \vec{\Omega}^{(B)} \\ \vec{\omega}_r^{(1)} \\ \vdots \\ \vec{\omega}_r^{(N_{\mathrm{F}})} \end{bmatrix}, \quad \begin{bmatrix} \vec{\omega}_1 \\ \vdots \\ \vec{\omega}_{N_{\mathrm{F}}\cdot N_{\mathrm{PF}}} \end{bmatrix} = A'_4 \begin{bmatrix} \vec{\Omega}^{(B)} \\ \vec{\omega}_r^{(1)} \\ \vdots \\ \vec{\omega}_r^{(N_{\mathrm{F}})} \end{bmatrix}, \tag{A.4}$$

where the matrices A'_3 and A'_4 are determined by using the position vectors, according to Eqs. A.1 and A.3.

Like the flexible model, the total torques and forces acting on the bacterium complex are zero. However, the torque balance equations about the flagella joints (i.e. Eq. 2.69) are removed from the system of linear equations, and instead, torque balance equations to satisfy the motor torque constraints are added to the equations. This equation for ith flagellum is expressed as:

$$\vec{e}_1^{(i)} \cdot \left(\int_{\Gamma^{(i)}} \vec{\gamma} \times \vec{f}_{\mathrm{F}} ds + \int_{\Gamma^{(i)}} \vec{n} ds \right) + T_i = 0. \tag{A.5}$$

The first and second integrals represent the torque induced by the hydrodynamic forces and torques along the ith flagellum, respectively. The projection of this torque on the rotor axis is balanced by the motor torque. Since the rotational velocity vector of each rotor is expressed as $W^{(i)\mathrm{rot}}\vec{e}_1^{(i)}$, Eq. A.5 is solved in coupled with the other equations in the system of the linear equations for the scalar unknown $W^{(i)\mathrm{rot}}$ which denotes the ith motor's rotation rate. By applying these simplifications, the simplified form of the system of the linear equations is solved for three unknowns $W^{(i)\mathrm{rot}}$, $\vec{U}^{(B)}$ and $\vec{\Omega}^{(B)}$. In the next step, the configuration of the model bacterium is updated according to these translational and angular velocities.

Appendix B

Convergence of numerical methods

In addition to the verifications presented in section 2.8, we conduct the following simulations to test the convergence of the swimming properties to the rigid model (Fig. B.1), the convergence of the swimming properties with the mesh refinement (Figs. B.2-B.4), stability of the numerical solutions (Fig. B.5), impacts of the twisting stiffness to the bending stiffness ratio Υ and the regularization parameter on the progressive speed (Figs. B.6-B.7), and the sensitivity of the maximum time step to some most important parameters (Fig. B.8).

Table B.1: Mesh refinement level for convergence test

Refinement Level	N_S	N_B
1	12	24
2	18	60
3	24	112
4	30	180
5	36	264
6	42	364

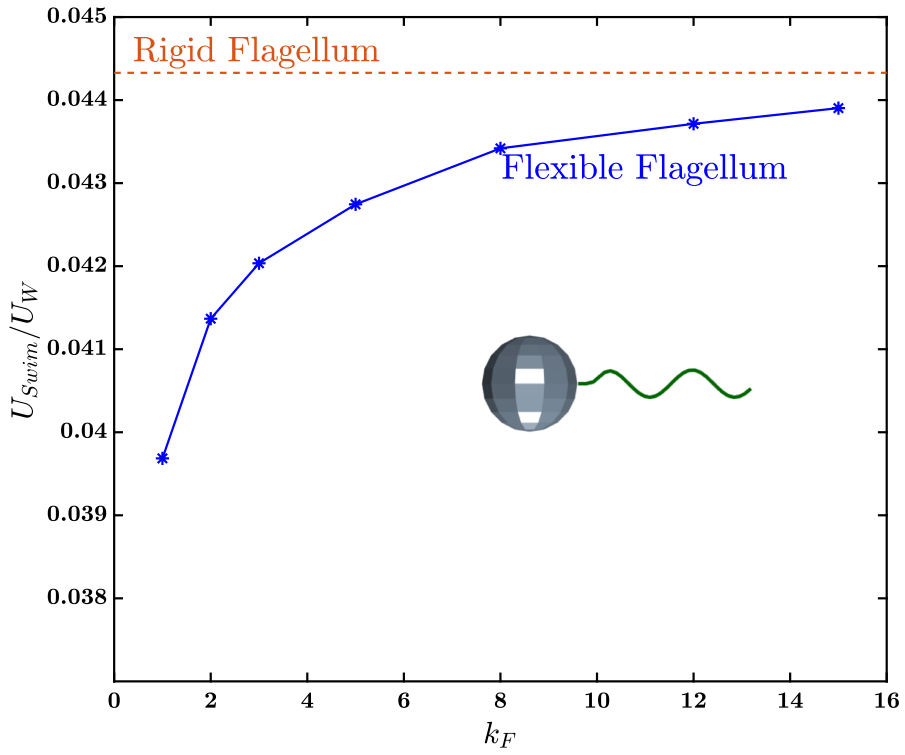

Figure B.1: Progressive speed of a uniflagellated model bacterium with flexible and rigid flagellum at constant motor speed. U_{swim}/U_w is the progressive speed non-dimensionalized by the linear wavespeed of the flagellum. As expected, the progressive speed of the model bacterium converges to the rigid model as the stiffness of the flagellum increases. In this model bacterium, the physical parameters are defined as $\frac{l}{R} = 5$, $\frac{\epsilon}{R} = 0.02$, $\frac{p}{a} = 2\pi$, $ak_{\mathrm{E}} = 1$,$N_{\mathrm{S}} = 30$ and $N_{\mathrm{B}} = 180$. There is no hook in this model bacterium, but it is assumed that the first segment of the flagellum is straight and the helical shape of the flagellum starts after the first segment. In order to align the flagellum axis with the cell body axis, amplitude envelope growth rate k_E is used to describe the flagellum shape. In fact, the bacterium configuration in this simulation is according to Higdon's model [46] with minor differences in connecting the flagellum to the cell body.

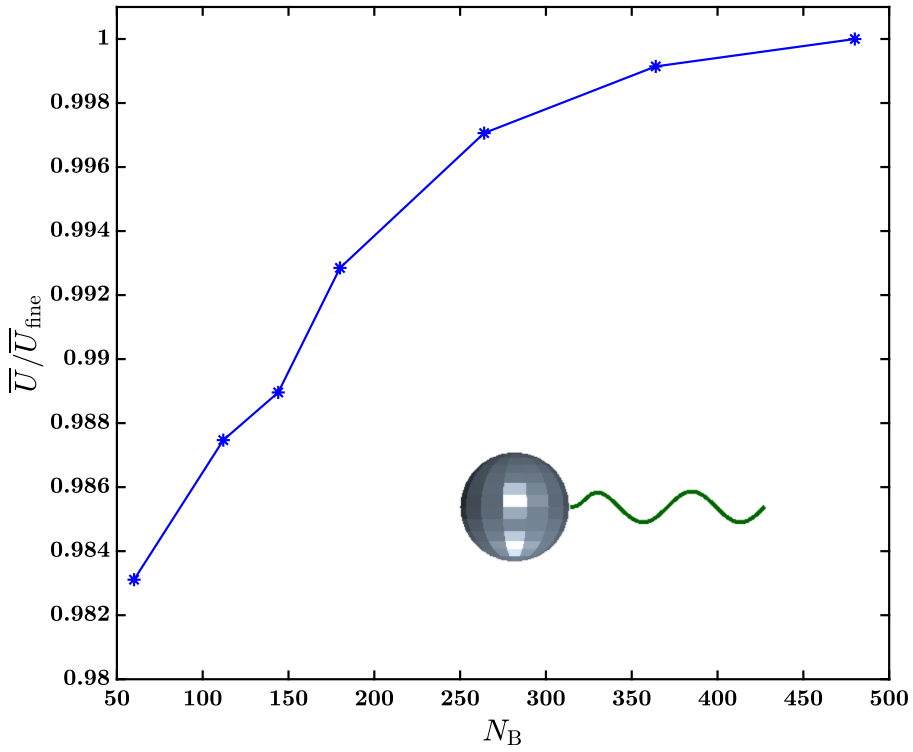

Figure B.2: Convergence of the numerical method with respect to the cell body mesh refinement for a bacterium with flexible flagellum swimming in free space and constant motor speed. The steady-state progressive speed, $\overline{U}$, increasingly converges to its most accurate value. The speeds in this graph are scaled by the value obtained at the finest mesh ($N_{\text{s}} = 480$), $\overline{U}_{\text{fine}}$. In this model bacterium, the physical parameters are defined as $\frac{l}{R} = 5$, $\frac{\epsilon}{R} = 0.02$, $\frac{p}{a} = 2\pi$, $ak_{\text{E}} = 1$, $N_{\text{S}} = 30$ and $k_{\text{F}} = 3$. In order to align the flagellum axis with the cell body axis, amplitude envelope growth rate k_{E} is used to describe the flagellum shape.

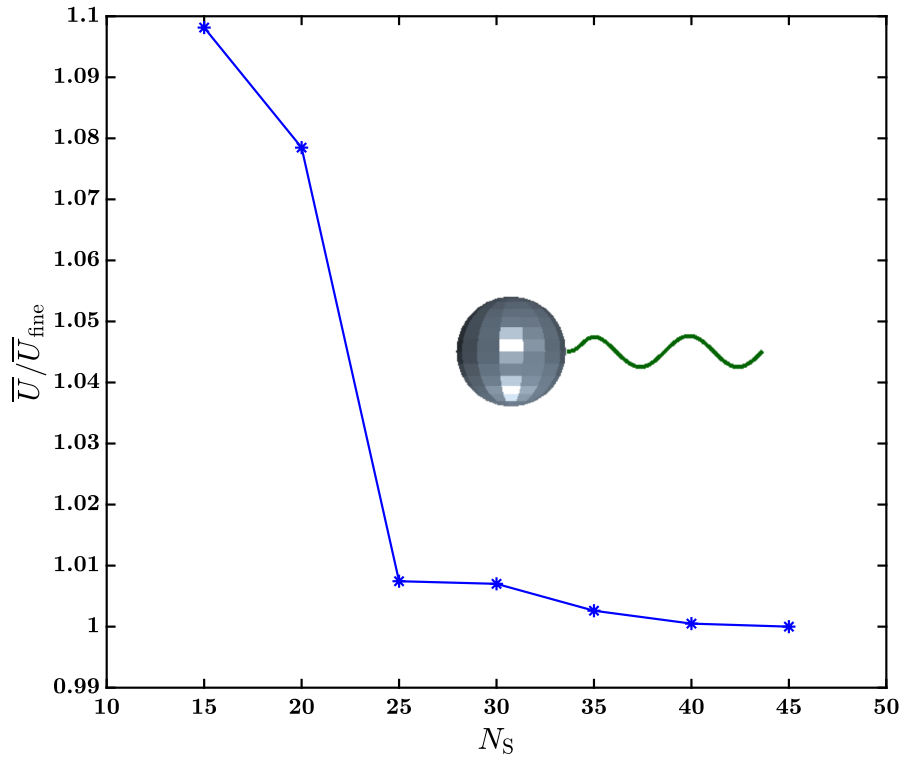

Figure B.3: Convergence of the numerical method with respect to the flagellum mesh refinement for a bacterium with flexible flagellum swimming in free space and constant motor speed. The steady-state progressive speeds, $\overline{U}$, which are scaled by the value obtained at the finest grid, are reported in the different numbers of the segments on the flagellum. Unlike Fig. B.2, the progressive speed decreasingly converges to its most accurate value. In this model bacterium, the physical parameters are defined as $\frac{l}{R} = 5$, $\frac{\epsilon}{R} = 0.02$, $\frac{p}{a} = 2\pi$, $ak_{\text{E}} = 1$, $N_{\text{B}} = 180$ and $k_{\text{F}} = 3$. In order to align the flagellum axis with the cell body axis, amplitude envelope growth rate k_{E} is used to describe the flagellum shape.

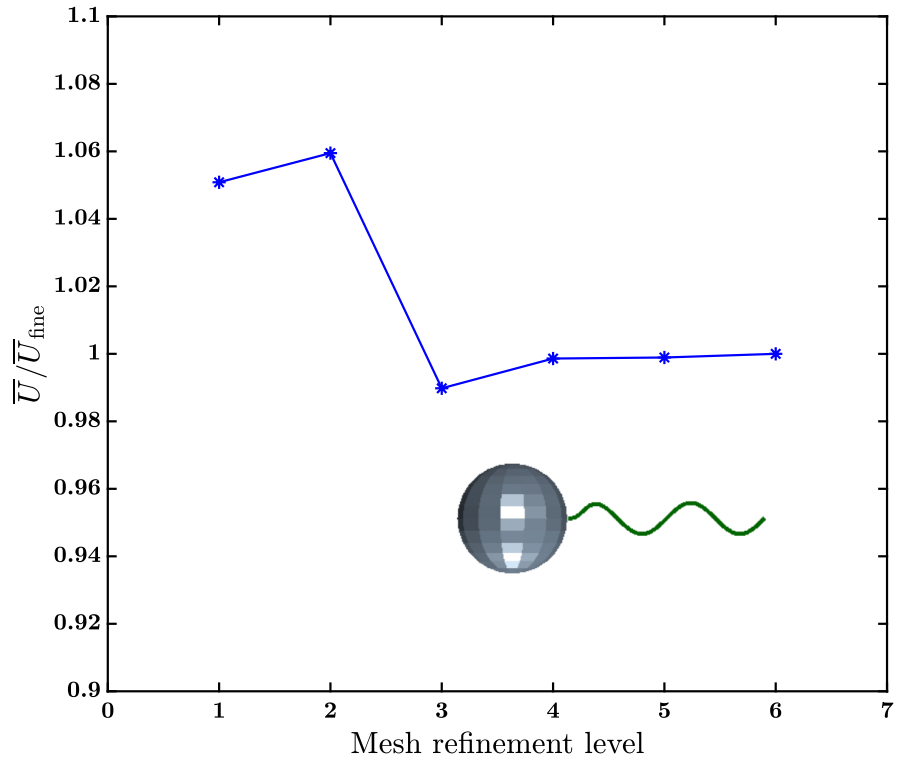

Figure B.4: Convergence of the numerical method with respect to the cell body and flagellum meshes refinement. The steady-state progressive speeds, $\overline{U}$, which are scaled by the value at the highest refinement level 6, are presented in the different levels of the flagellum and cell body meshes refinement. The number of segments and the element at each level of refinement are described in Tab. B.1. For the refinement level 3 and more the error is less than 1.5%. The model bacterium has a flexible flagellum and swims in free space with a constant motor speed. The physical parameters are defined as $\frac{l}{R} = 5$, $\frac{\epsilon}{R} = 0.02$, $\frac{p}{a} = 2\pi$, $ak_{\text{E}} = 1$ and $k_{\text{F}} = 3$. In order to align the flagellum axis with the cell body axis, amplitude envelope growth rate k_{E} is used to describe the flagellum shape.

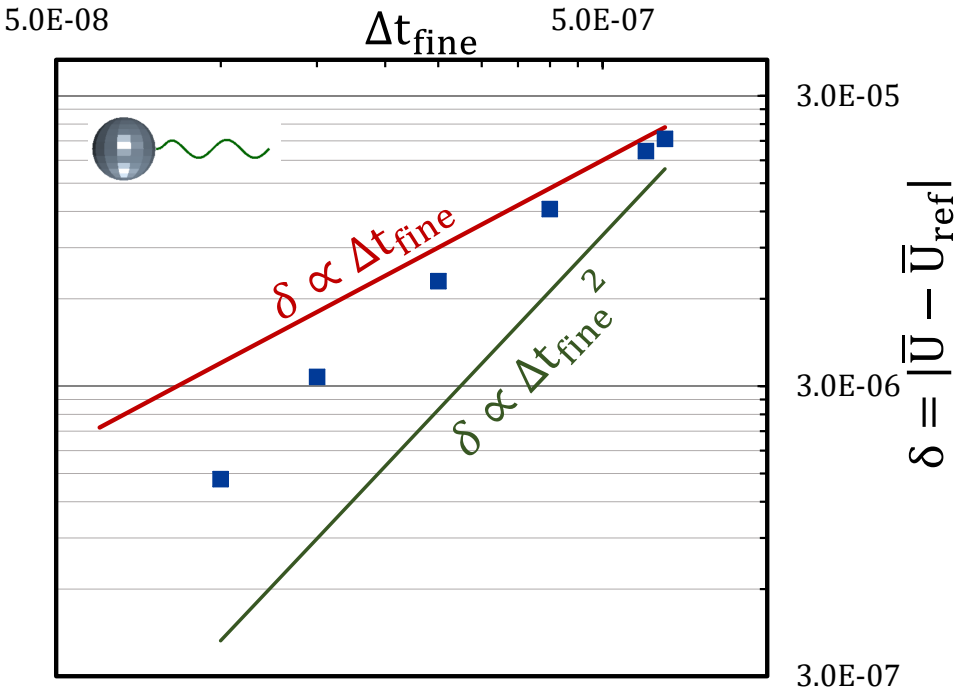

Figure B.5: Test for the time step independency of the numerical scheme developed in this thesis. The progressive speeds of the model bacterium are calculated explicitly using the forward Euler method with different time steps. The convergence of the absolute error is shown in the log-log scale. The absolute error is defined as $\delta = |\overline{U} - \overline{U}_{\mathrm{ref}}|$; where $\overline{U}_{\mathrm{ref}}$ is the progressive speed obtained at the finest time step $\Delta t_{\mathrm{fine}} = 6 \times 10^{-8}$. In the studied model bacterium, the physical parameters are defined as $\frac{l}{R} = 5$, $\frac{\epsilon}{R} = 0.02$, $\frac{p}{a} = 2\pi$, $ak_{\mathrm{E}} = 1$, $N_{\mathrm{B}} = 180$, $N_{\mathrm{S}} = 30$, $\frac{\Delta t_{\mathrm{coarse}}}{\Delta t_{\mathrm{fine}}} = 100$ and $k_{\mathrm{F}} = 3$. In order to align the flagellum axis with the cell body axis, amplitude envelope growth rate k_{E} is used to describe the flagellum shape.

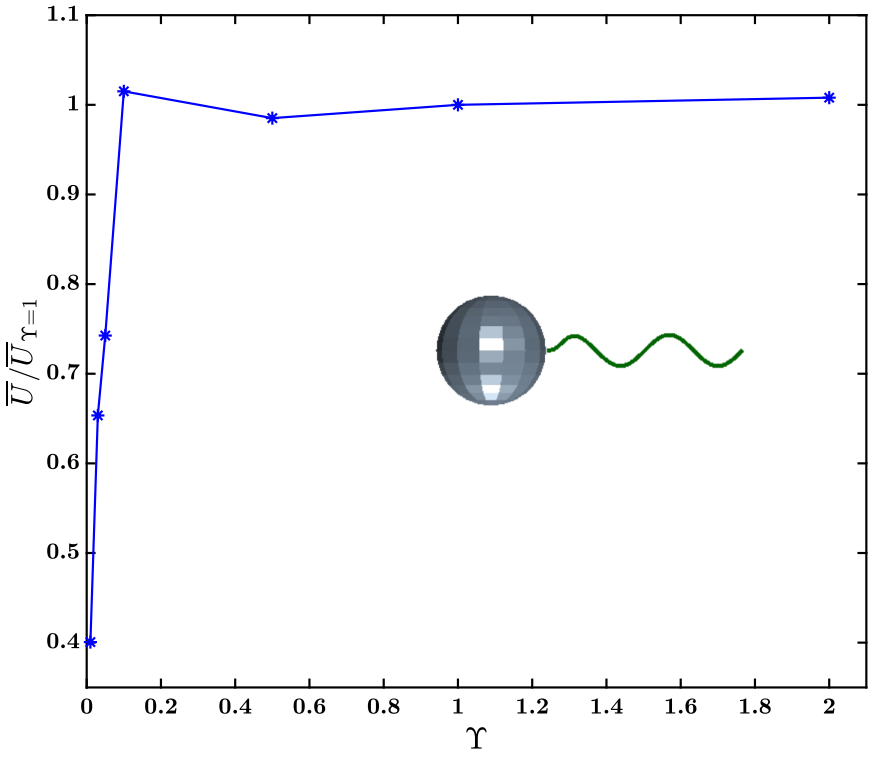

Figure B.6: Impact of the ratio of the twisting stiffness GJ to the bending stiffness EI of the flagellum on the progressive speed of the model bacterium. The steady-state progressive speeds of the model bacterium in free space and constant motor speed are calculated using different ratios Υ for the flagellum. These speeds are scaled by the value obtained at the case with $\Upsilon = 1$ (as a reference ratio used in this thesis). In smaller ratios ($\Upsilon < 0.2$), the twisting of the flagellum changes the effective amplitude and the number of turns along the flagellum, and therefore, the progressive speed decreases. In higher ratios, the swimming properties remain fairly constant. In this model bacterium, the physical parameters are defined as $\frac{l}{R} = 5$, $\frac{\epsilon}{R} = 0.02$, $\frac{p}{a} = 2\pi$, $ak_{\mathrm{E}} = 1$, $N_{\mathrm{B}} = 180$, $N_{\mathrm{S}} = 30$ and $k_{\mathrm{F}} = 3$. In order to align the flagellum axis with the cell body axis, amplitude envelope growth rate k_{E} is used to describe the flagellum shape.

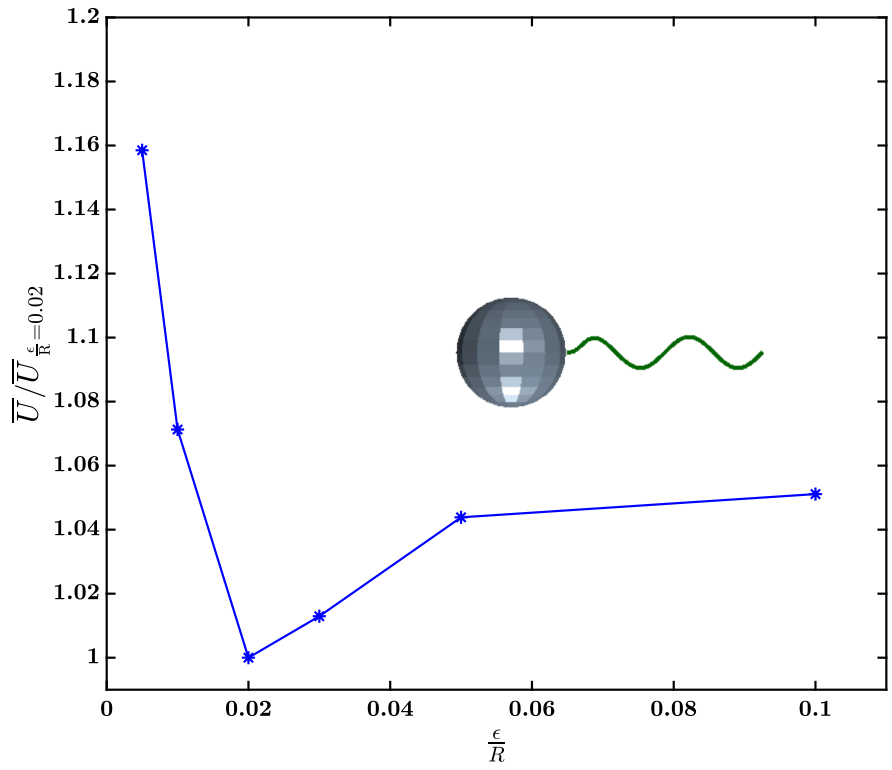

Figure B.7: Impact of the regularization parameter $\frac{\epsilon}{R}$ on the progressive speed of the model bacterium. The steady-state progressive speeds of the model bacterium in free space and constant motor speed are calculated using different regularization parameters $\frac{\epsilon}{R}$ for the flagellum. These speeds are scaled by the value obtained at the case with $\frac{\epsilon}{R} = 0.02$ (as a reference regularization parameter used in the verifications). In smaller regularization parameters ($\frac{\epsilon}{R} < 0.05$), the progressive speed's dependency on the regularization parameter is considerable. In this model bacterium, the physical parameters are defined as $\frac{l}{R} = 5$, $\frac{p}{a} = 2\pi$, $ak_{\mathrm{E}} = 1$, $N_{\mathrm{B}} = 180$, $N_{\mathrm{S}} = 30$ and $k_{\mathrm{F}} = 3$. In order to align the flagellum axis with the cell body axis, amplitude envelope growth rate k_{E} is used to describe the flagellum shape.

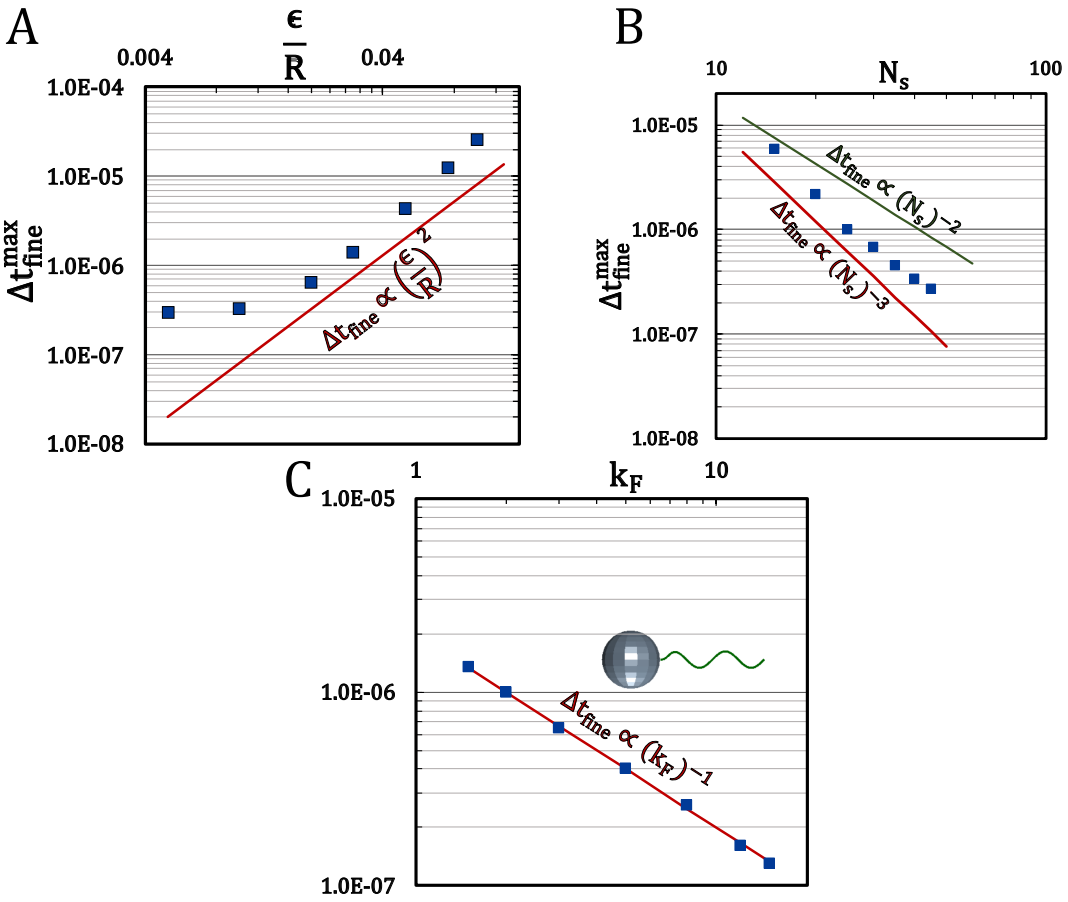

Figure B.8: Impacts of the regularization parameter (A), the number of the flagellum's segments (B), and the flagellum's stiffness (C) on the largest time step $\Delta\, t_{\text{fine}}^{\max}$ for ensuring the solution stability. The graphs are plotted in the log-log scale and the data points are obtained manually by increasing the time step with increments of 10^{-8} until the largest value in which the solution is numerically stable. We decide on the stability of the solution by checking the obtained results in the first 100 steps. The obtained results indicate that the time step required to solve the stiff ODEs (discussed in section 2.7) significantly depends on the regularization parameter ($\frac{\epsilon}{R}$) and the number of segments on the flagellum (N_{s}). The time step is less sensitive to the flagellum stiffness (k_{F}), comparatively. In the uniflagellated model bacterium with a flexible flagellum, the physical parameters are defined as $\frac{l}{R} = 5$, $\frac{p}{a} = 2\pi$, $ak_{\text{E}} = 1$, $N_{\text{B}} = 180$, $N_{\text{S}} = 30$ and $k_{\text{F}} = 3$. Obviously, the parameter that varies at each graph is not fixed at the given value. In order to align the flagellum axis with the cell body axis, amplitude envelope growth rate k_{E} is used to describe the flagellum shape.